

**TiO<sub>2</sub> – ZnO NANO COMPOSITE FILMS IN SOLAR  
DRIVEN WATER SPLITTING PERFORMANCE**

**NUR AZIMAH BINTI ABD SAMAD**

**INSTITUTE OF GRADUATE STUDIES  
UNIVERSITY OF MALAYA  
KUALA LUMPUR**

**2016**

**TiO<sub>2</sub> – ZnO NANO COMPOSITE FILMS IN SOLAR  
DRIVEN WATER SPLITTING PERFORMANCE**

**NUR AZIMAH BINTI ABD SAMAD**

**DISSERTATION SUBMITTED IN FULFILMENT OF  
THE REQUIREMENTS FOR THE DEGREE OF MASTER  
OF PHILOSOPHY**

**INSTITUTE OF GRADUATE STUDIES  
UNIVERSITY OF MALAYA  
KUALA LUMPUR**

**2016**

**UNIVERSITY OF MALAYA**  
**ORIGINAL LITERARY WORK DECLARATION**

Name of Candidate: NUR AZIMAH BINTI ABD SAMAD

Matric No: HGA140002

Name of Degree: MASTER OF PHILOSOPHY

Title of Thesis ("this Work"): TiO<sub>2</sub> – ZnO NANO COMPOSITE FILMS IN  
SOLAR DRIVEN WATER SPLITTING PERFORMANCE

Field of Study: MATERIALS ENGINEERING (NANOTECHNOLOGY)

I do solemnly and sincerely declare that:

- (1) I am the sole author/writer of this Work;
- (2) This Work is original;
- (3) Any use of any work in which copyright exists was done by way of fair dealing and for permitted purposes and any excerpt or extract from, or reference to or reproduction of any copyright work has been disclosed expressly and sufficiently and the title of the Work and its authorship have been acknowledged in this Work;
- (4) I do not have any actual knowledge nor do I ought reasonably to know that the making of this work constitutes an infringement of any copyright work;
- (5) I hereby assign all and every rights in the copyright to this Work to the University of Malaya ("UM"), who henceforth shall be owner of the copyright in this Work and that any reproduction or use in any form or by any means whatsoever is prohibited without the written consent of UM having been first had and obtained;
- (6) I am fully aware that if in the course of making this Work I have infringed any copyright whether intentionally or otherwise, I may be subject to legal action or any other action as may be determined by UM.

Candidate's Signature

Date:

Subscribed and solemnly declared before,

Witness's Signature

Date:

Name:

Designation:

## ABSTRACT

Solar driven water splitting system is a key target for the development of sustainable hydrogen economy for future energy system. The formation of self-organized zinc oxide (ZnO) nanostructures is essential for high efficiency in photoelectrochemical (PEC) solar driven water splitting system. Comprehensive investigations on different parameters, such as heat treatment, stirring process, reaction temperature, exposure time, and applied potential were conducted in order to control the specific architecture of ZnO nanostructures. Based on the results obtained, ZnO nanorod; diameter in a range of 35.0 – 65.0 nm and length in a range of 210.0 – 280.0 nm were successfully formed via electrodeposition technique in an electrolyte containing 0.05 mM ZnCl<sub>2</sub> and 0.1 M KCl at 1.0 V for 60 min. Continuous efforts have been exerted to further improve the PEC water splitting performance by incorporating an optimum content of TiO<sub>2</sub> nanoparticles on ZnO nanorod film via dip-coating technique. The modification of ZnO nanorod was to overcome several drawbacks, including poor visible light absorption and high recombination losses of charge carrier. It was found that 0.25 at% of TiO<sub>2</sub> nanoparticles coated on ZnO nanorod film and subsequently heat treated at 400 °C demonstrated a maximum photocurrent density of 19.78 mA/cm<sup>2</sup> (1.66 % photoconversion efficiency) under UV ray (300 nm) and 14.75 mA/cm<sup>2</sup> (2.18 % photoconversion efficiency) under visible light (500 nm). This performance was approximately 2-3 times higher than the ZnO nanorod film. The presence of Ti element in hybrid TiO<sub>2</sub>-ZnO film (below 1 at% Ti) showed an improvement of photocurrent density and photoconversion efficiency because it acted as an effective mediator to trap the photo-induced electrons and minimize the recombination of charge carriers. It is a well-known fact that phenomenon of charge carriers-separation effect at type-II band alignment of Zn and Ti might further enhanced the transportation for photo-induced charge carriers during illumination. Contra in results appeared with the redundant of TiO<sub>2</sub> nanoparticles coated on ZnO nanorod wall surface.

PEC water splitting performance became poor because TiO<sub>2</sub> nanoparticles formed independent layers and electrons in TiO<sub>2</sub> were trapped by the excess amount of oxygen and could not be transferred to ZnO.

University of Malaya

## ABSTRAK

Penjanaan hidrogen solar daripada sistem pembelahan air pacuan suria (elektrolisis air) merupakan sasaran utama bagi membangunkan ekonomi hidrogen yang mampan untuk sistem tenaga masa hadapan. Pembentukan sendiri ZnO nanostruktur (ZnO nanorod) adalah penting bagi memastikan kecekapan yang tinggi dalam aplikasi sistem pembelahan air (elektrolisis air) pacuan suria fotoelektrokimia (PEC). Penyiasatan menyeluruh pada parameter yang berbeza, iaitu rawatan haba, proses pengacauan, suhu tindak balas, tempoh dedahan, dan keupayaan yang dikenakan telah dijalankan bagi mengawal pembentukan ZnO nanostruktur. Dalam kajian ini, ZnO nanorod terarah telah berjaya disintesis dalam julat diameter 35.0 – 65.0 nm dan julat panjang 210.0 – 280.0 nm melalui pengendapan elektrokimia dengan elektrolit 0.05 mM ZnCl<sub>2</sub> dan ejen pengarah 0.1 M KCl pada 1.0 V selama 60 minit. Penting untuk menyedari bahawa zink oksida (ZnO) mempunyai beberapa kelemahan seperti rendah penyerapan cahaya tampak (hanya berkesan berfungsi di bawah sinar UV) dan penggabungan semula dan kehilangan caj pembawa. Usaha yang berterusan telah dilaksanakan bagi meningkatkan prestasi fotoelektrokimia pemisahan air dengan menggabungkan suatu kandungan optimum TiO<sub>2</sub> ke atas ZnO nanorod menggunakan teknik rendam-salut. Pengubahsuain ZnO nanorod adalah bagi mengatasi beberapa kelemahannya seperti penyerapan cahaya tampak yang lemah dan penggabungan semula pembawa cas yang tinggi. Didapati bahawa 0.25 at% TiO<sub>2</sub> menunjukkan kepadatan arusfoto maksimum 19.78 mA / cm<sup>2</sup> di bawah sinar UV (300 nm) dan 14.75 mA / cm<sup>2</sup> di bawah cahaya tampak (500 nm) iaitu masing-masing dengan kecekapan tukarfoto ~ 1.66 % and ~2.18 % . Prestasi ini adalah 2-3 kali ganda lebih tinggi daripada filem ZnO nanorod tulen. Satu peningkatan ketumpatan arusfoto dan kecekapan tukarfoto berlaku dengan kehadiran unsur Ti dalam hibrid TiO<sub>2</sub>-ZnO filem (di bawah 1 at% Ti) iaitu Ti bertindak sebagai pengantara yang berkesan dalam memerangkap elektron aruhan foto serta meminimumkan penggabungan semula

pembawa cas. Kesan fenomena pemisahan cas pembawa pada penjajaran jalur jenis-II Zn dan Ti berpotensi menggalakkan pengangkutan pembawa cas aruhan foto semasa pencahayaan. Keputusan yang berbeza diperolehi apabila TiO<sub>2</sub> berlebihan disalut pada permukaan dinding ZnO nanorod. Prestasi fotoelektrokimia pemisahan air menurun apabila TiO<sub>2</sub> nanopartikel membentuk lapisan bebas manakala elektron dalam TiO terperangkap dalam lebihan amaun oksigen serta tidak boleh dipindahkan ke ZnO.

University of Malaya

## ACKNOWLEDGEMENTS

It is a genuine pleasure to express my deep sense of thanks and gratitude to my supervisors; Dr Lai Chin Wei and Prof Dr Sharifah Bee Abd Hamid on their dedication and keen interest above all their overwhelming attitude to help me completing my work. Their timely advice, meticulous scrutiny, scholarly advice and scientific approach have helped me to a very great extent to accomplish this research.

This research was supported by grants from the Fundamental Research Grant Scheme (FRGS), University Malaya Research Grant (UMRG) and Postgraduate Research Fund (PPP) for the sources of funding through this study. I gratefully acknowledge University of Malaya for financial supporting that helping me in this study and MyMaster scholarship from Kementerian Pendidikan Malaysia (KPM).

I owe a deep sense of gratitude to all NANOCAT's technical and administrative staff and University of Malaya for their keen interest on helping me at every stage of my research work and accommodation. I extremely thankful to my NANOCAT's best friends for their kind help and co-operation throughout my study period.

It is my privilege to thank my family especially my husband; Mohd Azahari Isa, my mother; Zaleha Mohd Yusof, my father; Abd Samad Mahmud, and my children; 'Aisyah Ummul Mukminin, Sofiyah Ummul Mukminin, and my beloved late Umair for your financial support, moral support, understanding, and constant encouragement which were the sustaining factors in carrying out my research work successfully.

## TABLE OF CONTENTS

Abstract .....	iii
Abstrak .....	v
Acknowledgements .....	vii
Table of Contents .....	viii
List of Figures .....	xiii
List of Tables.....	xvi
List of Symbols and Abbreviations.....	xviii
<b>CHAPTER 1: INTRODUCTION.....</b>	<b>1</b>
1.1 Introduction.....	1
1.2 Problem statement .....	6
1.3 Objectives of Research .....	7
1.4 Outline of Research Work .....	7
1.5 Thesis overview .....	7
<b>CHAPTER 2: LITERATURE REVIEW.....</b>	<b>9</b>
2.1 Importance of hydrogen.....	9
2.2 Principal of PEC water splitting system .....	12
2.3 The engineering behind ZnO nanostructures.....	15
2.3.1 Synthesis of ZnO nanostructures.....	18
2.3.1.1 Synthesis of ZnO nanostructures from sol-gel technique .....	18
2.3.1.2 Synthesis of ZnO nanostructures from hydrothermal technique.....	18
2.3.1.3 Synthesis of ZnO nanostructures from solvothermal technique	19

2.3.1.4	Synthesis of ZnO nanostructures from electrodeposition technique .....	20
2.3.1.5	Synthesis of ZnO nanostructures from chemical vapor deposition (CVD).....	21
2.3.1.6	Synthesis of ZnO nanostructures from atomic layer deposition (ALD) .....	22
2.4	Crystallization of ZnO nanostructures.....	26
2.5	Modification of ZnO nanostructures .....	28
2.5.1	Metal-coated ZnO nanostructures .....	28
2.5.2	Polyaniline-modified ZnO nanostructures .....	29
2.5.3	Carbon-modified ZnO nanostructures .....	29
2.5.4	Semiconductor-modified ZnO nanostructures .....	30
2.6	Hybrid TiO <sub>2</sub> -ZnO nanostructure film as photoelectrode.....	31
<b>CHAPTER 3: METHODOLOGY.....</b>		<b>37</b>
3.1	Raw materials .....	38
3.2	Synthesis of ZnO nanostructures film .....	40
3.2.1	Foil preparation .....	40
3.2.2	Electrolyte preparation .....	41
3.2.3	Electrodeposition procedure.....	41
3.2.4	Cleaning ZnO nanostructures .....	42
3.3	Synthesis of TiO <sub>2</sub> nanoparticles .....	42
3.3.1	Acidified water preparation.....	42
3.3.2	Dilution of Titanium (IV) isopropoxide (TTIP).....	43
3.3.3	Precipitation and peptization procedure .....	43
3.3.4	Washing TiO <sub>2</sub> nanoparticles precursor.....	44

3.4	Synthesis of hybrid TiO <sub>2</sub> -ZnO film .....	44
3.4.1	Annealing process .....	44
3.5	Characterization Techniques .....	45
3.5.1	Field emission scanning electron microscopy (FESEM) .....	45
3.5.2	High resolution transmission electron microscopy (HRTEM).....	46
3.5.3	X-ray diffraction (XRD).....	47
3.5.4	Raman spectroscopy .....	48
3.5.5	Photoluminescence spectroscopy (PL).....	48
3.5.6	UV-Vis diffuse reflectance spectroscopy (UV-DR).....	49
3.5.7	X-ray photoelectron spectroscopy (XPS).....	50
3.6	Photoelectrochemical (PEC) water splitting performance .....	50
3.6.1	Photocurrent density analysis .....	51
3.6.2	Photoconversion efficiency analysis .....	51
3.6.3	Mott – Schottky Analysis .....	52
<b>CHAPTER 4: RESULTS AND DISCUSSION .....</b>		<b>53</b>
4.1	Easy formation of highly responsive ZnO nanostructures .....	53
4.1.1	The effect of heat treatment to crystallization aspect.....	54
4.1.1.1	Morphological studies and elemental analysis by FESEM-EDX and HRTEM .....	55
4.1.1.2	Phase structure analysis by XRD .....	58
4.1.1.3	Photoelectrochemical response .....	61
4.1.2	The influence of stirring process towards the formation of ZnO nanostructure film.....	64
4.1.2.1	Morphological studies and elemental analysis by FESEM- EDX.....	65

4.1.2.2	Phase structure analysis by XRD .....	67
4.1.2.3	Photoelectrochemical water splitting evaluation.....	68
4.1.3	The influence of reaction temperature towards the formation of ZnO nanostructure film.....	71
4.1.3.1	Morphological studies and elemental analysis by FESEM-EDX.....	71
4.1.4	The influence of exposure time towards the formation of ZnO nanostructure film.....	75
4.1.4.1	Morphological studies and elemental analysis by FESEM.....	75
4.1.5	The influence of applied potential towards the formation of ZnO nanostructure film.....	79
4.1.5.1	Morphological studies and elemental analysis by FESEM-EDX and HRTEM .....	80
4.1.5.2	Phase structure analysis by XRD and Raman Scattering .....	83
4.1.5.3	Charge carriers recombination by PL.....	86
4.1.5.4	Photoelectrochemical water splitting evaluation.....	87
4.2	Formation of TiO <sub>2</sub> nanoparticles via precipitation-peptization technique .....	90
4.2.1	The influence of temperature towards the formation of TiO <sub>2</sub> nanoparticles.....	90
4.2.1.1	Morphological studies and elemental analysis by FESEM-EDX.....	90
4.2.1.2	Phase structure analysis by XRD .....	91
4.2.2	The influence of stirring towards the formation of TiO <sub>2</sub> nanoparticles ...	93
4.2.2.1	Morphological studies and elemental analysis by FESEM-EDX.....	93
4.2.2.2	Phase structure analysis by XRD .....	95

4.3	Hybrid TiO <sub>2</sub> -ZnO nanostructure film .....	97
4.3.1	The influence of exposure time during dip-coating technique .....	98
4.3.1.1	Morphological studies and elemental analysis by FESEM .....	98
4.3.1.2	Phase structure analysis by XRD .....	99
4.3.2	The influence on the number of dipping cycles .....	101
4.3.2.1	Morphological studies and elemental analysis by FESEM-EDX and HRTEM .....	101
4.3.2.2	Phase structure analysis by XRD and Raman Scattering .....	103
4.3.2.3	Chemical state analysis .....	106
4.3.2.4	Photoluminescence behavior by PL .....	111
4.3.2.5	Photoelectrochemical response and photoconversion efficiency .....	112
4.3.2.6	UV-vis diffusive reflectance analysis .....	116
4.3.2.7	Mott-Schottky analysis .....	118
<b>CHAPTER 5: CONCLUSION AND RECOMMENDATIONS .....</b>		<b>119</b>
5.1	Conclusion .....	119
5.2	Suggestions and Recommendations .....	122
References .....		123
List of Publications and Papers Presented .....		144

## LIST OF FIGURES

Figure 2.1: Schematic diagram of three-electrode PEC water splitting cell.....	13
Figure 2.2: Illustration of PEC water splitting principal.....	14
Figure 2.3: The crystal structure of ZnO; (a) cubic rocksalt, (b) cubic zinc blende, and (c) tetragonally hexagonal wurtzite structure. ....	16
Figure 3.1: The overview of research methodology .....	39
Figure 3.2: Schematic diagram of electrodeposition process for synthesizing ZnO film. ....	42
Figure 3.3: Schematic diagram of experimental set up for synthesizing of TiO <sub>2</sub> nanoparticles. ....	44
Figure 3.4: Annealing profile.....	45
Figure 4.1: FESEM images of (a) x100k magnification of ZnO nanostructure before heat treatment; and (b) x100k magnification of ZnO nanostructure; after heat treatment (400°C). ....	57
Figure 4.2: HRTEM images for annealed (400°C) ZnO nanostructure film.....	57
Figure 4.3: XRD pattern of as-prepared ZnO, 200°C, 300°C, 400°C, 500°C, 600°C, 700°C, and 800°C annealing temperature .....	60
Figure 4.4: Photocurrent response for as-prepared ZnO film, 200°C, 300°C, 400°C, 500°C, 600°C, and 700°C annealing temperature under UV ray. ....	63
Figure 4.5: Photocurrent response for as-prepared ZnO film, 200°C, 300°C, 400°C, 500°C, 600°C, and 700°C annealing temperature under visible light. ....	63
Figure 4.6: FESEM image of (a) 6k magnification of nanodisk-dendritic ZnO; (inset) 20k magnification of stacked hexagonal-shape nanodisk ZnO, and (b) 10k magnification of nanodisk dendritic ZnO (inset) 100k magnification hexagonal-shape nanodisk ZnO....	66
Figure 4.7: XRD pattern of as-prepared ZnO and annealed ZnO nanodisk-dendritic....	68
Figure 4.8: Photocurrent response for nanodisk-dendritic ZnO, as-prepared ZnO under UV ray and nanodisk-dendritic ZnO without illumination. ....	70
Figure 4.9: Photocurrent response for nanodisk-dendritic ZnO, as-prepared ZnO under visible light and nanodisk-dendritic ZnO without illumination.....	71

Figure 4.10: FESEM images of ZnO nanostructures (a) 40°C, (b) 50°C, (c) 60°C, (d) 70°C, (e) 80°C, (f) 90°C, and (g) 100°C electrolyte bath temperature. ....	74
Figure 4.11: Schematic diagram of ZnO nanostructure mechanism under the influenced of reaction temperature adapted from “Effect of Bath Temperature on the Electrodeposition Mechanism of Zinc Oxide Film from Zinc Nitrate Solution” by Otani <i>et. al.</i> (2006). Copyright 2014 by the authors. ....	75
Figure 4.12: FESEM images of ZnO nanostructures at (a) 15 min, (b) 30 min, (c) 60 min, (d) 90 min, and (e) 120 min exposure time.....	78
Figure 4.13: Formation of the ZnO.....	79
Figure 4.14: FESEM images (a) 1V of electrodeposition applied potential; (b) 2V of electrodeposition applied potential; (c) 3V of electrodeposition applied potential; and HRTEM image (d) 1V of electrodeposition applied potential.....	82
Figure 4.15: Raman spectra for 1 V, 2 V, and 3 V (excitation: $\lambda = 514$ nm). ....	85
Figure 4.16: The XRD pattern for ZnO nanorod for 1 V applied potential. ....	85
Figure 4.17: PL spectra for sample 1V, 2V, and 3V (excitation: $\lambda = 325$ nm).....	87
Figure 4.18: Photocurrent response for 1V, 2V, and 3V under UV ray. ....	89
Figure 4.19: Photocurrent response for 1V, 2V, and 3V under visible illumination. ....	89
Figure 4.20: FESEM micrographs of TiO <sub>2</sub> synthesized at different reaction temperatures, (a) Room temperature, (b) 40°C, (c) 60°C, and (d) 80°C.....	91
Figure 4.21: XRD patterns of the TiO <sub>2</sub> synthesized at different reaction temperatures: room temperature, 40°C, 60°C, and 80°C. [A: Anatase, and B: Brookite] .....	92
Figure 4.22: FESEM images of TiO <sub>2</sub> nanoparticles at (a) 60 rpm, (b) 125 rpm, (c) 350 rpm, (d) 700 rpm, and (e) 900 rpm.....	94
Figure 4.23: XRD patterns of the TiO <sub>2</sub> synthesized at different stirring speed 60 rpm, 125 rpm, 350 rpm, 700 rpm, and 900 rpm. [A: Ananatse].....	96
Figure 4.24: FESEM for dip-coating of TiO <sub>2</sub> onto ZnO nanostructure at exposure time (a) 15 min, (b) 30 min, and (c) 60 min .....	99
Figure 4.25: XRD patterns for exposure time dip-coating of TiO <sub>2</sub> nanoparticles onto ZnO nanostructure 15 min, 30 min, and 60 min. [Z: ZnO, and T: TiO <sub>2</sub> ].....	100

Figure 4.26: FESEM images with 100k magnification (a) ZnO nanostructure, (b) 0.25 at% TiO <sub>2</sub> -ZnO, (c) 0.50 at% TiO <sub>2</sub> -ZnO, and (d) 1.0 at% TiO <sub>2</sub> -ZnO and HRTEM image for TiO <sub>2</sub> -ZnO. ....	102
Figure 4.27: XRD pattern of 0.25 at% TiO <sub>2</sub> -ZnO, 0.50 at% TiO <sub>2</sub> -ZnO, 1.0 at% TiO <sub>2</sub> -ZnO and pure ZnO. [Z: ZnO and T: TiO <sub>2</sub> ]. ....	104
Figure 4.28: Raman scattering for ZnO nanostructure, 0.25 at% TiO <sub>2</sub> -ZnO, 0.5 at% TiO <sub>2</sub> -ZnO, and 1.0 at% TiO <sub>2</sub> -ZnO. ....	106
Figure 4.29: Full XPS survey spectra of ZnO, 0.25 at% TiO <sub>2</sub> -ZnO, and 1.0 at% TiO <sub>2</sub> -ZnO. ....	109
Figure 4.30: XPS spectra of Zn2p for ZnO, 0.25 at% TiO <sub>2</sub> -ZnO, and 1.0 at% TiO <sub>2</sub> -ZnO. ....	109
Figure 4.31: XPS spectra of O1s for TiO <sub>2</sub> , 0.25 at% TiO <sub>2</sub> -ZnO, 1.0 at% TiO <sub>2</sub> -ZnO, and ZnO. ....	110
Figure 4.32: XPS spectra Ti2p for TiO <sub>2</sub> , 0.25 at% TiO <sub>2</sub> -ZnO, and 1.0 at% TiO <sub>2</sub> -ZnO. ....	110
Figure 4.33: PL spectra for sample (a) pure ZnO, (b) 0.25 at% TiO <sub>2</sub> -ZnO, (c) 0.50 at% TiO <sub>2</sub> -ZnO, and (d) 1.0 at% TiO <sub>2</sub> -ZnO (excitation: $\lambda = 325$ nm). ....	112
Figure 4.34: Photocurrent response for (a) pure ZnO, (b) 0.25% TiO <sub>2</sub> -ZnO, (c) 0.50 at% TiO <sub>2</sub> -ZnO, and (d) 1.0 at% TiO <sub>2</sub> -ZnO under UV ray. ....	113
Figure 4.35: Photocurrent response for (a) pure ZnO, (b) 0.25 at% TiO <sub>2</sub> -ZnO, (c) 0.50 at% TiO <sub>2</sub> -ZnO, and (d) 1.0 at% TiO <sub>2</sub> -ZnO under visible light. ....	114
Figure 4.36: Photoconversion efficiency for pure ZnO, 0.25 at% TiO <sub>2</sub> -ZnO, 0.50 at% TiO <sub>2</sub> -ZnO, and 1.0 at% TiO <sub>2</sub> -ZnO under UV ray. ....	115
Figure 4.37: Photoconversion efficiency for pure ZnO, 0.25 at% TiO <sub>2</sub> -ZnO, 0.50 at% TiO <sub>2</sub> -ZnO, and 1.0 at% TiO <sub>2</sub> -ZnO under visible light. ....	115
Figure 4.38: UV-DR Spectra for pure ZnO, 0.25 at% TiO <sub>2</sub> -ZnO, 0.50 at% TiO <sub>2</sub> -ZnO, and 1.0 at% TiO <sub>2</sub> -ZnO. ....	117
Figure 4.39: Illustration of staggered bandgap (type II) hybrid TiO <sub>2</sub> -ZnO film semiconductor and its photo-induced charge transfer and separation. ....	117
Figure 4.40: MS spectra of samples ZnO and 0.25at% TiO <sub>2</sub> -Zn. ....	118

## LIST OF TABLES

Table 2.1: The advantages and disadvantages between synthesis techniques to obtain ZnO nanostructure .....	24
Table 2.2: The previous studies of hybrid TiO <sub>2</sub> -ZnO formation based on different technique. ....	35
Table 3.1: Raw materials and chemicals used for the preparation of TiO <sub>2</sub> -ZnO nanostructures and PEC performance evaluation. ....	40
Table 4.1: Average compositional ratio of as-prepared, 200°C, 300°C, 400°C, 500°C, 600°C, 700°C, and 800°C annealing temperature of ZnO nanostructure using EDX spectroscopy.....	57
Table 4.2: Crystallite size of as-prepared ZnO, 200°C, 300°C, 400°C, 500°C, 600°C, 700°C, and 800°C annealing temperature .....	60
Table 4.3: The photocurrent density (mA/cm <sup>2</sup> ) for as-prepared ZnO and different annealing temperatures under UV ray and visible light.....	64
Table 4.4: Average compositional ratio of nanodisk dendritic ZnO and as-prepared ZnO using EDX spectroscopy analysis. ....	67
Table 4.5: Average compositional ratio of ZnO nanostructures at 40°C, 50°C, 60°C, 70°C, 80°C, 90°C, and 100°C electrolyte bath temperature. ....	75
Table 4.6: Average compositional ratio for 1 V, 2 V, and 3 V applied potential from EDX spectroscopy.....	83
Table 4.7: Average value for length, diameter and aspect ratio for different applied potential.....	83
Table 4.8: Compositional ratio of TiO <sub>2</sub> synthesized at different reaction temperatures: (a) room temperature, (b) 40°C, (c) 60°C, and (d) 80°C.....	91
Table 4.9: Diffraction peak position (°), FWHM, and crystallite size (Å) for TiO <sub>2</sub> synthesized at different reaction temperatures. ....	93
Table 4.10: Compositional ratio of TiO <sub>2</sub> synthesized at different reaction temperatures: (a) 60 rpm, (b) 125 rpm, (c) 350 rpm, (d) 700 rpm, and (e) 900 rpm. ....	95
Table 4.11: Diffraction peak position (°), FWHM, and crystallite size (Å) for TiO <sub>2</sub> synthesized at different stirring speed.....	97

Table 4.12: Crystallite size ( $\text{\AA}$ ) for dip-coating $\text{TiO}_2\text{-ZnO}$ synthesized at different exposure time. ....	100
Table 4.13: Average compositional ratio for pure ZnO, 0.25 at% $\text{TiO}_2\text{-ZnO}$ , 0.50 at% $\text{TiO}_2\text{-ZnO}$ , and 1.0 at% $\text{TiO}_2\text{-ZnO}$ using EDX spectroscopy analysis. ....	103
Table 4.14: The average value of length, diameter and aspect ratio for pure ZnO, 0.25 at% $\text{TiO}_2\text{-ZnO}$ , 0.50 at% $\text{TiO}_2\text{-ZnO}$ , and 1.0 at% $\text{TiO}_2\text{-ZnO}$ . ....	103
Table 4.15: Summary of XPS spectra for $\text{Zn}2p_{3/2}$ , $\text{Ti}2p_{1/2}$ , $\text{Ti}2p_{3/2}$ , and $\text{O}1s$ for samples $\text{TiO}_2$ , 0.25 at% $\text{TiO}_2\text{-ZnO}$ , 1.0 at% $\text{TiO}_2\text{-ZnO}$ , and ZnO. ....	111
Table 4.16: The photocurrent density ( $\text{mA}/\text{cm}^2$ ) for pure ZnO, 0.25 at% $\text{TiO}_2\text{-ZnO}$ , 0.50 at% $\text{TiO}_2\text{-ZnO}$ , and 1.0 at% $\text{TiO}_2\text{-ZnO}$ under UV ray and visible light. ....	114

University of Malaysia

## LIST OF SYMBOLS AND ABBREVIATIONS

IPCC	:	Intergovernmental Panel on Climate Change
EPA	:	Environmental Protection Agency
PEC	:	Photoelectrochemical
ZnO	:	Zinc oxide
TiO <sub>2</sub>	:	Titanium dioxide
CNT	:	Carbon nanotubes
PEM	:	Polymer electrolyte membrane
MRs	:	Membrane reactors
WE	:	Working electrode
CE	:	Counter electrode
RE	:	Reference electrode
<i>hν</i>	:	Photon
PVP	:	Polyvinylpyrrolidone
CVD	:	Chemical vapor deposition
PECVD	:	Plasma-enhanced chemical vapor deposition
MOCVD	:	Metal organic chemical vapor deposition
ALD	:	Atomic layer deposition
PANI	:	Polyaniline
VB	:	Valence band
CB	:	Conduction band
FESEM	:	Field emission scanning electron microscopy
EDX	:	Energy dispersive X-ray
HRTEM	:	High resolution transmission electron microscopy
XRD	:	X-ray diffraction

XPS	:	X-ray photoelectron spectroscopy
PL	:	Photoluminescence
UV-DR	:	UV-Vis diffuse reflectance spectroscopy
DI	:	Deionized water
DC	:	Direct current
TTIP	:	Titanium(IV) isopropoxide
1D	:	One dimensional
2D	:	Two dimensional
3D	:	Three dimensional
FHWM	:	Full width at half maximum
UV	:	Ultraviolet
rpm	:	Revolution per minute

University of Malaya

## CHAPTER 1: INTRODUCTION

### 1.1 Introduction

Behind the rapid development of social, economy and technology, energy becomes a crucial issue around the globe. Global warming devastation occurs from time to time and becoming severe in the 21st century. Abrupt climate change happens around the world. Intergovernmental Panel on Climate Change (IPCC), which is the responsible body to control the variation in global temperature, has announced that the global temperature has increased between 0.4 to 0.8 °C over the past century (United States Environmental Protection Agency (EPA), 2001). Based on records dating back to 1880 by NASA, the earth's surface temperature was the warmest in 2015 (NASA, 2016). Global warming occurred as a result of greenhouse effect due to the increase in atmosphere temperature (Jian-Bin *et al.*, 2012). As the earth's surface temperature rises, the amount of heat the surface radiates will increase rapidly. As long as greenhouse gas concentrations continue to rise, the amount of absorbed solar energy will continue to exceed the amount of thermal infrared energy that can escape to space. The energy imbalance will continue to grow, and the earth's surface temperatures will continue to rise (NASA, 2014). Greenhouse gases emissions were mostly caused by the combustion of fossil fuels. In North Atlantic, the atmospheric circulation above Greenland changed abruptly because of the excessive carbon dioxide gas produced (Bond *et al.*, 1997; Jian-Bin *et al.*, 2012).

In addition, the increasing greenhouse gas concentration of the atmosphere was causing droughts over the areas from the coast of Eastern Africa through the Arabian Sea, to South Asia and East Asia and South China. Meanwhile, stalagmite formations which are closely associated to the Northern Atlantic cold events (ice-rafted debris events) have been reported in 2005-2009 (Kirkby, 2007; S. Wang, 2009; Y. Wang *et al.*, 2005). Global warming in the 21st century resulted in the melting of remaining ice masses, which led to rising water (sea/river) levels. IPCC forecasts global mean sea levels (GMSLs) are likely

to increase with the variation of 4-5 mm/year by 2050, 0.5-0.9 m by 2100; henceforth the losses of up to 30% of coastal wetlands (Devoy, 2014). Major heat sources, such as net heating generated by human activities, geothermal heat flow, the exploitation of nuclear energy and non-renewable energy produced additional heat in the world (Nordell, 2003). These driving forces lead the researchers to reduce the greenhouse effect and environmental protection by presenting creative ideas. Therefore, many parties have tried to create alternative energy substitutes to the current energy sources around the world. One of the alternatives taken by many countries is hydrogen gas. In the 21st century, the transition of fuel usage from liquid to gas, commonly known as the hydrogen economy, for future sustainability of fuel and hydrogen-based economies will have an impact on all sectors in the long term. Up to the present time, hydrogen has been selected as one of the potential future energy carrier. To secure future clean and sustainable clean energy, hydrogen energy is possibly the best substitute for fossil fuel. Currently, fossil fuels, methane, and coal gasification are the main sources for hydrogen production (Ogden, 1999). The large scale production of hydrogen gas will have an influence on energy efficiency and an impact on the environment and. Therefore, PEC water splitting system for the generation of hydrogen is an attractive area of research.

In fact, hydrogen is a captivating clean fuel when engendered from water and the energy required to form it can be obtained by utilizing our solar energy (Weidenkaff *et al.*, 2000). Thus, solar-driven PEC water splitting system merges numerous captivating features for energy utilization. PEC water spitting is a novel system for hydrogen production. In fact, PEC water splitting produces hydrogen without carbon emission that is also renewable (S Licht *et al.*, 2000). Briefly, PEC water spitting is a chemical reaction forming oxygen ( $O_2$ ) and hydrogen ( $H_2$ ) from water via direct

thermal dissociation at above 2500 K (Bilgen *et al.*, 1977; Fletcher & Moen, 1977; Kogan, 1998).

Recently, a semiconductor which can be used as a photoelectrode has been developed to harvest hydrogen in a large scale. Among the semiconductor based photoelectrodes, metal oxide is one of the most promising materials that is able to utilize our solar illumination for hydrogen production via PEC water splitting process. Its promising characteristics such as easily available, stable against chemical and corrosion, inexpensive, as well as non-toxic in nature makes it an important candidate for photocatalysis and PEC water splitting application (Fierro, 2005). Theoretically, a suitable semiconductor photoelectrode for hydrogen production must fulfil several basic criteria, such as being high photochemically stable in aqueous solution, responsive to solar-irradiation, and having the oxidation and reduction potential that is equivalent to the valence and conduction band of the semiconductor

The exceptional chemical and physical properties of ZnO photoelectrode have been long recognized since 1960 (Z. L. Wang, 2004). As a direct semiconductor, ZnO has the advantage of a 3.37 eV band-gap and produces electronic properties such as exciton binding energy of 60 meV near UV emission, transparent conductivity and piezoelectricity has led to many optoelectronic applications especially in gas, chemical and biosensors, field effect transistor, transducer, dye-sensitized solar cells, and PEC water splitting. Moreover, ZnO is a biocompatible and bio-safe material for many medical applications without any modifications (Fierro, 2005; Shaheen *et al.*, 2013). Additionally, its radiation hardness can be applied at high altitudes or even in space with its transparent and conductive properties (Abd-Ellah *et al.*, 2013; Janotti & Van de Walle, 2009; Ma *et al.*, 2011; Z. Zheng *et al.*, 2013).

Lately, design and development of nanostructure of ZnO has gained significant scientific interest and become the most studied material as it exhibits promising functional

properties, especially one-dimensional (1D); nanocombs (T. Xu *et al.*, 2012), nanowires (Kołodziejczak-Radzimska & Jesionowski, 2014; Nikoobakht *et al.*, 2013; Tien *et al.*, 2008), nanobelts (Y. Huang *et al.*, 2006; Pan *et al.*, 2001), nanotubes (W. Chen *et al.*, 2007; J. Liu *et al.*, 2005; J.-J. Wu *et al.*, 2002), nanospring and ring (Kong *et al.*, 2004), nanoribbon, nanohelices, nanoneedle (Wahab *et al.*, 2007) and nanorod (Banerjee *et al.*, 2003; Frade *et al.*, 2012; Hahn, 2011), two-dimensional (2D); nanopellets and nanosheets (Chiu *et al.*, 2010; Jose-Yacaman *et al.*, 2005), and three dimensional (3D) dendrites, flower, dandelion, coniferous, and snowflakes (Abd Samad *et al.*, 2015b; Bitenc & Orel, 2009; Kołodziejczak-Radzimska & Jesionowski, 2014; J. Liu *et al.*, 2006; Lu *et al.*, 2013; Polshettiwar *et al.*, 2009; Xie *et al.*, 2005).

Based on the discussion above, the main focus of this study, is the formation of 1D ZnO nanorod and its morphology, element composition, crystallinity, and PEC water splitting responses. A convincing motivation arose from the benefits of a 1D ZnO nanorod because the mobility of electrons was crucial for the formation of hydrogen gas via the reduction reaction of hydrogen ions ( $H^+$ ). Thus, 1D ZnO nanorod film was selected for this research purpose due to its anisotropic mobility of electrons. Indeed, the electron mobility increased with the decrease of density for electrons available to scatter. Based on the literature, many researchers concluded that electron mobility behaviour could generate better transport of photogenerated charge carriers within the 1D nanorod's one-dimensional wall surface. Simultaneously, 1D nanorod prevents backward reactions and therefore reduced the number of recombination centres.

However, ZnO-based photoelectrode is still far from becoming a potential candidate for solar driven PEC water splitting. The low active surface area for photon absorption from illumination and fast recombination losses of photo-induced charge carriers remain as a great challenge for researchers in this area. Thus, in order to

obtain the right dimensions and morphologies of ZnO photoelectrode, a controlled synthesis procedure for the production of 1D ZnO nanorod must be investigated and optimized. As such, considerable efforts have been devoted to tuning the responsiveness of ZnO from UV into visible light region by coating an optimum amount of TiO<sub>2</sub> nanoparticles on ZnO. In fact, TiO<sub>2</sub> nanoparticles have been comprehensively studied and utilised in many technological applications due to its outstanding physicochemical properties, such as thermal and chemical stability, relatively high photocatalytic activity, low toxicity and cost (H. Xu *et al.*, 2008). These properties have found a wide range of applications in numerous areas, including cosmetics and sunscreen formulations (Han *et al.*, 2012) ceramics (Fostad *et al.*, 2009), dye-sensitized solar cells (Grätzel, 2001; Shin *et al.*, 2011), and solar-based drinking water treatment (Salih & Pillay, 2007).

In this study, anatase phase TiO<sub>2</sub> nanoparticles (tetragonal, 3.894 g/cm<sup>3</sup>) was selected as potential coating for the modification of ZnO nanostructure. It is a well-known fact that the anatase phase of TiO<sub>2</sub> can be perceived as an arrangement of parallel octahedral; TiO<sub>2</sub> is stable in aqueous media and is tolerant of both acidic and alkaline solutions (Bagheri *et al.*, 2012; SHAHAB *et al.*, 2013). For the reason of large surface area per unit mass and volume, anatase phase of TiO<sub>2</sub> can be performed to have the highest photocatalytic activity compared to the other phase when coated on the ZnO nanostructure (brookite phase and rutile phase) (Bagheri *et al.*, 2012; Chaturvedi *et al.*, 2012). In this manner, coating ZnO with TiO<sub>2</sub> nanoparticles that possess different redox energy level in TiO<sub>2</sub>-ZnO heterostructures, provides another attractive approach in achieving a more efficient charge separation under visible light. Therefore, a hybrid of TiO<sub>2</sub>-ZnO nanostructure, acting as a photoelectrode in PEC water splitting system has been developed in this study. Results suggest that the hybrid TiO<sub>2</sub>-ZnO nanostructure film demonstrate significant advantages of promoting the separation of electron/hole pairs and responsiveness to the visible light in PEC water splitting system.

## 1.2 Problem statement

Since scientific studies of ZnO have been established in the early of 20th century, it has become one of the most widely used materials due to its unique physio-chemical properties. To date, 1D structure of ZnO nanostructure using electrodeposition technique (Pradhan *et al.*, 2009) under a specific set of environment conditions have been widely reported. As discussed in previous section, ZnO is still far from becoming a suitable candidate for PEC water splitting application. The poor visible-light absorption and high recombination losses of charge carriers have restricted the widespread use of ZnO in PEC water splitting application. In fact, ZnO can only effectively function under UV region ( $\lambda < 400$  nm) which contain only about 4-5% of UV rays from our solar energy. Thus, utilization of visible light from solar energy (40-45%) is essential that lead to the higher photoconversion efficiency in solar-driven water-splitting applications. Thus, in order to produce high efficient solar-driven PEC water splitting system using ZnO as a photoelectrode is very challenging unless the above mentioned issues are addressed. The strategies to get the right dimensions and morphologies, a controlled synthesis procedure for the production of ZnO must be investigated and optimized in detail. Generally, ZnO results in undesirable ZnO structures (non-uniformity of ZnO morphology) problems, which significantly decrease its photocurrent density and photoconversion efficiency performance. Considerable efforts have been exerted to minimize the recombination losses of charge carriers and extend the spectral response of ZnO nanostructure to visible spectrum by incorporating an optimum amount of TiO<sub>2</sub> nanoparticles into the ZnO nanostructure wall surface. The incorporation of TiO<sub>2</sub> on the ZnO nanostructure wall surface may create impurity energy levels that can facilitate better absorption in the visible light region and further minimize the recombination losses of charge carriers.

### **1.3 Objectives of Research**

The objectives of this study are listed as follow:

- To synthesize hybrid TiO<sub>2</sub>-ZnO nanostructure film via dip-coating technique (formation of TiO<sub>2</sub>-ZnO), electrodeposition technique (formation of ZnO), and precipitation peptization technique (formation of TiO<sub>2</sub>).
- To evaluate the PEC water splitting performance of hybrid TiO<sub>2</sub>-ZnO nanostructure film as compared to the ZnO nanostructure film under illumination (e.g, UV ray and visible light).

### **1.4 Outline of Research Work**

There are six stages of experiment in this research work. Stage one covers the materials and chemical procurement. Stage two illustrates the synthesis work of ZnO nanostructures (nanodisk, nanorod, nanodisk-dendritic). The secondary semiconductor; TiO<sub>2</sub> nanoparticles production will be shown in stage three. Stage four will show the formation of hybrid TiO<sub>2</sub>-ZnO nanostructure film. Stage five will present their characterization, and lastly stage six presents the PEC water splitting performance evaluation under illumination.

### **1.5 Thesis overview**

This thesis is organized into five chapters. Chapter 1 includes the introduction of this research work, problem statement, objectives of research, research work outline and outline of thesis. Chapter 2 covers the importance of hydrogen, history of PEC water splitting, the principal behind the PEC water splitting, the engineering of ZnO and its advantages and disadvantages, the modification of ZnO and tuning its photocatalytic performance into visible light region, and whilst the last section of Chapter 2 presents comprehensive literature on the TiO<sub>2</sub>-ZnO composite. Chapter 3 contains the raw

materials selection, methodologies for catalysts characterization, and PEC water splitting testing performance. The results obtained and discussion will be discussed in Chapter 4. Lastly, Chapter 5 summarizes the conclusion of study and several suggestions and recommendations.

University of Malaya

## CHAPTER 2: LITERATURE REVIEW

Comprehensive review will be presented in this chapter which covers the following topics: 1) importance of hydrogen, 2) principal of PEC water splitting system, 3) ZnO nanostructures, 4) crystallization of ZnO, 5) modification of ZnO nanostructures, and 6) hybrid TiO<sub>2</sub>-ZnO nanostructure film as photoelectrode.

### 2.1 Importance of hydrogen

The rapid growth of gross domestic product for each country has a close relation with global warming phenomena and climate change issues. The global warming and climate change aspects have drawn the attention especially in the field of science, economic, social, and politics and it has been discussed actively in the past hundred years (Chiroma *et al.*, 2015; Cicea *et al.*, 2014; Tang *et al.*, 2012). The climate change mitigation has been studied by all continents due to the abnormal change in geography, meteorological, and the emerging of diseases. Many researchers found that global warming (climate change issue) is mostly affected by the fast expansion of energy production and consumption. The carbon dioxide (CO<sub>2</sub>) emission increased with energy consumption. Currently, coal contributed around 30-40% of CO<sub>2</sub> emission from fossil fuels, whilst sulfur dioxide (SO<sub>2</sub>) or NO<sub>x</sub> contributed to acid rain (Kaygusuz, 2009; Ozyurt, 2010).

In the effort to ensure the environmental efficiency index could be achieved, a clean and sustainable hydrogen energy has been introduced by researchers around the world. The hydrogen energy intensity is one of the econometric model to promote sustainable clean energy supply. So far, a low degree of environmental efficiency (in green energy) has been recognized for certain countries. However, countries like United States, Japan and European Union countries have reached the desired environmental efficiency (Cicea *et al.*, 2014). Hydrogen energy could be considered as a low-cost and no-carbon-emission energy. Therefore, hydrogen energy would contribute to the

significant improvement in achieving desired environmental efficiency. Under those circumstances, many techniques were studied for the hydrogen generation. Some of the techniques are pyrolysis and steam reforming of biomass (Parthasarathy & Sheeba, 2015), photo-reforming of organics (Clarizia *et al.*, 2014), methanol steam reforming (Iulianelli *et al.*, 2014), ammonia decomposition via reactor technology (Chiuta *et al.*, 2013), membrane reactor (Iulianelli *et al.*, 2014), borohydride hydrolysis reaction (B. H. Liu & Li, 2009), and solar-driven water splitting system (George *et al.*, 2015; Hu *et al.*, 2009).

Future hydrogen generation can be generated from thermochemical techniques. Fast pyrolysis can be classified as modern thermochemical technology. This technology is followed by bio-oil steam reforming, purification of water, and steam gasification. Nevertheless, slow pyrolysis also can be engaged with steam gasification for hydrogen generation (Parthasarathy & Sheeba, 2015). Equally important, ammonia decomposition for hydrogen generation has also been actively studied, and there are two types of technology for the decomposition of ammonia. The first technology use Ruthenium (Ru), which is known as good catalyst, together with carbon nanotubes (CNT) aided as support, and potassium hydroxide as best promoter for ammonia decomposition. High dispersion of Ru promotes excellent catalytic activity. In addition, the CNT basicity and conductivity gave better performance to high efficiency catalyst (Yin *et al.*, 2004). Second technology relates to ammonia decomposition through reactor technology. Too many efforts have been done to produce portable and distributed power generation from this technology. This technology also called as load-shedding technology (Chiuta *et al.*, 2013). Over the past decade, reactor design including operability, capacity of power generation, and efficiency were the main focus. In a more advanced research, microreactors and monolithic reactors offer more advantages in many ways (Chiuta *et al.*, 2013).

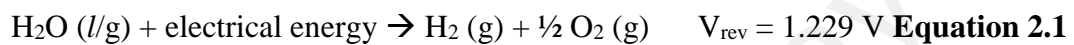
Polymer electrolyte membrane (PEM) assists methanol steam reforming to produce high purity hydrogen. This technology is also known as inorganic membrane

reactor. There are three types of membrane reactors (MRs); membrane reactors, palladium-based MRs, and proton exchange membrane fuel. MRs can be categorized as photo catalytic MRs (Mozia, 2010), zeolite MRs (Fong *et al.*, 2008; McLeary *et al.*, 2006), polymeric MRs (J. Huang *et al.*, 2005; Scholes *et al.*, 2010), enzyme MRs (Andrić *et al.*, 2010), dense and porous inorganic MRs (Y. Lin, 2001; Westermann & Melin, 2009), electrochemical MRs (Chatenet *et al.*, 2010), and bio medical MRs (Reij *et al.*, 1998; Woodside *et al.*, 1998). Meanwhile, palladium-based membrane should be given special attention as it has less permeability to hydrogen as compared to tantalum, vanadium, and niobium. The last part for methanol steam reforming conversion to hydrogen is proton exchange membrane fuel cells. It involves chemical energy conversion (Peighamardoust *et al.*, 2010). Membrane such as nafion (sulfonated perfluorinated polymer) has great proton conductivity and high applied potential at low-medium temperature (Iulianelli *et al.*, 2014).

Further, organic materials photoreforming become one of the efforts for hydrogen generation. This technology is almost similar to water splitting system where the only difference is the used of sacrificial agents. This technology uses organic materials as sacrificial agent, for instance; methanol, glycerol, and formic acid. However, the most frequently used organic materials are methanol, glycerol, and ethanol. Another key point regarding this technology is the use of single-catalyst or second catalyst in the conversion from organic materials to hydrogen generation. Alkaline medium is needed for hydrogen generation by producing a negative shift of the bands' positions (Chiuta *et al.*, 2013). PEC water splitting system will be discussed in detail in the next section, as this technology has been selected for hydrogen generation in this research work.

## 2.2 Principal of PEC water splitting system

After reviewing all the above technologies, hydrogen generation via PEC water splitting system has been selected due to its low-cost, simple and direct production of hydrogen, and free carbon emission. Additionally, the increased in solar-to-hydrogen efficiency reduced the intrinsic cost. Plus, the abundant resources of sunlight and water (inexhaustible sources) are available. Below is the net reaction for the electrolysis of water splitting:



Referring to the above equation, oxygen as a byproduct is very clean and useful gas [Equation 2.1]. However, water splitting technology so far only meet 3.9% from the world's hydrogen demand (Ewan & Allen, 2005; Grimes *et al.*, 2007). The water splitting Gibbs free energy ( $\Delta G$ ) is positive at standard ambient pressure and temperature. Therefore, the reaction is non-spontaneous. The electrical energy equivalent with the change in Gibbs free energy is required for the reaction to occur (Grimes *et al.*, 2007). The conversion of electrical energy to chemical energy will take place through reaction of charge transfer at electrode-solution interface. The thermodynamic reversible potential,  $V_{\text{rev}}$  is 1.229 V and  $\Delta G$  is 237.178 kJ/mol at 1 bar and 25°C (Grimes *et al.*, 2007; Stull & Prophet, 1971). Since water has poor ionic conductivity, hence water splitting process normally proceeds by addition of alkalis or acids. These aqueous media offer high ionic concentration and mobility of hydrogen and hydroxyl which will produce low electrical resistance. Considering corrosion problem, basic electrolyte is generally preferred than acidic electrolyte (Grimes *et al.*, 2007). Potassium hydroxide (KOH) and sodium hydroxide (NaOH) are preferred as both are strong bases (Grimes *et al.*, 2007).

PEC water splitting is described as light-driven electrolysis process. In particular, light is converted to electrical energy and transformed to chemical energy. By the same

meaning, photoelectrode (semiconductor) absorbed solar energy and the required applied potential is generated to proceed with water splitting process for hydrogen generation. Below is a conventional schematic diagram of three- electrode PEC cell that will be used for further explanation [Figure 2.1].

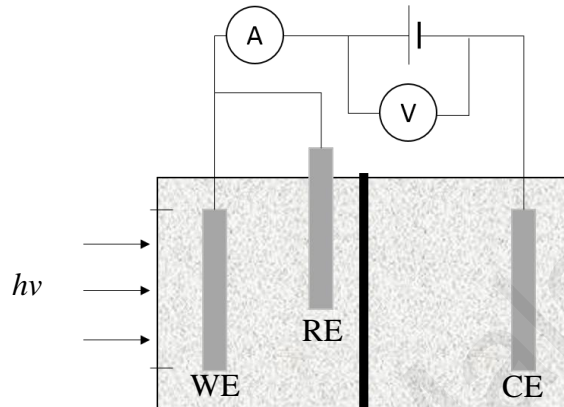


**Figure 2.1: Schematic diagram of three-electrode PEC water splitting cell.**

Where;

WE = Working electrode

CE = Counter electrode

RE = Reference electrode

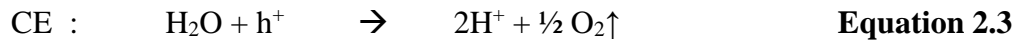
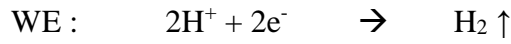
$h\nu$  = Photons

Common PEC cell, WE (semiconductor n-type) produces oxygen and CE (metal) produces hydrogen [Equation 2.2]. Meanwhile, for WE (semiconductor p-type) would produce hydrogen and CE (metal) would produce oxygen [Equation 2.3]. Below equations show the reaction of n-type semiconductor as an photo-anode and p-type semiconductor as a photo-cathode (Grimes *et al.*, 2007).

n-type semiconductor;



p-type semiconductor;



In PEC water splitting, the photoelectrode is illuminated by photon which provides an energy  $h\nu$  that is equal or larger than semiconductor bandgap in order to form charge carriers [Equation 2.4]. Below is the illustration of PEC water splitting principle by considering the n-type semiconductor [Figure 2.2].

At WE;



At CE;

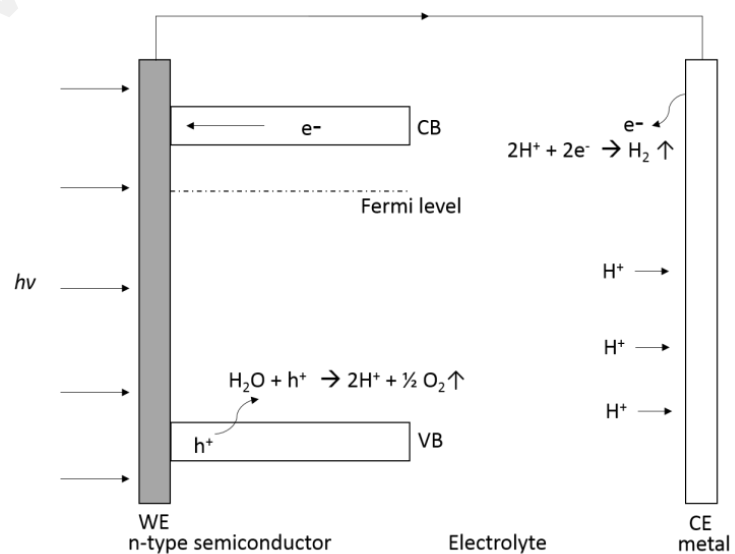
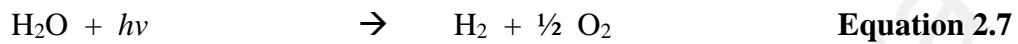


**Figure 2.2: Illustration of PEC water splitting principal.**

At WE and electrolyte interface, the oxygen and  $H^+$  are formed after the reaction of water and photogenerated holes  $h^+$ . Meanwhile, hydrogen ions travel through the electrolyte (internal circuit) to the CE [Equation 2.5]. At the same time in the external circuit, the photogenerated electron (from WE) travels to CE and react with hydrogen ions to become hydrogen gas [Equation 2.6]. Simplified overall reaction is shown as follows [Equation 2.7];



### 2.3 The engineering behind ZnO nanostructures

In order to increase the efficiency of PEC water splitting performance in this research work, ZnO has been selected as a promising photo-anode as compared to other oxide semiconductor materials. ZnO possess excellent electrical, piezoelectric and optical properties. Nevertheless, ZnO always functioned excellently under the blue UV region with a direct bandgap (3.37 eV). Also, it has a large excitation binding energy with value 60 meV at room temperature (Y. J. Kim *et al.*, 2011; Lepot *et al.*, 2007; Park *et al.*, 2002). ZnO existed in three crystal structures; wurtzite, zinc blende, and rocksalt. However, wurtzite is preferred for electronic application as it is thermochemically stable at room temperature compared the other two structures [Figure 2.3] and belongs to space group  $P6_3mc$  (Hermann-Mauguin notation) and  $C_{6v}^4$  (Schoenflies notation).

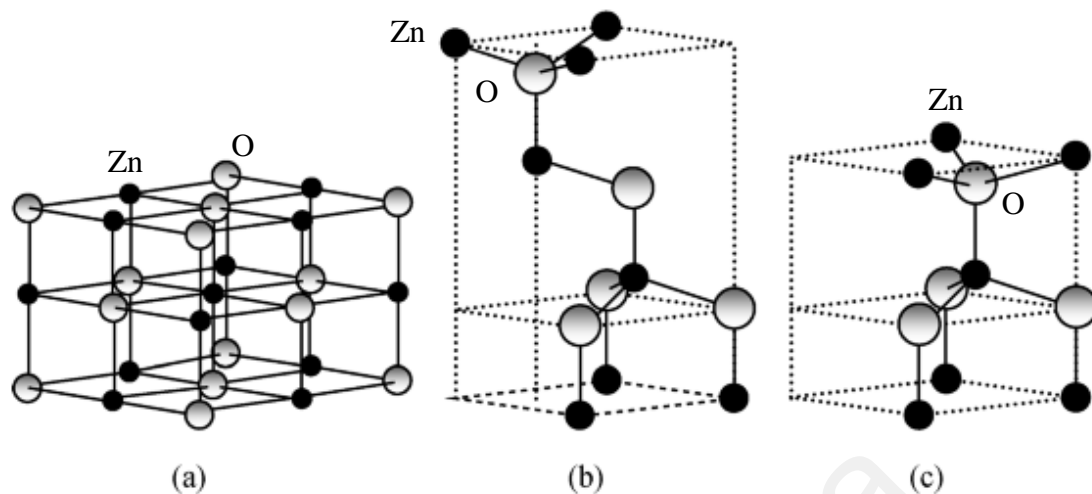


**Figure 2.3: The crystal structure of ZnO; (a) cubic rocksalt, (b) cubic zinc blende, and (c) tetragonally hexagonal wurtzite structure.**

A number of techniques have been successfully studied for the production of ZnO crystals of specific size and shape, such as atomic layer deposition, sol-gel, hydrothermal, solvothermal, electrodeposition, and chemical vapor deposition. Also, studies of different surfactants have been instigated for the formation of ZnO nanocrystals with various shapes and structures (Lévy-Clément *et al.*, 2005; Ramírez *et al.*, 2010; Wong *et al.*, 2003; Yiamsawas *et al.*, 2009). The use of surfactants leads to highly complicated reaction and the use of additives are environmentally unfriendly in large-scale industrial production. Therefore, an additive-free technique has been developed to prepare ZnO nanostructures; especially from commercially available zinc acetate precursor for solution-phase reactions. In this case, additive-free ZnO nanostructures were prepared by using simple solution phase technique, autoclave and microwave oven. The annealing effects on the morphology and properties at low temperature are discussed in Section 2.4. ZnO has also been listed as safe (GRAS) material by the Food and Drug Administration and can be used as food additive (Espitia *et al.*, 2012).

Series of fabrication technique of wurtzite ZnO nanostructures share the common growth conditions which lead to the controllable wurtzite ZnO nanostructures formation. By controlling the growth kinetics, it is possible to change the growth behaviour of

wurtzite ZnO nanostructures. The crucial variables for the formation of wurtzite ZnO nanostructures are; the pH of the electrolyte for the solution-based synthesis technique (sol-gel, hydrothermal, solvothermal, electrodeposition, and chemical bath deposition); pH 5 - 6. However, certain findings showed that ZnO nanostructures might be produced in basic solution with pH of 9-13. In addition, reaction temperature could be considered as the main variable that could affect the formation of wurtzite ZnO nanostructures. Most of the studies stated that the formation of wurtzite ZnO nanostructures started between the temperature of 500°C - 800°C for physical and chemical vapour deposition techniques.

Meanwhile, for the solution-based synthesis, the appropriate deposition temperature for the formation of wurtzite ZnO nanostructures is between 70 °C – 80 °C. The temperature control has significant effect towards 70 °C due to the inadequate bulk oxygen atom diffusion at room temperature. 0.001- 0.1 M of the concentration of zinc ion in solution-based synthesis technique was sufficient for the formation of wurtzite ZnO nanostructures. Other than that, the presence of catalyst (such as Au, Fe, and Sn) could assist the direction of ZnO nanostructures growth and diameter of nanostructures. But, the growth of nanostructures might be terminated when it reached the eutectic point of catalyst alloys or reactant. On the other hand, the selection of substrates has become one of the essential elements in the formation of wurtzite ZnO nanostructures, because the process of crystal growth for certain orientation on top of another crystal was influenced by the substrate surface. Consideration on the crystallographic structure together with the surfaces to be used and the atomic termination and charge status of the substrate could definitely affect the morphology of the grown nanostructures. Modifying the ageing or deposition time as a matter of fact could give different result of the synthesized ZnO nanostructures.

### **2.3.1 Synthesis of ZnO nanostructures**

#### **2.3.1.1 Synthesis of ZnO nanostructures from sol-gel technique**

According to Bahadur and co-researchers, the selection of precursor materials in sol-gel technique are crucial because it could determine the future morphology of ZnO nanostructures. Besides, authors also stated that the nitrate ions formed an agglomeration or islands like dendrite structure and acetate ions could produce a smooth character and uniform ZnO nanostructures. Moreover, nitrate ions produced a smaller crystallite size of ZnO nanostructures as compared to acetate ions as precursor. This situation occurred because the increase in basicity in nitrate ions electrolyte produced random and rapid crystallization ZnO nanostructures (Bahadur *et al.*, 2007). Furthermore, sol-gel technique might produce an enhancement of preferential growth for subsequent-deposited process. Therefore, a highly topotactic in *c*-axis growth of ZnO nanostructures will be produced (Bornand & Mezy, 2011).

#### **2.3.1.2 Synthesis of ZnO nanostructures from hydrothermal technique**

Aqueous solutions-based hydrothermal technique is recognized as a potential technique for the formation of ZnO nanostructures. In fact, this technique normally produces a nanostructures with narrow size particle distribution, high-quality growth orientation, and good crystallization (Aziz *et al.*, 2014; S. Dai *et al.*, 2013; Y. J. Kim *et al.*, 2011). However, directing agent is needed to nucleate the ZnO nanostructures; which serves as a growth directing agent during the hydrothermal process (Lepot *et al.*, 2007). Besides, the presence of a capping agent; for instance polyvinylpyrrolidone (PVP) is needed in order to achieve the anisotropic growth of nanocrystals. As a result, the surface energy of crystallographic surfaces of ZnO could be altered (J. Du *et al.*, 2005; Park *et al.*, 2002). Also, many literatures have been reported that the reaction time required for hydrothermal is much longer compared to electrodeposition process. Nevertheless,

prolong reaction time would not affect the morphology of ZnO nanostructures because surfactant plays the major role in morphology control compared to reaction time (Lepot *et al.*, 2007).

### 2.3.1.3 Synthesis of ZnO nanostructures from solvothermal technique

Solvothermal is also widely employed to synthesis ZnO nanostructure as its working principle is quite similar with hydrothermal. However, there is a difference in the usage of precursor solution where solvothermal usually used non-aqueous precursor solution. Additionally, solvothermal technique benefits both sol-gel technique (Oliveira *et al.*, 2003) and hydrothermal technique (Andersson *et al.*, 2002). In addition, solvothermal technique allows the controllability of size, shape distribution, and crystallinity of ZnO nanostructures with all these characteristics could be controlled by varying the precursor, surfactant, and solvent used.

Varghese *et al.* reported that ZnO nanostructures can be conveniently prepared under the temperature of 200 – 300 °C. Also, the presence of surfactants in the reaction mixture help to obtain uniform diameter of ZnO nanostructures (Varghese *et al.*, 2007). Similar with hydrothermal technique, the use of polyvinylpyrrolidone (PVP) plays an important role in controlling the ZnO size and shape. Indeed, PVP acts as a template to form chain structures for ZnO crystals. Normally, with the use of polymer template, ZnO could grow up along these chains to form nanostructures. On the other hand, PVP could form a shell surrounding the particles to prevent them from aggregating into larger particles and its steric effect controlled the grain growth (Yiamsawas *et al.*, 2009). As a growth directing agent, PVP led to the morphology control depending on its interaction during the crystal growth (Yiamsawas *et al.*, 2009).

#### 2.3.1.4 Synthesis of ZnO nanostructures from electrodeposition technique

Among various preparation techniques available as mentioned earlier, electrodeposition technique has been commonly used technique for the preparation of ZnO nanostructures. Generally, the main advantage of electrodeposition technique is it offers simpler method for the production of ZnO nanostructures. In addition, low equipment cost, scalability, and facile and precise control of nanostructure and morphology give added advantages of electrodeposition technique (Abd-Ellah *et al.*, 2013). It is well-known that without the use of any surfactant; ZnO nanostructures can be produced via this technique. The ZnO growth produced by using electrodeposition technique from Zn (II) ions and different oxygen precursors is strongly dependent on Zn (II) concentration. In fact, the influence of Zn (II) concentration on the self-assembly, 1D ZnO growth has been extensively reported in many literatures (Q.-P. Chen *et al.*, 2006; Cui & Gibson, 2005; J Elias *et al.*, 2007; Jamil Elias *et al.*, 2008; Könenkamp *et al.*, 2000; Lévy-Clément *et al.*, 2005; Mollar *et al.*, 2006; Ramírez *et al.*, 2010; Ramon Tena-Zaera *et al.*, 2007; R Tena-Zaera *et al.*, 2005; Wong *et al.*, 2003). Most of the literatures concluded that ZnO nanorod could be formed via electrodeposition technique with certain parameters applied.

In summary, the structures produced using electrodeposition technique seems to be strongly dependent on the applied current density. Aziz and co-researchers reported that a very thin layer of nanodot structures was obtained at very low current density of  $-0.1 \text{ mA/cm}^2$ . Further increasing the current density up to  $-0.5 \text{ mA/cm}^2$ , a ZnO layer with nanoporous-like morphological structures could be produced. The authors observed that the diameter (75 – 150 nm) of the nanorod increased drastically when increasing the applied current to  $-1.0 \text{ mA/cm}^2$ , generating almost no space between the nanorods. At the high current density of  $-1.5 \text{ mA/cm}^2$ , the morphology of ZnO nanorod shows no more well-defined hexagonal structure. The reason mainly is attributed to increase in the rate

of all chemical reactions resulting from high dissolution and deposition rate. At high current density of  $-2.0 \text{ mA/cm}^2$ , a ZnO layer of nanocluster structures were formed (Aziz *et al.*, 2014). The reason is higher dissolution and deposition rate produced high conductance value. Therefore, it affects the nucleation densities and morphology (Abd-Ellah *et al.*, 2013; Samad *et al.*, 2016).

#### **2.3.1.5 Synthesis of ZnO nanostructures from chemical vapor deposition (CVD)**

Lately, chemical vapor deposition (CVD) is the most prominent and well-established physical technique that utilizes high temperature ( $700 - 900 \text{ }^\circ\text{C}$ ) to form ZnO nanostructures; especially nanorods. Normally, ZnO nanostructures could be produced via plasma-enhanced chemical vapor deposition (PE-CVD) and metal organic chemical vapor deposition (MO-CVD). In fact, this technique is considered as a high cost technique by most researchers due to expensive equipment needed (Aziz *et al.*, 2014; Y.-J. Kim *et al.*, 2009; Lee *et al.*, 2012). Many researchers reported that temperature plays an important role in the formation of ZnO nanostructures via MO-CVD technique. Normally, the temperatures studied is between the  $200-500\text{v}^\circ\text{C}$ . It affects the growth of ZnO nanostructures especially in the aspect of crystal planes, energy difference, and growth kinetic. Besides that, the transformation of nanostructures from conventional polycrystalline to arranged clusters of ZnO nanostructures can also be observed (Khranovskyy & Yakimova, 2012; K.-S. Kim & Kim, 2003; Saitoh *et al.*, 1999; Sbrockey & Ganesan, 2004; Tompa *et al.*, 2006). Chi *et al.* added that high temperature ( $>900 \text{ }^\circ\text{C}$ ) MO-CVD produced better crystal quality as compared to low temperature. Under high temperature, generally, the samples have higher photon emission efficiencies due to the highest emission quantum efficiency (Chi *et al.*, 2005).

PE-CVD provides layers of deposition at relatively low substrate temperature;  $200 - 300 \text{ }^\circ\text{C}$  (Dobkin & Zuraw, 2003; Kern, 2012). Nevertheless, variables like substrate

temperature, power density, gas pressure, gas composition, and frequency also affect the crystal growth and properties of metal oxide (Grimes *et al.*, 2007).

#### **2.3.1.6 Synthesis of ZnO nanostructures from atomic layer deposition (ALD)**

The ALD technique has already shown its versatility in industrial use for deposition of dielectric and luminescent films for electroluminescent flat panel displays. The big challenge to ALD is to establish a position in microelectronics. It has great potential because of the accurate thickness control in deposition of very thin films and 100% conformity even on high aspect ratio structures (Clavel *et al.*, 2010; Leskelä & Ritala, 2002).

In ALD technique, basic steps are as follows: Firstly the precursors will be located in the growth chamber. When precursors reach the substrate, it will be scattered by purging of inert gas (N<sub>2</sub>). At the same time, the opening and closing of valves will be controlled by computer. Normally, the pressure in the chamber is about 1 – 2 Torr, and it is monitored by vacuum gauge. Meanwhile, the substrate temperature is maintained at ~200 °C for deposition to occur. In order to achieve different thickness and crystallographic, the reaction is repeated up to 1,800 cycles (depend on the requirement) (Solís-Pomar *et al.*, 2011).

Nowadays, plasma activation technique will increase the usability of ALD technique because wider materials can be implemented by using this technique. Plasma-ALD could give promising result that will further improve the existing process (Leskelä & Ritala, 2002). Moreover, nanoparticles from chemistry colloidal can be used as precursor in this technique (Clavel *et al.*, 2010). But, a limitation arise when it relates with electropositive metals (alkaline earth metals, rare earth metals) because they lack of volatile compounds for deposition to occur (Leskelä & Ritala, 2002). Unlike other types of chemical vapor

deposition, ALD proceeds through reactions solely at the surface of the substrate, leading to a self-limiting and layer-by-layer growth (M.-K. Wu *et al.*, 2010). Table 2.1 summarizes the advantages and disadvantages between synthesis techniques to obtain ZnO nanostructure. Based on review, electrodeposition technique has been selected in this research work.

University of Malaya

**Table 2.1: The advantages and disadvantages between synthesis techniques to obtain ZnO nanostructure**

Synthesis methods	Advantages	Disadvantages
Sol-gel method	<ol style="list-style-type: none"> <li>1. Processing temperature is very low (below 100°C) (Wright &amp; Sommerdijk, 2000).</li> <li>2. It is a convenient production technique for any possible shape for film and bulk materials (Wright &amp; Sommerdijk, 2000).</li> <li>3. Can create very fine powders (Carter &amp; Norton, 2007) .</li> </ol>	<ol style="list-style-type: none"> <li>1. High cost of raw materials (Carter &amp; Norton, 2007).</li> <li>2. Shrinkage and cracking occur during drying with high volume (Carter &amp; Norton, 2007).</li> </ol>
Hydrothermal method	<ol style="list-style-type: none"> <li>1. The ability to create crystalline phases which are not stable at the melting point (L. Liu <i>et al.</i>, 2008).</li> <li>2. Can process materials that have a high vapor pressure near melting point (L. Liu <i>et al.</i>, 2008).</li> <li>3. Can produce high quality of crystals while maintaining good control over composition (O'Donoghue, 2006).</li> </ol>	<ol style="list-style-type: none"> <li>1. The need of expensive autoclaves (O'Donoghue, 2006).</li> <li>2. The impossibility of observing the crystal as it grows (O'Donoghue, 2006).</li> </ol>
Solvothermal method	<ol style="list-style-type: none"> <li>1. This method is benefit of both sol-gel method and hydrothermal method (Andersson <i>et al.</i>, 2002).</li> <li>2. Having good control over the size, shape distribution, and crystallinity of nanostructures (Andersson <i>et al.</i>, 2002).</li> </ol>	<ol style="list-style-type: none"> <li>1. The need of expensive autoclaves (O'Donoghue, 2006).</li> <li>2. The use of non-aqueous solution (Oliveira <i>et al.</i>, 2003).</li> </ol>
Chemical bath deposition	<ol style="list-style-type: none"> <li>1. The use of unexpansive and precise equipment (Yi <i>et al.</i>, 2007).</li> <li>2. Allow the large scale of nanostructures production at a relatively low cost (Yi <i>et al.</i>, 2007).</li> <li>3. The low temperature growth method makes it suitable for flexible polymers, and the arrays can be readily patterned using standard synthesis procedures (Yi <i>et al.</i>, 2007).</li> </ol>	<ol style="list-style-type: none"> <li>1. Two steps process, which co-operate with the hydrothermal process for the formation of ZnO nanorods (Yi <i>et al.</i>, 2007) .</li> </ol>

Electrodeposition method	<ol style="list-style-type: none"> <li>1. Simple, quick, economic, and able to control the crystallization of ZnO nanostructures (G.-R. Li <i>et al.</i>, 2007).</li> <li>2. Low temperature condition, low equipment cost, and precise control of nanostructures (Abd-Ellah <i>et al.</i>, 2013).</li> </ol>	
Chemical vapor deposition method (CVD)	<ol style="list-style-type: none"> <li>1. Uniform distribution over large areas (Dobkin &amp; Zuraw, 2003; Plummer &amp; Griffin, 2001; Smith, 1995; Wolf &amp; Tauber).</li> <li>2. No compositional gradients across substrate (Dobkin &amp; Zuraw, 2003; Plummer &amp; Griffin, 2001; Smith, 1995; Wolf &amp; Tauber).</li> <li>3. During the sources change, there is no need to stop the vacuum (Dobkin &amp; Zuraw, 2003; Plummer &amp; Griffin, 2001; Smith, 1995; Wolf &amp; Tauber).</li> <li>4. Due to the higher activation energy for reaction, it can be more selective in deposition (Dobkin &amp; Zuraw, 2003; Plummer &amp; Griffin, 2001; Smith, 1995; Wolf &amp; Tauber).</li> <li>5. MOCVD is suitable synthesized uniform ZnO nanorods in bulk quantities (K.-S. Kim &amp; Kim, 2003).</li> </ol>	<ol style="list-style-type: none"> <li>1. Mostly involve safety and contamination (Dobkin &amp; Zuraw, 2003; Plummer &amp; Griffin, 2001; Smith, 1995; Wolf &amp; Tauber).</li> <li>2. Metal organics are pyrophoric (ignite in contact with air) (Dobkin &amp; Zuraw, 2003; Plummer &amp; Griffin, 2001; Smith, 1995; Wolf &amp; Tauber).</li> <li>3. High cost for compounds with sufficient purity (Dobkin &amp; Zuraw, 2003; Plummer &amp; Griffin, 2001; Smith, 1995; Wolf &amp; Tauber).</li> <li>4. The combination of chemical reaction and gas kinetics; lead the CVD process more complicated (Dobkin &amp; Zuraw, 2003)</li> </ol>
Atomic layer deposition method (ALD)	<ol style="list-style-type: none"> <li>1. Low processing temperature (Demmin, 2001; Leskelä &amp; Ritala, 2002).</li> <li>2. Accurate and facile thickness control, excellent conformality, high uniformity over a large area, good reproducibility, dense and pinhole-free structures, and low deposition temperatures (M.-K. Wu <i>et al.</i>, 2010).</li> </ol>	<ol style="list-style-type: none"> <li>1. Low deposition rate (Demmin, 2001).</li> <li>2. The use of electropositive metals (alkaline earth metals, rare earth metals) form a challenge for chemical thin film depositions as they do not have many volatile compounds (Leskelä &amp; Ritala, 2002).</li> </ol>

## 2.4 Crystallization of ZnO nanostructures

The crystallization of ZnO nanostructures might affect the photocatalytic and PEC performance of ZnO nanostructures. Chen *et al.*, Goh *et al.*, Cheng *et al.*, and other researchers agreed that as-synthesized ZnO is in amorphous phase (Z. Chen *et al.*, 2010; C. Cheng *et al.*, 2007; Goh *et al.*, 2011; Hwang & Wu, 2004; Khrypunov *et al.*, 2011; S. J. Kim *et al.*, 2008; Mao *et al.*, 2002; Miller *et al.*, 2014; Musić *et al.*, 2003; Q. Sun *et al.*, 2012; S. Xu & Wang, 2011; J. H. Zeng *et al.*, 2009). In fact, heat treatment process might alter the properties (semiconducting property, photoconductivity, tunable electric property, thermal conductivity, piezoelectricity, and luminescent property) of ZnO and has direct relation with crystallization of ZnO nanostructures.

In year 2007, Callister; stated that heat treatment is a phenomena that work with atomic diffusion. Besides, heat treatment acts as a strain hardening remover. Also, strengthening effect could be eliminated by heat treatment process at elevated temperature where strain hardening and reduction in grain size happened. However, restoration would occur at elevated temperature by two different processes; recovery and recrystallization. Restoration affects the grain growth. Nevertheless, heat treatment process allows the recrystallization process to occur by modification. Other effect of heat treatment is coring; which at elevated temperature enables a homogenation to occur below the solidus point for certain alloy or composite. Compositionally, homogenous grains occurred due to atomic diffusion (Callister & Rethwisch, 2007).

Three factors that are very important during heat treatment process are applied temperature, heating time at applied temperature, and cooling rate to room temperature. Heat treatment is closely related with solid state transformation (kinetic consideration) and it affects nucleation, growth, and transformation rates. Kinetic of solid state

transformation is measured as a function of time while temperature is maintained constant  
Equation 2.8.

$$y = 1 - \exp(-kt^n) \quad \text{Equation 2.8}$$

where,

$y$  = fraction of transformation

$t$  = time

$k$  &  $n$  = time-independent constant for particular reaction.

Supercooling and superheating during heat treatment are the rate of temperature change. High supercooling and superheating will produce internal stress, and temperature gradients that could lead to warping and cracking of structure (Callister & Rethwisch, 2007). Temperature, heating rate, cooling rate, and heating time need an equilibrium conditions to achieve the best phase transformation.

Musić *et al.* reported that the use of precursors have an impact on the crystallization of ZnO as well as its properties. The decomposition of urea produced basic zinc carbonate. Further treatment of this basic zinc carbonate under temperature 300 °C will formed ZnO. Meanwhile, second method is hydrothermal technique. The use of  $Zn_5(OH)_8(NO_3)_3(H_2O)_{2-x}(NH_3)_x$  as a complex compound will undergo hydrothermal technique prior to ZnO formation (Musić *et al.*, 2003). Musić *et al.*, Chin *et al.*, and Molefe *et al.* also added that the crystallization increased with increased growing temperature; either in hydrothermal technique or chemical bath deposition as well as radio frequency (RF) sputtering (Chin & Chao, 2013; Molefe *et al.*, 2015; Musić *et al.*, 2003).

## 2.5 Modification of ZnO nanostructures

ZnO nanostructures are a rapidly developed metal oxide. The dynamic in design and most promising functional properties attracted momentous scientific interest. With its vast nano-architecture, ZnO nanorod shape is the most studied photocatalyst in PEC water splitting application. As mentioned earlier, its limitation especially its poor visible light absorption and rapid recombination charge carrier losses hinder further practice in electronic application. Thus, utilization of visible light from our solar energy and reduce the recombination losses of charge carriers are essential that lead to the higher photoconversion efficiency in water-splitting applications

### 2.5.1 Metal-coated ZnO nanostructures

Lately, many potential modification techniques for improvement of ZnO have been studied and reported actively around the world. The coupling of ZnO with various noble metals is one of the techniques. This technique helps on the prevention towards corrosion and oxidation under moist air (K. Huang *et al.*, 2014; H. Zeng, Cai, *et al.*, 2008; H. Zeng, Liu, *et al.*, 2008). Examples of noble metals are palladium, silver, osmium, iridium, platinum, and gold. Another technique involves the coupling of ZnO semiconductor with transition metal ions. Transition metal ions are the metals with incomplete d-orbitals; for instances Titanium, Nickel, Cobalt, Manganese, Ferum, Copper, Chromium, and Vanadium (K. Huang *et al.*, 2014; Ullah & Dutta, 2008; Yefeng Yang *et al.*, 2013). This coupling technique has been widely studied around the world.

The coupling of metal with ZnO works differently in Fermi levels. The performance is improved by the work function of the band structure of ZnO and metal (Kapałka *et al.*, 2010). The transfer of charge carriers are rectified in the coupled semiconductor (Gao *et al.*, 1991; Kapałka *et al.*, 2010; Linsebigler *et al.*, 1995; Schierbaum *et al.*, 1991). The electrons in the CB of semiconductor are generated by the photon irradiation and lead its

Fermi level to be more negative in value (Kapałka *et al.*, 2010; Subramanian *et al.*, 2004). At the semiconductor/metal interface, the energetic difference drives the electrons from semiconductor CB to metal nanoparticles; which lead the secondary electrons transfer occurs during redox couples from surrounding electrolyte (Kapałka *et al.*, 2010; Yu *et al.*, 2000).

### **2.5.2 Polyaniline-modified ZnO nanostructures**

Other coupling agent for the improvement of ZnO semiconductor performance is polyaniline (Tang *et al.*, 2012; H. Zhang *et al.*, 2009). Polyaniline (PANI) acts as a photocorrosion inhibitor and photocatalytic activity improver. Moreover, separation efficiency is high for photogenerated charge carriers on the hybrid PANI/ semiconductor interface. In the meantime, the inhibition of photocorrosion of ZnO can be done by photogenerated holes transferred rapidly by PANI monolayer. Nevertheless, PANI improved the ZnO performance under visible irradiation, when excited electron is delivered to CB of ZnO and electrons are transferred to adsorbed electron acceptor. Hydroxyl radical will be produced which can catalyzed pollutant degradation (H. Zhang *et al.*, 2009).

### **2.5.3 Carbon-modified ZnO nanostructures**

Outstanding performance of ZnO semiconductor could be achieved by graphite-like carbon doping or coupling (K. Huang *et al.*, 2014; L. Zhang *et al.*, 2009). Graphite-like carbon coupling ZnO helped in photocorrosion suppression by developing surface hybridization. These carbon materials inhibit the coalescence and crystal growth of ZnO at high temperature annealing. In addition, carbon materials improve the ability of adsorption, crystallinity, and increase the reusability of this hybrid graphite-like carbon/ ZnO for photocatalysis reaction. Other advantage of this idea is ZnO would perform

better under extreme pH condition (K. Huang *et al.*, 2014; Mishra *et al.*, 2013; Xinyu Zhang *et al.*, 2015).

#### **2.5.4 Semiconductor-modified ZnO nanostructures**

The coupling of ZnO semiconductor with other semiconductors could also improve its photocatalytic and PEC performance. In general, many researches proved that performance of ZnO (visible light absorption and recombination of charge carrier losses) could be improved by coupling with another semiconductor (Kim & Park, 2011; Navarro Yerga, Álvarez Galván, Del Valle, Villoria de la Mano, & Fierro, 2009). Many semiconductors could be coupled with ZnO such as Cadmium selenide (CdSe), Gallium arsenide (GaAs), Silicon carbide (SiC), Boron Arsenide (BAs), Cadmium sulfide (CdS), and other metal oxide semiconductors. Charge carriers recombination can be reduced by appropriate coupling of CB and VB of two different semiconductors. The reason is the charge carriers will be transferred from one semiconductor to another semiconductor, therefore; it prolonged the movement of charge carriers and prevent the recombination process to occur. Furthermore, the composite of semiconductors can be activated in the visible region depending on the band-gap energy of the semiconductor used (H. Zhang, Chen, & Bahnemann, 2009). The impurity level existed from the replacement of cationic ions within the crystal lattice facilitate better absorption in the visible region. The interfacial potential gradient corresponds to the energetic position, play a role as providing better charge carrier transportation and charge carrier separation can be achieved by modification of core semiconductor (Bessegato, Guaraldo, & Zanoni, 2014; Lai, Juan, Ko, & Bee Abd Hamid, 2014).

The mechanism of electrons movement in semiconductors composite will be discussed here on. When the semiconductors composite is illuminated by photon, electrons at more negative conduction band will be injected to the more positive band. At the same time,

holes the more positive valence band will be transferred to the more negative band. Therefore, the separation of charge carrier could be achieved and the lifetime of charge carriers could be increased. It will also contribute to significant increase of interfacial charge transfer to the water (Leung et al., 2010; Kim et al., 2011). It is important to realize that an optimum content of second oxide semiconductors will create an excellent performance by promoting an impurity level in binary type semiconductor. However, excess second semiconductor may lead to disadvantageous impurity level and poor result (Ghicov & Schmuki, 2009; Lai et al., 2014).

## **2.6 Hybrid TiO<sub>2</sub>-ZnO nanostructure film as photoelectrode**

PEC water splitting solar energy conversion efficiency and photocatalytic performance are dependent on the light adsorption capability, charge separation competency, the movement of charge migration, charge recombination process and electrocatalytic activity on the surface of photocatalyst (J. Li & Wu, 2015). The purpose of TiO<sub>2</sub>-ZnO hybridization is basically to increase the adsorption efficiency of solar irradiation and to overcome the PEC photoelectrode inhibition of recombination by building heterojunction. From the heterojunction, it would produce electrons sink. Furthermore, TiO<sub>2</sub> and ZnO are very good conductors; therefore, the quantum confinement effect would be generated from the nanostructures and lead to high electron mobility.

Therefore, the modification of binary oxide arises from the enrichment of second oxide on primary oxide would diminish radiation less transfer of the photon energy absorbed by second oxide (Anpo *et al.*, 1986). In another study, Anpo *et al.* have proved that the enhancement of the photocatalytic activity of the TiO<sub>2</sub> species in the primary oxide having a lower Ti content (Anpo *et al.*, 1986). Nakamura *et al.*, Ihara *et al.*, and Rehman

*et al.* stated that semiconductor coupling may create band-gap modification by introducing oxygen vacancies modification and oxygen sub-stoichiometry; and this modification help to improve the workability of semiconductor under visible light (Ihara *et al.*, 2003; Nakamura *et al.*, 2000; Rehman *et al.*, 2009). Grain boundaries of polycrystalline semiconductor are the place for oxygen vacancies to occur. A discrete state of about 0.75 eV and 1.18 eV can be generated under the CB of core semiconductor and the adsorption towards visible light can be improved (Nakamura *et al.*, 2000; Rehman *et al.*, 2009). A good property of oxygen vacancies is as electron trapper. Oxygen vacancies are an excellent electron trapper. Therefore, with the existence of oxygen vacancies lie close to the CB of core semiconductor help to increase in capturing electron and promote to visible light adsorption at semiconductor surface (Nakamura *et al.*, 2000; Rehman *et al.*, 2009). Justicia *et al.* claimed that oxygen sub-stoichiometry is generating an overlap of defect states and reduces catalyst band gap (Justicia *et al.*, 2005).

Jlassi *et al.* also found that coupling a photocatalyst with another semiconductor would promise a better photocatalytic activity. The comparison of TiO<sub>2</sub>-ZnO based film with pure P25 TiO<sub>2</sub> showed a better photocatalytic efficiency of TiO<sub>2</sub>-ZnO based film. This could be explained by efficient photocatalytic activity by improvement in the charge-carrier lifespan. Additionally, the efficient electron transfer from ZnO to TiO<sub>2</sub> increases the photocatalytic activity. The improvement of photocatalytic activity is due to the perturbation occurred on the surface of composite structure (Jlassi *et al.*, 2013).

Meanwhile, Tian *et al.* revealed hybrid TiO<sub>2</sub>-ZnO film crystallization behavior are influenced by atomic ratio of Ti. Sol-gel technique was chosen for the formation of hybrid TiO<sub>2</sub>-ZnO film by direct mixing of TiO<sub>2</sub> -ZnO and heat treatment for 2 hours at 500 °C (Tian *et al.*, 2009). Hernandez *et al.* studied ZnO-TiO<sub>2</sub> nanoarrays formation by using hydrothermal technique and TiO<sub>2</sub>-covered ZnO via non-acid sol-gel technique. The

impregnation method was varied from 3-10 min. From the PEC tests, the ZnO-TiO<sub>2</sub> materials exhibited photocurrent density of value 0.7 mA/cm<sup>2</sup> under solar light (AM 1.5G, 100mW/cm<sup>2</sup>) (Hernández *et al.*, 2014).

Dao *et al.* prepared TiO<sub>2</sub>-ZnO core shell via chemical synthesis. Basically, Dao's team used sol-gel technique for the TiO<sub>2</sub> formation and hydrothermal technique for the ZnO formation. The heterostructure produced an enhancement in light scattering and better charge carriers' separation. Moreover, under UV ray with reverse bias of -5 V application, 250 A/W and switch current ratio of 140 is produced (Dao *et al.*, 2013). Shao *et al.* has discovered high quality of ZnO-TiO<sub>2</sub> nanowires (NWs) could be fabricated via a facile-two steps method: hydrothermal technique for ZnO NWs and atomic layer deposition (ALD) technique for TiO<sub>2</sub> coating. Efficient charge carriers' separation of TiO<sub>2</sub>-ZnO has quenched the UV emission intensity which showed reduction in band-to-band recombination. On the contrary, the UV and visible light adsorption ability are improved due to the high refractive index of TiO<sub>2</sub>. A maximum value of 495 A/W at 373 nm photoresponsivity was detected; which is ~8 times higher compared to bare ZnO NWs. Meanwhile, the transient response is improved ~6 times compared to bare ZnO NWs (Shao *et al.*, 2014).

Cheng *et al.* discovered hybrid TiO<sub>2</sub>-ZnO film exhibited strong quenching of green emission under photoluminescence testing. This result attributed by the enhancement of charge carriers' separation resulting from type II heterojunction existed near TiO<sub>2</sub>-ZnO hybrid interface. Nevertheless, the catalytic activity improved due to the change in E<sub>g</sub> occurred, and the improved in high specific area, and surface hydroxyl groups (C. Cheng *et al.*, 2014). Summary of hybrid TiO<sub>2</sub>-ZnO formation based on different technique from past researchers is tabulated in Table 2.2. Optimum amount of incorporated TiO<sub>2</sub>-based ZnO formation extends the lifetimes of charge carriers and suppresses the recombination losses effectively. The modification of ZnO could lead to higher photocatalytic activity

and PEC performance than pure ZnO. Besides, the improvement in light absorption occurred from UV region to visible region.

University of Malaya

**Table 2.2: The previous studies of hybrid TiO<sub>2</sub>-ZnO formation based on different technique.**

Authors	Technique	Findings	Photoresponse performance	Reference
Dali Shao <i>et al.</i> (2014)	<ul style="list-style-type: none"> <li>▪ Hydrothermal (ZnO nanowires)</li> <li>▪ Atomic layer deposition (TiO<sub>2</sub> shell)</li> </ul>	<ul style="list-style-type: none"> <li>▪ Two steps Synthesis ZnO-TiO<sub>2</sub> core shell nanowires. For UV sensing application.</li> <li>▪ UV ray efficiently reduced band-to-band recombination.</li> </ul>	<ul style="list-style-type: none"> <li>▪ Maximum photoresponsivity with 495 A/W at 373 nm under -10V.</li> </ul>	(Shao <i>et al.</i> , 2014)
Simelys Hernández <i>et al.</i> (2014)	<ul style="list-style-type: none"> <li>▪ Seed layer-assisted hydrothermal route (ZnO nanowires)</li> <li>▪ In situ non-acid sol-gel synthesis (TiO<sub>2</sub> shell).</li> </ul>	<ul style="list-style-type: none"> <li>▪ The core-shell photo-anodes performance was about twice and forty- times better than the ones with a film of equivalent thickness of bare ZnO NWs and TiO NPs, respectively.</li> </ul>	<ul style="list-style-type: none"> <li>▪ Photocurrent densities, values of about 0.7 mA/cm<sup>2</sup> under simulated solar light (AM1.5G, 100mW/cm<sup>2</sup>).</li> </ul>	(Hernández <i>et al.</i> , 2014)
Dao <i>et al.</i> (2013)	<ul style="list-style-type: none"> <li>▪ Hydrothermal (ZnO nanowires)</li> <li>▪ Sol-gel (TiO<sub>2</sub> shell)</li> </ul>	<ul style="list-style-type: none"> <li>▪ UV photodetector</li> <li>▪ Heterojunction is composed of a 5–10 nm thick p-type Cr-doped TiO<sub>2</sub>nanoshell and n-type single-crystalline ZnO nanowires (50 nm radius).</li> </ul>	<ul style="list-style-type: none"> <li>▪ At a moderate reverse bias of -5 V and under UV ray at 104 μW, it showed a switch current ratio of 140 μW and a responsivity as large as 250 A/W, while it showed nearly no response to the infrared and visible light.</li> </ul>	(Dao <i>et al.</i> , 2013)
Lin Lin <i>et al.</i> (2012)	<ul style="list-style-type: none"> <li>▪ Hydrothermal technique</li> </ul>	<ul style="list-style-type: none"> <li>▪ TiO<sub>2</sub>- ZnO n-p-n heterojunction nanorod with diameter of 30 nm.</li> <li>▪ Photodegrading methyl orange has been demonstrated to increase three</li> </ul>	<ul style="list-style-type: none"> <li>▪ <i>Nil</i></li> </ul>	(L. Lin <i>et al.</i> , 2013)

		times compared to that of wurtzite hexagonal ZnO.		
Shrabani Panigrahi <i>et al.</i> (2011)	<ul style="list-style-type: none"> <li>▪ Aqueous chemical technique (ZnO nanorod)</li> <li>▪ Solution of titanium isopropoxide [Ti(OC<sub>3</sub>H<sub>7</sub>)<sub>4</sub>] followed by a heating to form the shell (TiO<sub>2</sub> shell)</li> </ul>	<ul style="list-style-type: none"> <li>▪ UV sensor application.</li> </ul>	<ul style="list-style-type: none"> <li>▪ The UV photosensitivity of the nanocomposite becomes four times larger while the photocurrent decay during steady UV ray has been decreased almost by 7 times compared to the as-grown ZnO NRs indicating high efficiency of these core-shell structures.</li> </ul>	(Panigrahi & Basak, 2011)

University of Malaya

### CHAPTER 3: METHODOLOGY

The use of nanoscale materials results in their tunability, which has a number of benefits. Therefore, staged research was conducted in order to produce hybrid TiO<sub>2</sub>-ZnO nanostructure for PEC water splitting. This chapter covers the explanation and discussion of six important sections. In section one, the general information on the raw materials and chemicals used in this study is provided. In section two, the experimental procedure for synthesising ZnO nanostructures film by optimizing several important electrodeposition conditions, e.g. temperature, exposure time, applied potential and heat treatment temperature are explained and elaborated in detail. The next section emphasizes on the influence of temperature and stirring speed toward TiO<sub>2</sub> nanoparticles via precipitation and peptization techniques. Then, in the fourth section, the parameters tested for the synthesized TiO<sub>2</sub>-ZnO nanostructures film will be discussed, namely exposure time and number of cycle during dip-coating technique. These studies aim to determine the optimum processing parameters to obtain desired hybrid TiO<sub>2</sub>-ZnO nanostructure film for PEC water splitting. The following section outlines the characterization of structural, morphological, optical, electronic and electrochemical properties of the ZnO, TiO<sub>2</sub>, and hybrid TiO<sub>2</sub>-ZnO nanostructure film samples using various techniques, such as Field emission scanning electron microscopy (FESEM), High resolution transmission electron microscopy (HRTEM), X-ray diffraction (XRD), Raman spectroscopy, Photoluminescence spectroscopy (PL), and UV-Vis diffuse reflectance spectroscopy (UV-DR). The last section in this chapter describes the PEC water splitting system by conducting three-electrode PEC system. Figure 3.1 shows the overview of research methodology.

### **3.1 Raw materials**

In the present study, raw materials and chemicals selection became one of the most important factors in designing and developing nanostructure of ZnO film for better PEC water splitting performance. Table 3.1 shows the general information of raw materials and chemicals used in this research work.

University of Malaya

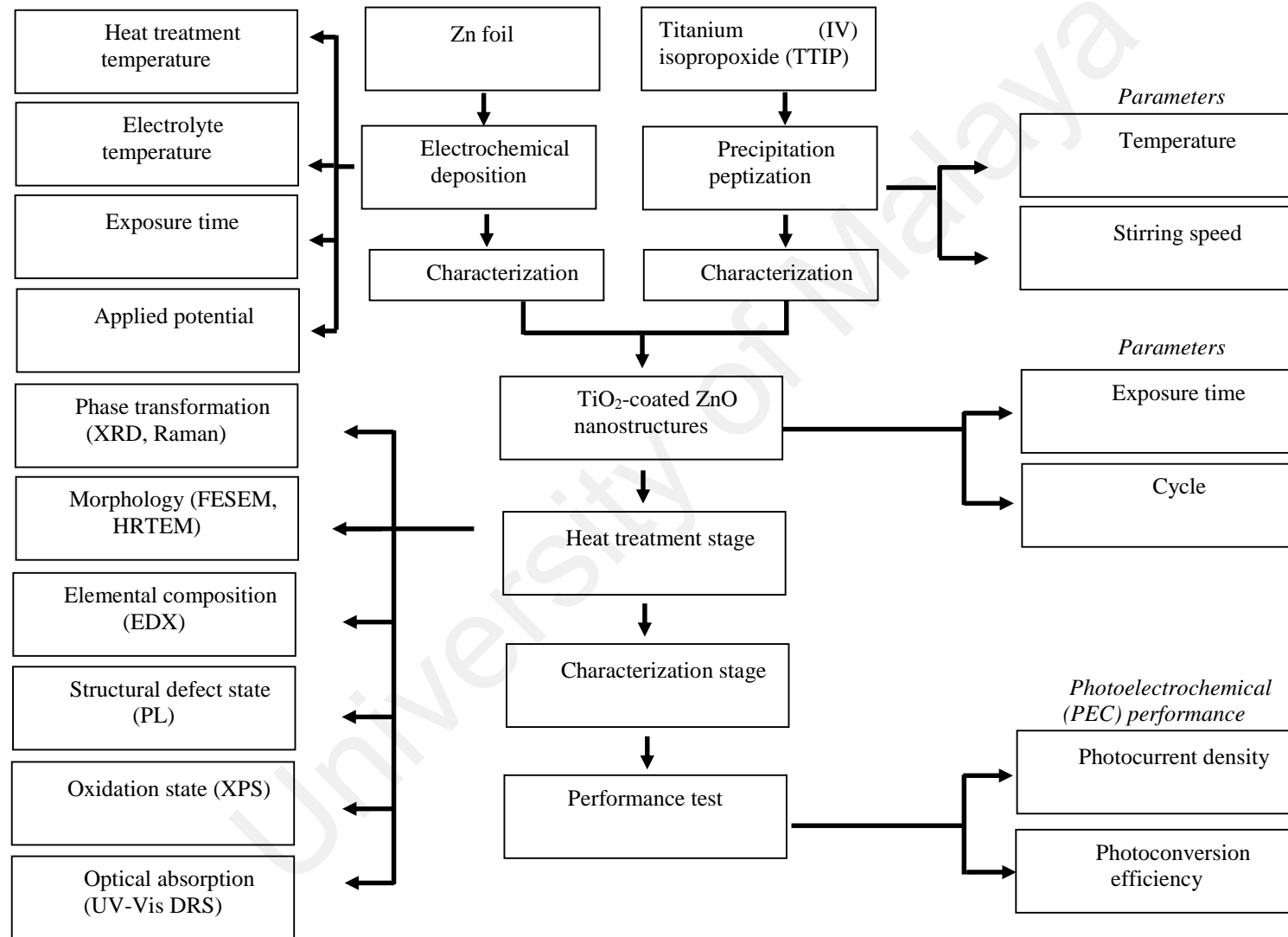


**Figure 3.1: The overview of research methodology**

**Table 3.1: Raw materials and chemicals used for the preparation of TiO<sub>2</sub>-ZnO nanostructures and PEC performance evaluation.**

Materials (chemical formula)	Function	Manufacturer /country	Properties
Zn foil	Substrate	Sigma Aldrich / United States	Purity: 99.9% Thickness : 0.25mm
Zinc chloride	Electrolyte	Merck / Unites States	Chemical formula : ZnCl <sub>2</sub> Purity : 98.0%
Potassium chloride	Directing agent	Merck / Unites States	Chemical formula : ZnCl <sub>2</sub> Purity : 98.0%
Acetone	Cleaning agent	Merck / Unites States	Chemical formula : ZnCl <sub>2</sub> Purity : 98.0%
Titanium (IV) isopropoxide	Precursor	Sigma Aldrich / United States	Chemical formula: Ti[OCH(CH <sub>3</sub> ) <sub>2</sub> ] <sub>4</sub>
2-propanol	Solvent	Merck / Unites States	Chemical formula : ZnCl <sub>2</sub> Purity : 98.0%
Ethanol	Cleaning agent	J. Kolin / United States	Chemical formula: C <sub>2</sub> H <sub>6</sub> O Purity: 95%
Nitric acid	pH controller	Merck / Unites States	Chemical formula : HNO <sub>3</sub> Purity : 98.0%
Sodium hydroxide	PEC electrolyte	Merck / Unites States	Chemical formula: NaOH Purity : 98.0%
Ethylene glycol	Sacrificial agent	Friedemann Schmidt / Germany	Chemcial formula: C <sub>2</sub> H <sub>6</sub> O <sub>2</sub>

## 3.2 Synthesis of ZnO nanostructures film

### 3.2.1 Foil preparation

The cleanliness of the substrate is crucial as it affects the epitaxial growth oxide layer. The columnar crystals grow and misalign with each other if the substrate is not molecularly smooth (Atwood & Zuckerman, 1999). This affects the grains and performance of the photoelectrode following the heat treatment process. In addition, the dehydration rate and deposition rate are critically dependent on substrate condition (Machlin, 2006). Zn foil that had been cut into the desired dimensions (5 cm x 1 cm) was immersed in acetone and then cleaned in an ultrasonic bath for 30 min. Then, the Zn foil was rinsed with deionized (DI) water and air-dried (less than 1.0 sec.).

### 3.2.2 Electrolyte preparation

The quality of the thin film is directly related to the electrolyte used. The electrolytes selected should provide the following characteristics to support the formation of good quality thin film: (1) Ionic transport, (2) Discharge, (3) Breaking of ion-ligand bond (sometimes this characteristic could be negligible if not relevant), and (4) Atoms incorporated on the substrate surface (nucleation and growth) (Das & Jayaraman, 2014). Moreover, the electrolyte should provide (1) a sufficient current density, (2) sufficient metal ions, and (3) a hydrogen ion concentration (pH). The electrolyte used in this study was 0.5 mM zinc chloride with  $ZnCl_2$  as the main electrolyte and 0.1 M potassium chloride, KCl, as the directing agent. The mixture was stirred using magnetic agitation for 30 min prior to the electrodeposition procedure.

### 3.2.3 Electrodeposition procedure

In this procedure, the platinum rod acted as the anode through a connection to the positive terminal of a DC power supply. Meanwhile, Zn foil acted as the cathode through a connection to the negative terminal of the DC power supply. The DC power supply was adjusted to the desired potential and then switched on. Once the desired exposure time was reached, the electrodeposition process was stopped by switching off the DC power supply. Throughout the electrodeposition process, the electrolyte was magnetically agitated using a very slow speed. Minimum of two replicates has prepared for each ZnO nanostructures film sample. The schematic diagram of electrochemical process as in Figure 3.2.

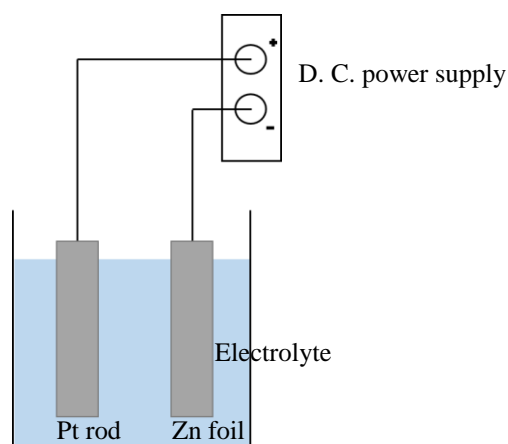


**Figure 3.2: Schematic diagram of electrodeposition process for synthesizing ZnO film.**

### 3.2.4 Cleaning ZnO nanostructures

This process is crucial because the future analytical process could be affected if the thin film contains debris or any leftover precipitation layer. Therefore, acetone was used as a cleaning agent. The thin film was agitated in an acetone solution for 20 seconds and allowed to air-dry.

## 3.3 Synthesis of TiO<sub>2</sub> nanoparticles

### 3.3.1 Acidified water preparation

The main purpose of the acidified water was to hydrolyze the titanium (IV) isopropoxide (TTIP), creating TiO<sub>2</sub> nanoparticles. Also, acidified water meant to reduce the tendency of TiO<sub>2</sub> nanoparticle agglomeration because nanoparticles with high surface area tend to agglomerate more than sub-micro particles. Also, the existence of Van der Waals forces between nanoparticles attract the particles to each other. Therefore, using acidified water, electrostatic stabilization could be achieved by introducing an additional charge, meaning that the particles repelled each other. (Othman *et al.*, 2012). The pH of acidified water was pH 3. Approximately 5 ml of 0.5 M nitric acid was added to 208.3

ml DI water together with 41.7 ml 2-propanol prior to the precipitation peptization process.

### **3.3.2 Dilution of Titanium (IV) isopropoxide (TTIP)**

The characteristic of TTIP that led to this step was that it is easily or rapidly hydrolysed upon contact with humid air. Therefore, the dilution of TTIP with 2-propanol was to prevent agglomeration prior to the precipitation and peptization procedures (Bhandarkar *et al.*, 2000). In addition, 2-propanol was used to prevent an irregular shaping of the TiO<sub>2</sub> nanoparticles due to the rapid hydrolysis (Termnak *et al.*, 2009). The ratio of Ti to 2-propanol was ~ 1:5.

### **3.3.3 Precipitation and peptization procedure**

Using standard procedure, dissolved titanium (IV) isopropoxide (TTIP) was added quickly and under vigorous stirring into an acidified water. A white precipitate was obtained. During the titration process of TTIP into acidified water, the reaction flask was kept uncovered in order to allow the isopropyl alcohol to evaporate. At the end of the peptization, the pH of the sol was about 1.4 and the molar concentration of Ti was in the range of 0.6–0.65 M (Alphonse *et al.*, 2010). Figure 3.3 shows the schematic diagram of experimental set up for synthesizing TiO<sub>2</sub> nanoparticles.

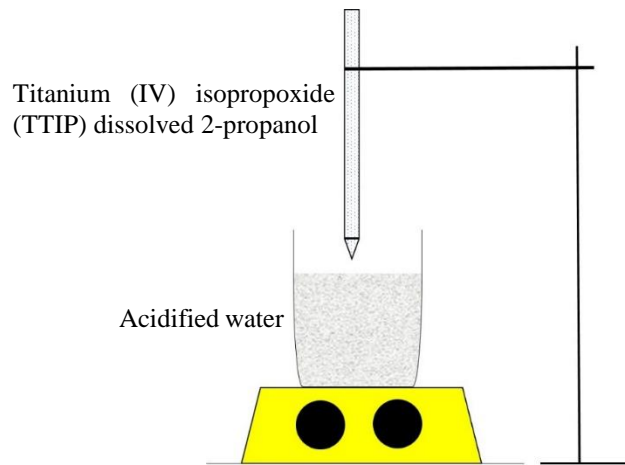


**Figure 3.3: Schematic diagram of experimental set up for synthesizing of TiO<sub>2</sub> nanoparticles.**

### 3.3.4 Washing TiO<sub>2</sub> nanoparticles precursor

The cleaning process of the TiO<sub>2</sub> sols was made by centrifuging the solution at 7500 rpm for 5 min. Then, the water residue was carefully discarded. After that, the solution was stirred with ethanol and centrifuged again. This process was repeated five times.

## 3.4 Synthesis of hybrid TiO<sub>2</sub>-ZnO film

In this study, the formation of the hybrid TiO<sub>2</sub>-ZnO film was done via dip-coating technique. The first step was the immersion of a ZnO nanostructure into the TiO<sub>2</sub> solution (jitter-free). ZnO nanostructure has been chosen because it has the excellent performance compared to other ZnO nanostructures. The ZnO nanostructure remained in the TiO<sub>2</sub> solution for less than five seconds and the deposition of a very thin layer of TiO<sub>2</sub> occurred. The drainage and evaporation of the excess TiO<sub>2</sub> solution was done by drying the dipped thin film in an oven at 60 °C and anneal it at 400 °C.

### 3.4.1 Annealing process

Materials are often heat treated to enhance their properties. The diffusion phenomenon within material transport involves atomic movement. This phenomenon transfers

materials from the amorphous state to the crystalline state. The heat treatment process involves heat treating temperature, time, heating rate, and cooling rate. Heat treated hybrid TiO<sub>2</sub>-ZnO nanostructure demonstrates better PEC properties. The three stages of the annealing process are the heating, soaking, and cooling processes. The heating rate used in this experiment was 3 °C/min until it reached 400 °C. It dwelled at this temperature for three hours and cooled slowly in the furnace. The very slow heating rate was used with the intention of allowing the diffusion of atoms within the materials. From the previous researches, 400°C is sufficient to achieve excellent structural and optical properties for ZnO and TiO<sub>2</sub>. In addition, 400°C is the minimum temperature to inhibit defect-related recombination (Hang *et al.*, 2014; Sanjeev & Kekuda, 2015) The atmosphere used was air during heat treatment process. Figure 3.4 shows the annealing profile for this research work.

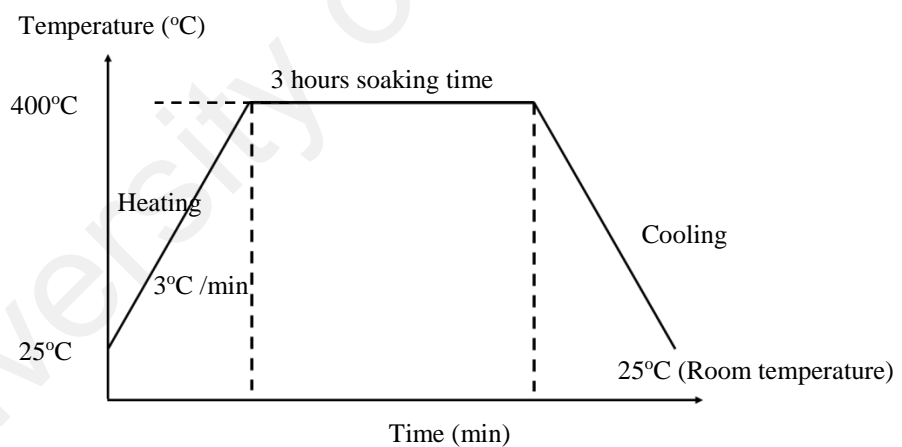


**Figure 3.4: Annealing profile**

### **3.5 Characterization Techniques**

#### **3.5.1 Field emission scanning electron microscopy (FESEM)**

Field emission scanning electron microscope (FESEM) is a microscope that works with the electron principle. FESEM helps researchers to study the very small topography of a surface or fractioned objects. In addition, FESEM allows the observation of a

structure at the nanoscale. Normally, electrons are liberated from the emission source and are accelerated by a high electric field gradient. These electrons are very focused due to the high vacuum column. The use of electronic lenses produces a narrow scan beam which bombards the materials. As a result, secondary electrons are emitted from each spot. The angles and velocity of the secondary electrons produce an image of the surface. FESEM images have great depth of field and a three-dimensional (3D) appearance. The FESEM used in this research was JEOL JSM-7600F operated at 5.0 kV at x10 000, x50 000, and x100 000 magnification.

Moreover, the FESEM was equipped with an Energy Dispersive X-ray (EDX) spectrometer. The EDX uses the X-ray spectrum emitting from a solid sample bombarded with focused beam electrons in order to obtain a localized chemical analysis. The EDX has two types of analysis. The qualitative analysis involves the identification of an element. Meanwhile, the quantitative analysis determines the elements' concentration. The electron probe is not only designed for producing electron images but also for mapping and point analysis. For ZnO characterization, 45° FESEM stand was used in order to measure accurate length of nanostructures. A replicates of 50 measurements have been done for each samples for FESEM and EDX respectively. Standard deviation has been calculated in order to find the closeness of measurement distribution has spread out from average (mean).

### **3.5.2 High resolution transmission electron microscopy (HRTEM)**

The difference between the high resolution transmission electron microscope (HRTEM) and other microscopes lies in its passing through and interacting with the atoms of the materials. The principal setup of the HRTEM is similar to that of a light microscope. In the case of the HRTEM, the materials are illuminated by electrons. The

image is then magnified by projection lenses and represented on a screen. The HRTEM allows the sample to be observed at an atomic resolution. The local atomic information includes precipitates, dislocations and grain boundaries. In addition, the HRTEM provides an observation of the lattice distortions due to dislocations, grain boundary defects, and dopant interstitials. The lattice fringes are observable in the thin sample. In this research work, the HRTEM used was a JEOL JEMP – 2100F. The magnification used was; x4 000, x12 000, x60 000, x100 000, and x800 000.

### 3.5.3 X-ray diffraction (XRD)

Electromagnetic radiation impinging on materials produces diffraction effects. When the x-ray is exposed to crystalline materials, it produces constructive and destructive interference phenomena. In the energy range, it produces three different interactions: (1) The bound atomic states liberate the electrons in the photoionization process; (2) Compton scattering is inelastic scattering that incoming x-ray beams may undergo; (3) Thompson scattering is scattered elastically by electrons (Birkholz, 2006). However, the very basic principal is based on the monochromatic x-ray beam that is directed at the crystalline materials. Then, the reflections are recorded using a detector at different angles which are respective to the primary beam. Using Bragg's Law:  $n\lambda = 2d\sin\theta$ , the  $d$ -spacing can be calculated. The  $d$ -spacing is a unique fingerprint of materials. In this research work, a Bruker D8 Advance equipped with EVA-Diffract Software (Germany) X-ray Dispersive (XRD) was used to analyse the crystallinity and phase transition of the TiO<sub>2</sub>-ZnO nanostructures. The XRD was conducted using 10-80 with Cu K $\alpha$  radiation ( $\alpha = 1.5406 \text{ \AA}$ ).

From XRD characterization, the crystallite size can be obtained by using Scherer's formula and phase quantification can be obtained by using Quantitative Analysis or Rietveld XRD Quantification formula. In addition, Direct Comparison Method and

relative intensity ratio (which is much easier than Rietveld XRD quantification) can be used in order to obtain the phase quantification (Hurst *et al.*, 1997; Kniess *et al.*, 2012). But, for this research work, relative intensity ratio was used and supported by calculation from XRD software (X'Pert HighScore Plus).

#### **3.5.4 Raman spectroscopy**

Raman spectroscopy technique is both a qualitative and a quantitative analysis. The qualitative involves the scattered radiation frequency, while the quantitative involves the scattered radiation intensity (Bumrah & Sharma, 2015; Skoog & West, 1980; Willard *et al.*, 1988). It is a non-destructive and non-contact test method. Raman spectroscopy technique can identify the chemical composition and structure of materials, even though these are in the same atomic but different arrangements. Vibrational, rotational, and low frequency modes can be observed and phase identification can be performed (Turrell *et al.*, 1989). The basic principle of Raman is that when the laser light interacts with a phonon, vibration or any other kind of excitation it produces the energy for a photon to shift up or down. When the material is illuminated by a laser beam, the electromagnetic radiation is collected and sent to a monochromator. The Rayleigh scattering is filtered out and the remaining light goes to a detector. In this research work, Raman spectroscopy was performed using a Renishaw in via Raman microscope. The laser light used was 514 nm and 325 nm over a range of  $100\text{ cm}^{-1}$  to  $1000\text{ cm}^{-1}$ .

#### **3.5.5 Photoluminescence spectroscopy (PL)**

Photoluminescence (PL) spectroscopy is a method of identifying the recombination mechanism and electronic structure, finding energy levels and crystal defects, e.g. the atomic interstitial, substitution or vacancies, and detecting the internal stress of materials. The basic principle behind PL spectroscopy is that the PL originates from the absorption

or emission process between different energy levels. A material absorbs photons and the electrons are excited to a higher energy state and then the photons are emitted and the electrons return to the lowest energy state. In crystalline semiconductors, the band gap energy is an energy transition between electronic states and the decrease in the energy state is known as recombination. In this research, the PL spectroscopy identified recombination using a monochromatic beam with 325 nm and in the range of 300 – 800 nm.

### 3.5.6 UV-Vis diffuse reflectance spectroscopy (UV-DR)

An energy band gap lies between the band structures, the valence band and the conduction band. Measuring the band gap is very important for semiconductor materials and nanomaterials. UV absorption and the reflectance spectrum determine the band gap energy. A diffuse reflectance measurement was used to characterize the opaque sample. The Kubelka-Munk function (K-M) and a Tauc plot were used to measure the band gap energy. In the K-M, a few assumptions were made. Materials were assumed to be: (1) uniform, (2) isotropic, (3) non-fluorescent, and (4) non-glossy; The K-M function is described below [Equation 3.1]. In particular, the energy band gap (eV) was obtained by extrapolating plots towards the  $h\nu$  (Tauc plot) [Equation 3.2]. The sample reflectance data were obtained using UV-DR Spectrophotometer Model UV – 3101PC Shimadzu.

$$[F(R) \cdot h\nu]^{1/2} = K (h\nu - E_g) \quad \text{Equation 3.1}$$

where;

$R$  = absolute reflectance of the sample layer

$h\nu$  = photons energy

$K$  = a constant characteristic of the semiconductor material

$E_g$  = band gap energy

and,

$$h\nu = hc / \lambda$$

**Equation 3.2**

where;

$h$  = Planks constant ( $6.626 \times 10^{-34}$  Joules or  $4.136 \times 10^{-15}$  eVs)

$C$  = Light speed ( $3.0 \times 10^8$  ms<sup>-1</sup> or  $3.0 \times 10^{17}$  ns<sup>-1</sup>)

$\lambda$  = cut-off wavelengths (nm)

### 3.5.7 X-ray photoelectron spectroscopy (XPS)

The basic principle of x-ray photoelectron spectroscopy (XPS) is the kinetic energy and number of electrons measured after the irradiation of an X-ray beam onto materials. XPS uses the surface-sensitive quantitative technique to measure the elemental composition (parts per thousand range), empirical formula, chemical state or electronic state, elements that contaminate the surface, the uniformity of elemental composition across the top of the sample (line profiling or mapping), and the uniformity of elemental composition (depth profiling). In this research, a PHI Quantera II scanning X-ray microprobe using an Al cathode ( $h\nu = 1486.8$  eV) with a 100-micron spot size and a 280 eV pass energy was used. The core level spectra were recorded through high resolution narrow scans.

### 3.6 Photoelectrochemical (PEC) water splitting performance

Metrohm Autolab PGSTAT204 and PGSTAT302N potentiostat were used to study the photoelectrochemical (PEC) performance. The analysis included a photocurrent density analysis, and a photoconversion efficiency analysis. A three-electrode PEC system with hybrid TiO<sub>2</sub>-ZnO nanostructure films as the anode, a platinum rod as the cathode and an Ag/AgCl in saturated KCl electrode as the reference electrode were used in a quartz cell filled with 1M sodium hydroxide (NaOH) containing 1v% of ethylene glycol [Figure 2.1]. A Newport model 74010 light source was focused on the immersed

portion of the photoelectrode to simulate both UV and visible light. All of the three electrodes were connected to the potentiostat and an applied potential of -1 to 1V was used. The size of working electrode that was immersed in 1M sodium hydroxide (NaOH) was 3 cm x 1 cm.

### 3.6.1 Photocurrent density analysis

Current density was measured using a linear sweep voltammetry technique in which the current of a working electrode against potential (against a reference electrode) is swept linearly in time. The photocurrent density ( $j_{sc}$ ) could be recognized at a zero bias or short-circuit photocurrent.

### 3.6.2 Photoconversion efficiency analysis

Photoconversion efficiency ( $\eta$ ) was used to study the conversion of light energy to chemical energy. Several terms have been used to describe photoconversion efficiency, including Applied Bias Photon-to-Current Efficiency (ABPE), and Quantum Efficiency (QE). However, ABPE is normally used to present the photo-response efficiency of a photoelectrode under applied potential (Liao *et al.*, 2012). The equation related to photoconversion efficiency as in Equation 3.3.

$$\eta (\%) = \frac{\text{total power output} - \text{electrical power output}}{\text{light power input}} \times 100 \% \quad \text{Equation 3.3}$$

$$= j_p \frac{E_{rev}^0 - |E_{app}|}{I_0} \times 100 \%$$

where:

$j_p$  = photocurrent density in mA cm<sup>-2</sup>

$E_{rev}^0$  = reversible potential for water splitting (1.23 V SHE)

$E_{app}$  =  $E_{meas} - E_{counter}$

where:

$E_{meas}$  = electrical potential (V vs Ag/AgCl in saturated KCl electrode) of the working electrode under illumination

$E_{counter}$  = electrical electrode (V vs Ag/AgCl in saturated KCl electrode) of the working electrode at open circuit conditions.

### 3.6.3 Mott – Schottky Analysis

Another method of TiO<sub>2</sub>-ZnO photoelectrode characterization is Mott-Schottky plot. The photoelectrode/electrolyte interface electrochemical reaction determines the PEC efficiency of TiO<sub>2</sub>-ZnO photoelectrode. The investigation via Mott-Schottky (MS) showed the relationship of capacitance ( $C$ ) that was converted from real impedance ( $Z''$ ). Below are Mott-Schottky equation (Equation 3.4).

$$C = \frac{1}{2\pi f Z''}$$

**Equation 3.4**

where;

$f$  = applied frequency during measurement of 100000 Hz

$Z''$  = real impedance

## CHAPTER 4: RESULTS AND DISCUSSION

This chapter presents the results obtained from the experiments conducted and the discussion of the analyses on the formation of hybrid TiO<sub>2</sub>-ZnO nanostructures films. The ZnO were synthesized via electrodeposition method. Meanwhile, the TiO<sub>2</sub> nanoparticles were synthesized via precipitation-peptization method. The TiO<sub>2</sub>-ZnO was produced via dip-coating technique. There are three main sections in this chapter. The first section presents the information regarding to the growth mechanism and kinetic studies on the formation of ZnO nanostructures via the electrodeposition technique. The effect of temperature, exposure time, applied potential and heat treatment process on resultant ZnO nanostructures is evaluated in detail. The second section of this chapter will illustrate the formation of nano-size TiO<sub>2</sub> particles via precipitation-peptization technique by controlling temperature and stirring processing parameters. The last section discusses the incorporation of TiO<sub>2</sub> nanoparticles on ZnO nanostructure film using dip-coating technique. Two main processing parameters will be optimized throughout the experimental works, including exposure time and cycles. The PEC water splitting performance of the resultant hybrid TiO<sub>2</sub>-ZnO nanostructures film in term of photocurrent density and photoconversion efficiency are presented.

### 4.1 Easy formation of highly responsive ZnO nanostructures

In the present study, electrodeposition technique appears as a potential technique for depositing a thin layer of ZnO nanostructure onto a substrate (Zn foil). Furthermore, electrodeposition promises a uniform morphology of ZnO nanostructure layer across the substrate. This section presents a detailed investigation into the formation of ZnO nanostructures on substrates under different parameters, such as heat treatment for crystallization aspect, stirring rate effect, electrolyte temperatures, exposure time, and

applied potential. The influence of physicochemical characteristics on the PEC properties under UV-vis irradiation are studied in detail in following sections.

#### **4.1.1 The effect of heat treatment to crystallization aspect**

In this section, 0.5 mM ZnCl<sub>2</sub> electrolyte containing 0.1 M KCl, stirring rate (very slow agitation), electrolyte temperature of 80°C, exposure time of 60 mins, and applied potential of 3 V were constant for all samples. The as-prepared ZnO nanostructure film was amorphous in nature (Bruncko *et al.*, 2011). Thus, this part of experimental work presents the strongly beneficial effect of the heat treatment process for ZnO nanostructure film in improving the crystallinity and PEC water splitting performance than that of the as-prepared ZnO nanostructure film. In essence, high crystallinity ZnO nanostructure thin film is a more prominent aspect in improving its photocatalytic and PEC response (H.-C. Wang *et al.*, 2013). In this case, the annealed ZnO nanostructure film provided a better PEC performance with the transformation of the amorphous phase into the crystalline phase. This resultant condition could be categorized as wurtzite-type ZnO after annealing at 400 °C. Many literatures concluded that annealed ZnO nanostructure film played a crucial role in determining the photocurrent density response as compared to the as-prepared ZnO nanostructure film. Indeed, heat treatment process has significant effects on the morphological of ZnO nanostructure as well as hydrogen production studies. From the previous researches, 600°C- 1000°C have exhibited optical properties improvement. Moreover, improvement in green band emission also has been recorded at higher temperature (600°C- 1000°C) (Cai *et al.*, 2002; J. L. Y. C. J. Du & Lai). But, the investigation of the heat treatment effect on ZnO crystallization has stopped at 800°C because ZnO thin film has started to deform or totally melted at 900°C and above.

#### 4.1.1.1 Morphological studies and elemental analysis by FESEM-EDX and HRTEM

Since morphology is one of the main factors of a good photoelectrode, the insight gained from these morphological studies can be exploited to further improve our PEC water splitting system. In order to understand the effect of heat treatment on the morphology and phase transition of ZnO, the samples were annealed from 200 °C to 800 °C. Figure 4.1 exhibits the FESEM images of the as-prepared ZnO nanostructure film and annealed ZnO nanostructure film at 400 °C. The ZnO nanostructure film was successfully synthesized in 0.5 mM ZnCl<sub>2</sub> electrolyte with 0.1 M KCl. This composition was selected because it favours the formation of well-aligned ZnO nanostructure. As can be seen in the Figure 4.1, the ZnO nanostructure film were randomly nucleated and oriented. Figure 4.1 (a) shows a ZnO nanostructure before the heat treatment procedure; it was independently grown and lies poorly aligned in the *c*-axis direction. After heat treatment at 400 °C, it seems to be attached to the neighbouring rod [Figure 4.1 (b)]. This morphology was obtained due to the arrangement and movement of the Zn and O atoms during the heat treatment. Additionally, the thin film surface showed numerous micro-pores and some cracks due to the recombination of atoms, while the grain size became denser [Figure 4.2]. This finding is ascribed to the fact that the ZnO thin film lattice stress was released by increasing the particle size and producing more micro-pores or cracks in order to avoid falling off the Zn substrate at high annealing temperatures ( $> 500$  °C); because anisotropy-based nanostructured intergranular strains, produced excessive plastic deformation (lattice hardening to lattice softening) at high temperature (Fang *et al.*, 2014; Stoica *et al.*, 2014). But, with sufficient thermal supplied during heat treatment process, the atoms have enough diffusion activation energy to reside in the correct sites in the crystal lattice [Figure 4.2], and the grains with a lower surface energy become larger (Khojier *et al.*, 2014). Lattice fringes in Figure 4.2 showed good arrangement of ZnO

atoms after the heat treatment process. Under these circumstances, the heat treatment process decreases the defects in the crystal's performance. Thus, we can say that the heat-treatment process also assists with and influences the oxidation process for the formation of ZnO nanostructures and that the results are consistent with the EDX and XRD results [Table 4.1 and Figure 4.3].

The energy dispersive X-ray analysis (EDX) was employed to investigate the chemical stoichiometry of the as-prepared ZnO nanostructure film before and after the heat treatment stage. The typical EDX results, for an average compositional ratio of as-prepared ZnO nanostructure film at a 200 °C, 300 °C, 400 °C, 500 °C, 600 °C, 700 °C, and 800 °C annealing temperature, are shown in Table 4.1 respectively. It can be concluded that the annealing temperatures (200 °C-400 °C) show that the atomic ratio of Zn to O was approximately 1:1, and a further increase in the annealing temperature resulted in a higher ratio of oxygen. Strong solid-state reaction occurred at higher annealing temperature (recrystallization occurred) and it absorbed excess oxygen from ambient to oxidized ZnO nanostructures film (He *et al.*, 2005; Sendi & Mahmud, 2013). In addition, a higher Zn content (~ 84.32 at%) was obtained by the EDX analysis, indicating that the Zn species becomes prominent prior to conduct the heat treatment process. The reason was the oxygen atoms were not fully arranged and therefore, the ZnO crystal structure needs the heat treatment procedure to achieve a better nanostructure alignment and PEC performance. However, all samples showed the presence of only Zn and O elements without any impurities based on EDX analyses. Therefore, it could be concluded that the heat-treatment process plays an important role in controlling the oxidation process and crystallization control for the formation of the ZnO nanostructure film and to achieve excellent PEC performance (Sendi & Mahmud, 2013)

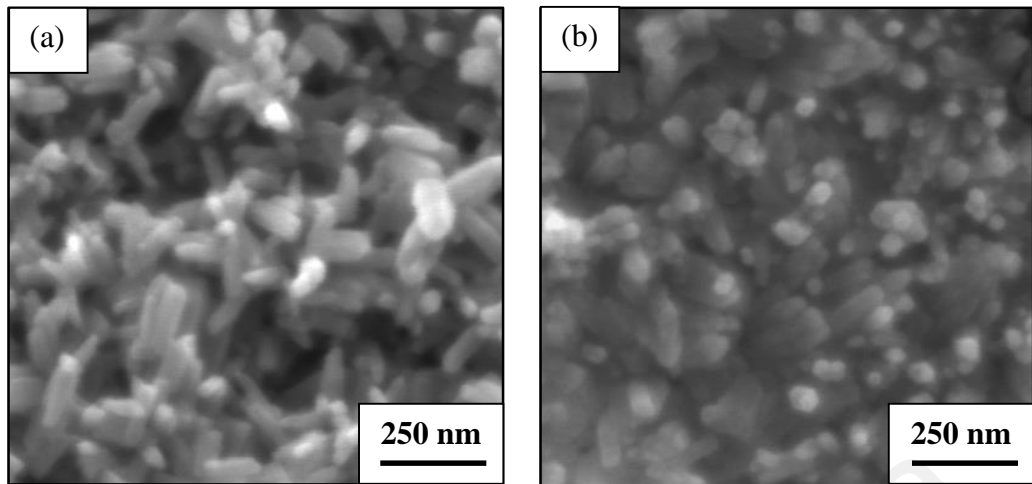


**Figure 4.1: FESEM images of (a) x100k magnification of ZnO nanostructure before heat treatment; and (b) x100k magnification of ZnO nanostructure; after heat treatment (400°C).**

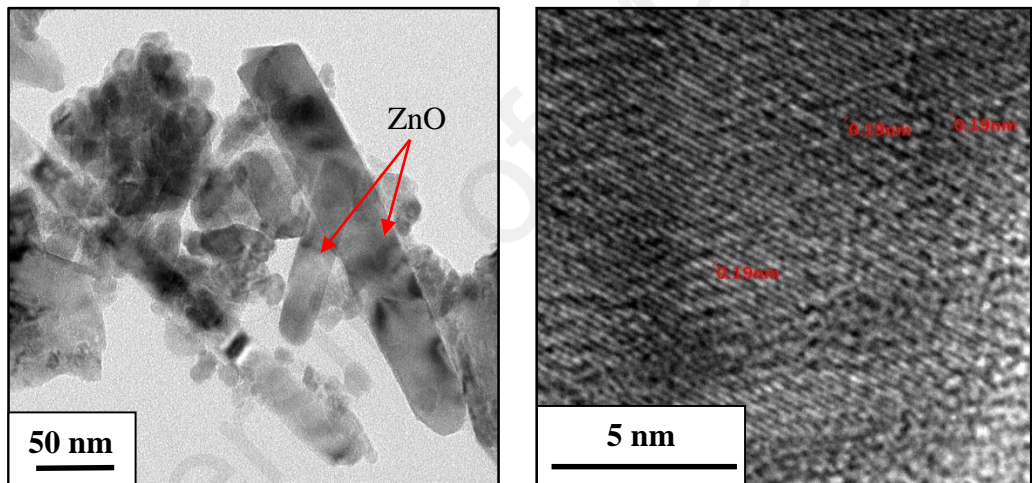


**Figure 4.2: HRTEM images for annealed (400°C) ZnO nanostructure film.**

**Table 4.1: Average compositional ratio of as-prepared, 200°C, 300°C, 400°C, 500°C, 600°C, 700°C, and 800°C annealing temperature of ZnO nanostructure using EDX spectroscopy.**

Element	Atomic percentage (at%)							
	As-prepared	200°C	300°C	400°C	500°C	600°C	700°C	800°C
Zinc	84.32	54.04	44.46	44.54	43.78	42.59	41.53	39.06
Oxygen	15.68	45.96	55.54	55.46	56.22	57.41	58.47	60.94

#### 4.1.1.2 Phase structure analysis by XRD

In this experiment, XRD analysis was used to investigate the influence of thermal treatment on the crystallization and phase transition of the ZnO nanostructure. Figure 4.3 exhibits the XRD patterns of the ZnO nanostructure before and after heat treatment process at temperatures of 200, 300, 400, 500, 600, 700 and 800 °C. The results clearly show that the crystal structure of ZnO was dependent on the heat treatment. This study aims to determine the optimum annealing temperature to obtain the desired properties of ZnO for the excellent PEC water-splitting performance. According to the literature, the wurtzite type of ZnO is an important in semiconductor applications, as compared to other crystal structures of ZnO: zinc blende and rock salt (Fierro, 2010; Manasreh, 2000). As a matter of fact, the significance of wurtzite type ZnO was obtained from the ideal arrangement by changing the  $c/a$  ratio or the  $u$  value. From the experimental observation, the  $c/a$  ratios were smaller than ideal ones. In addition, the  $c/a$  ratio also showed an association of difference for the two constituents' electronegativity. Consequently, the components with the greatest difference showed the greatest departure from the ideal  $c/a$  ratio (Abd Samad *et al.*, 2015b; Fierro, 2010; Kisi & Elcombe, 1989; Manasreh, 2000).

The Bragg reflection of the Zn phase was detected at  $2\theta$  values of 36.3°, 39.0°, 43.2°, 54.3°, 70.0°, 70.7°, and 77.0° in entire XRD patterns, corresponding to (002), (100), (101), (102), (013), (110) and (004) crystal planes, respectively. The presence of the Zn phase was identified by the ICDD file of 00-004-0831 for as-prepared ZnO nanostructure film. This XRD pattern indicated the amorphous nature of as-prepared ZnO [Figure 4.3 (a)]. Meanwhile, for annealed ZnO nanostructure film [Figure 4.3 (b-h)], all samples exhibited diffraction peaks were in line with reference code ICDD 00-036-1451, which indicated the presence of wurtzite type ZnO. The Bragg reflection of the ZnO phase was detected at  $2\theta$  values of 31.7°, 34.5°, 36.3°, 47.6°, 62.3°, 66.4°, 67.9°, 70.0°, and 77.0° in entire

XRD patterns, corresponding to (100), (002), (101), (102), (103), (200), (112), (004), and (202) crystal planes, respectively.

It is worth noting that the sample was crystallized and that a uniform lattice strain was obtained after the annealing process. An increase in the annealing temperature produced an increase in the crystallization state in the ZnO film. Figure 4.3 (f-h) showed very low FWHM diffraction peaks; however, all peaks belonging to ZnO and no Zn peaks appeared. The chemical formula for ZnO was obtained and a hexagonal crystal system with space group P63mc/ C6mc was identified. Besides, the obtained diffraction peak matches the wurtzite type because  $a = 3.2498 \text{ \AA}$ ,  $b = 3.2498 \text{ \AA}$  and  $c = 5.2066 \text{ \AA}$ . As mentioned above, the wurtzite type of ZnO could play an important role in PEC water splitting system compared to other crystal structures of ZnO: zinc blende and rock salt (Fierro, 2010; Kisi & Elcombe, 1989; Manasreh, 2000).

In addition, no obvious other elements were observed in the XRD patterns even a small volume of supporting electrolyte (50 mL 1M KCl) was added into ZnCl<sub>2</sub> electrolyte. It could be understood that supporting electrolyte might affect the formation of the nanostructure as well as the numbers of nucleation sites. In fact, supporting electrolyte is widely utilized in electrochemical quantifications when control of electrode potentials is essential. Indeed, this can be done to eliminate the transportation of electro-active species by ion migration in the electric field and to manipulate the overall electrolyte conductivity, and a fine balance generation rate of Zn(OH)<sub>2</sub> and Cl<sup>-</sup> adsorption rate can be achieved (Abd-Ellah *et al.*, 2013; J. Wang, 2006).

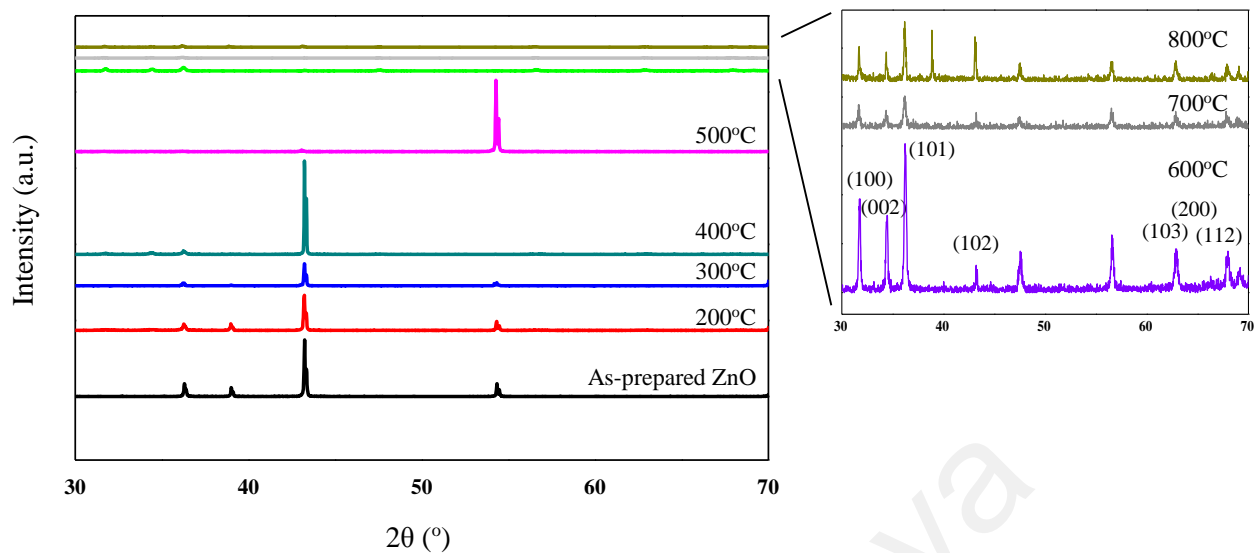


**Figure 4.3: XRD pattern of as-prepared ZnO, 200°C, 300°C, 400°C, 500°C, 600°C, 700°C, and 800°C annealing temperature**

**Table 4.2: Crystallite size of as-prepared ZnO, 200°C, 300°C, 400°C, 500°C, 600°C, 700°C, and 800°C annealing temperature**

Sample	Crystallite size (Å)
As-prepared ZnO	1448
200°C	1187
300°C	1187
400°C	890
500°C	607
600°C	175
700°C	303
800°C	425

#### 4.1.1.3 Photoelectrochemical response

A scanning potentiostat was used to measure current density ( $j$ ) under an applied potential ( $V$ ) characteristic curves could evaluate the PEC water splitting performance by using ZnO nanostructure film as photoelectrode. For a PEC water splitting, an efficiency of over 90% is between -1 and 1 V (S Licht *et al.*, 2000; Stuart Licht *et al.*, 2001). Figure 4.4 exhibits the  $j$ - $V$  characteristic curves for the as-prepared ZnO film and different heat treatment of the ZnO nanostructure film, under a UV ray. Under dark conditions, all samples exhibited non-significant photocurrent density,  $j_p$  of less than  $10 \mu\text{A}/\text{cm}^2$ . However, the photocurrent density increased under UV-ray. In this case, the photocatalytic activity contribution from the ZnO nanostructure film could be observed from the photocurrent generation under UV ray. The  $j_p$  started to increase from the as-prepared sample until a temperature of  $400^\circ\text{C}$  ( $10.96 \text{ mA}/\text{cm}^2$ ) [Figure 4.4]. Under visible light, a  $j_p$  of  $9.06 \text{ mA}/\text{cm}^2$  was observed for the ZnO nanostructure film subjected to the heat treatment of  $400^\circ\text{C}$  [Figure 4.5]. Nevertheless, heat treatment of  $400^\circ\text{C}$  appeared as an optimum temperature even though sample subjected to  $500^\circ\text{C}$  exhibited a better PEC performance ( $11.09 \text{ mA}/\text{cm}^2$  under UV ray and  $6.43 \text{ mA}/\text{cm}^2$  under visible light). The main reason is attributed to the physical appearance of the ZnO nanostructure film itself, which started to deform at temperature of about  $500^\circ\text{C}$  and it suppress the lifespan of ZnO in any application (Fang *et al.*, 2014; Stoica *et al.*, 2014). Starting  $500^\circ\text{C}$  heat treatment temperature, ZnO thin film has started to deform and wrinkled in physical appearance. Therefore, it inhibited the repeatability potential of ZnO usage in PEC water splitting application ( $< 5$  repetition). Based on the results of the photocurrent density for as-prepared ZnO and different annealing temperatures under UV ray and visible light [Table 4.3], the as-prepared ZnO nanostructure film showed poor PEC results ( $1.83 \text{ mA}/\text{cm}^2$  under UV ray and  $1.52 \text{ mA}/\text{cm}^2$  under visible light) due to the existence of an oxygen vacancies point defect inside the ZnO bulk, which pointed to the increasing

number of recombination centres (Fang *et al.*, 2014). The recombination centres clearly contributed to the decrease in photo-induced charge carrier mobility back to the contact of Zn substrate because a series of resistance caused by these trap states was increased. Besides, the amorphous phase comprises a high concentration of other material defects such as impurities, dangling bonds and micro-voids, which similarly act as recombination centres and result in a decrease in  $j_p$  (Lai & Sreekantan, 2014). Predominantly, as-prepared-ZnO film is basically unable to develop a regular depletion region (Ahn *et al.*, 2007). It was found that the  $j_p$  of the heat treated (400 °C) ZnO sample was the optimum temperature of the heat treatment process, which suggests that the well-arranged hexagonal crystal structure of the ZnO wurtzite type can improve the affectivity of photocurrent generation under both UV ray and visible light. Also, the sample subjected to heat treatment of 400 °C was chosen as the most prominent photoelectrode in water splitting system because it has a Zn: O ratio of 1:1, and it exhibited an acceptable photocurrent density under UV ray and visible light. In addition, the higher  $j_p$  of ZnO nano-architecture with annealing temperature 400 °C might be attributed to the strong light scattering effects and high specific surface area for incident light absorption from any direction. In the electrolyte in the PEC system, the large active surface area of ZnO nanostructure film could generate large amount of photo-induced charge carriers and these charge carriers could transfer to the substrate. Using an external circuit, these photo-induced charge carriers travelled to the counter electrode (platinum electrode) and eventually these electrons might reduce the hydrogen ions into hydrogen gases. The PEC water splitting testing stopped at 700°C because at 800°C, the sample was totally deform and out of shape. The ZnO nanostructures thin film were wrinkled and it cannot be connected with the circuit. Therefore, the PEC water splitting cannot be performed.

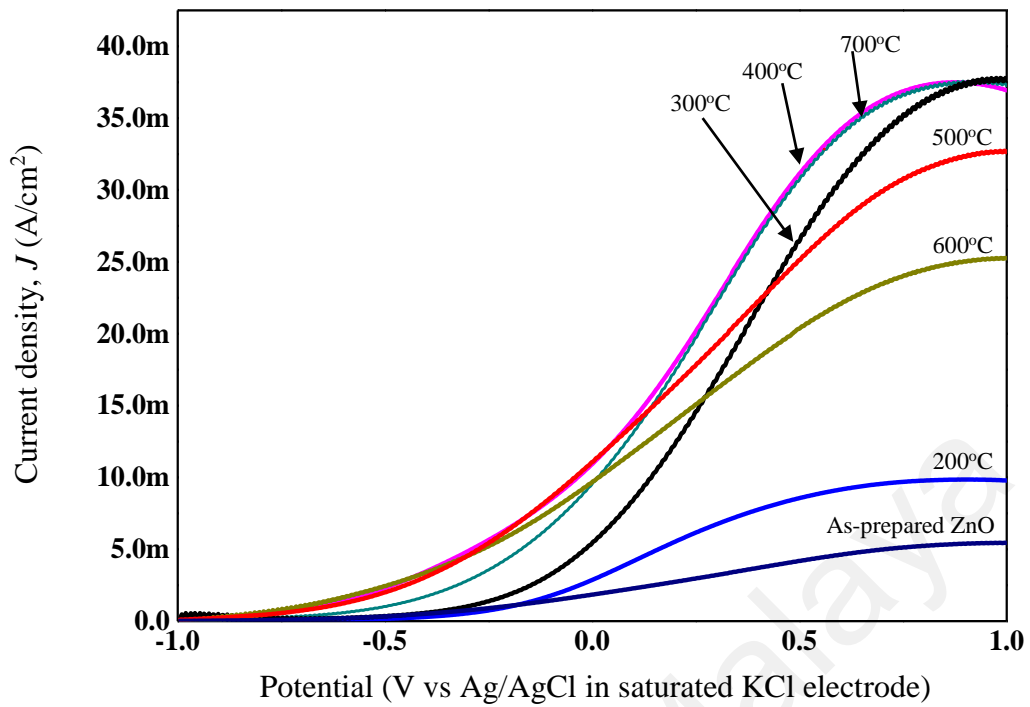


**Figure 4.4:** Photocurrent response for as-prepared ZnO film, 200°C, 300°C, 400°C, 500°C, 600°C, and 700°C annealing temperature under UV ray.

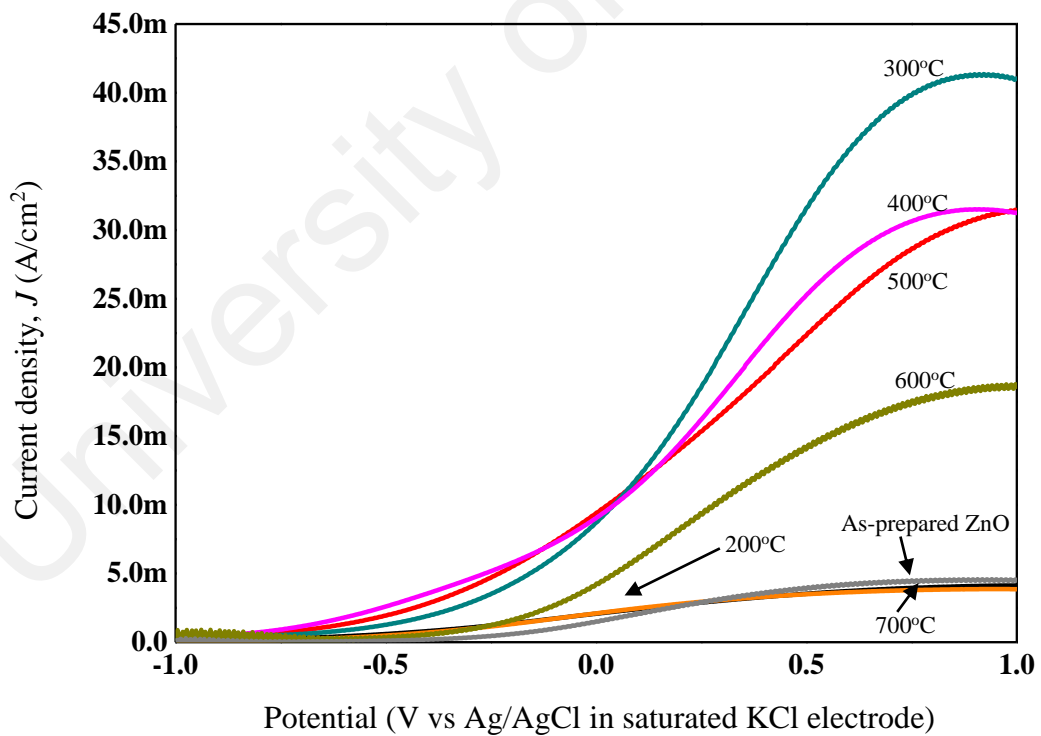


**Figure 4.5:** Photocurrent response for as-prepared ZnO film, 200°C, 300°C, 400°C, 500°C, 600°C, and 700°C annealing temperature under visible light.

**Table 4.3: The photocurrent density (mA/cm<sup>2</sup>) for as-prepared ZnO and different annealing temperatures under UV ray and visible light.**

Sample	UV ray (300nm) (mA/cm <sup>2</sup> )	Visible light (500nm) (mA/cm <sup>2</sup> )
As-prepared ZnO	1.85	1.52
200°C	2.88	2.10
300°C	9.62	8.73
400°C	10.96	9.06
500°C	11.09	9.43
600°C	9.71	4.28
700°C	5.49	2.08

#### **4.1.2 The influence of stirring process towards the formation of ZnO nanostructure film**

Next, stirring process during the electrodeposition technique is also known to play an important role in the formation of ZnO nanostructure film. Therefore, in this part of experiment, electrodeposition process with high speed stirring rate (> 350 rpm) or highly dynamic of electrolyte was investigated. In addition, 0.5 mM ZnCl<sub>2</sub> electrolyte containing 0.1 M KCl, electrolyte temperature of 80°C, exposure time of 60 mins, applied potential of 3 V, and heat treatment at 400°C were constant for all samples. Based on the literature review, the highly dynamic of electrolyte during the electrodeposition will produced 2D and 3D ZnO nanostructures. The optimum speed stirring rate (> 350 rpm) was selected in the present study as it is high enough to produce highly dynamic of electrolyte (G.-R. Li *et al.*, 2007). It could be noticed that the nanodisk-dendritic ZnO film with perfect hexagonal shape was successfully fabricated with high speed stirring rate (> 350 rpm) or

highly dynamic of electrolyte. Based on aforementioned discussion, the as-synthesized nanodisk-dendritic ZnO film with perfect hexagonal shape subsequently annealed at 400 °C. The reason attributed to the efficient charge separation occurred with increasing degree of crystallinity of nanodisk-dendritic ZnO film. It could be observed that prolonged the electrodeposition time or increase the ZnCl<sub>2</sub> concentration might increase the volume of nanodisk-dendritic ZnO film and might improve the PEC water splitting performance. This part of the current study aims to study the formation of 3D ZnO nanostructure to obtain the desired PEC water splitting performance.

#### **4.1.2.1 Morphological studies and elemental analysis by FESEM-EDX**

FESEM micrographs representing the effect of stirring speed of 350 rpm on the ZnO nanostructure film are shown in Figure 4.6. Figure 4.6 (a) clearly shows that the morphologies on the substrate was shrill of nanodisk-dendritic ZnO. In fact, the nanodisk-dendritic zinc oxides have a perfect hexagonal shape with diagonal approximately 1.7 μm and thickness approximately 150.4 nm. The above-discussed statement is in agreement with several researchers which nanodisk-dendritic ZnO film exhibited unique morphology; consist of overlapping nanodisks and self-tiered structure (XY Zhang *et al.*, 2007). The stem and the leaflets were built of hexagonal nanodisks where they were self-arranged and self-assembled and became little leaves. The brief in mechanism of nanodisk-dendritic zinc oxides is as followed; Zn<sup>2+</sup> concentration at the substrate surface decreased by increasing of pH at the beginning of deposition process, lead to slowest growth rate towards (0001). Diffusion of Zn<sup>2+</sup> from (0001) to the substrate surface lead to growing unit and preferential growth at [1000] direction. Although many nanodisks stacked together; important to realize that all of them were poorly lie on the substrate in horizontal position (1000) which is in the x-axis direction and clearly that the hexagonal shape is in symmetry shape. The crystal growth velocity along various planes are depend on the atomic packing density (XY Zhang *et al.*, 2007) [Figure 4.6 (a) and (b)].

Past researchers found the formation of dendrite shape due to the fast growth velocity of Zn ion in the electrolyte (Perel'Man *et al.*, 2008; Xue *et al.*, 2012). Growth mechanism occurred in globally diffusion and later oriented attachment were localized. Dislocation from the early crystal growth happened due to the high velocity of electrolyte (> 350rpm). Therefore, the second hexagonal nanodisk grown was slightly dislocated from the earlier crystal. Another key point is nanodisk-dendritic tips were known to grow in the direction of maximum surface energy. The (1000) facet was out of sorts, therefore it contributed to highest effective surface energy (Hoffmann *et al.*, 1995; XY Zhang *et al.*, 2007).

The EDX spectroscopy analysis was performed and it showed average atomic percentage 42.59% and 57.41% of zinc and oxygen respectively for nanodisk-dendritic ZnO and average atomic percentage 84.32% and 15.68% of zinc and oxygen respectively for as-prepared ZnO [Table 4.4].

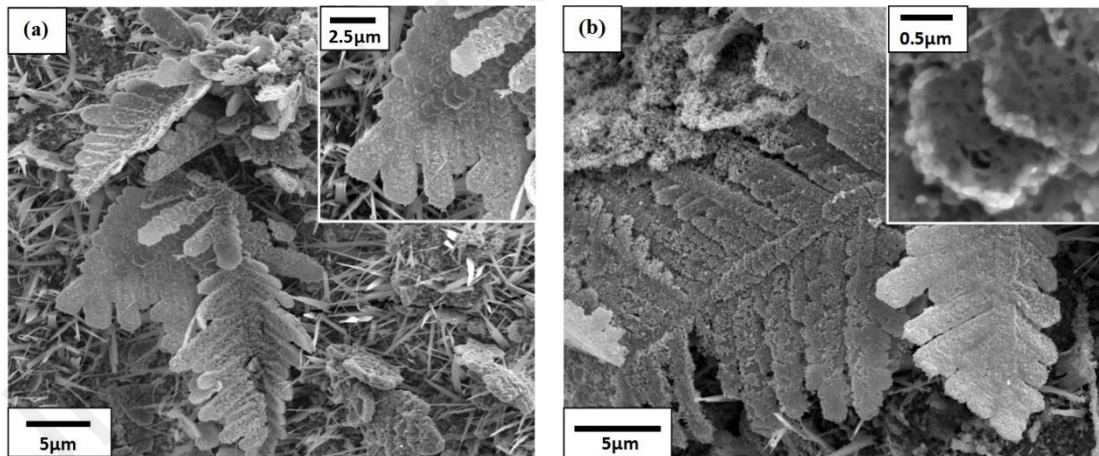


**Figure 4.6: FESEM image of (a) 6k magnification of nanodisk-dendritic ZnO; (inset) 20k magnification of stacked hexagonal-shape nanodisk ZnO, and (b) 10k magnification of nanodisk dendritic ZnO (inset) 100k magnification hexagonal-shape nanodisk ZnO.**

**Table 4.4: Average compositional ratio of nanodisk dendritic ZnO and as-prepared ZnO using EDX spectroscopy analysis.**

Element	Atomic percentage (%)	
	Nanodisk dendritic ZnO	As-prepared ZnO
Zinc	42.59	84.32
Oxygen	57.41	15.68

#### 4.1.2.2 Phase structure analysis by XRD

In this part of experiment, XRD analysis was used to investigate the crystallinity of the nanodisk-dendritic ZnO thin film and as-prepared ZnO thin film as presented in [Figure 4.7]. The XRD pattern of the as-prepared ZnO thin film exhibited major Zn phase, which points to the existence of amorphous nature [Figure 4.7 (a)]. The Bragg reflection of Zn phase was detected at  $2\theta$  values of  $36.3^\circ$ ,  $39.0^\circ$ ,  $43.2^\circ$ ,  $54.3^\circ$ ,  $70.0^\circ$ ,  $70.6^\circ$ , and  $77.0^\circ$  in entire XRD patterns, corresponding to (002), (100), (101), (102), (013), (110) and (004) crystal planes, respectively. The presence of Zn phase was identified by ICDD file of 00-004-0831. Meanwhile, nanodisk-dendritic ZnO thin film [Figure 4.7 (b)], the result showed that the samples were in line with reference code ICDD 00-036-1451 which indicates the ZnO phase. The Bragg reflection of ZnO phase was detected at  $2\theta$  values of  $31.7^\circ$ ,  $34.5^\circ$ ,  $36.3^\circ$ ,  $47.6^\circ$ ,  $62.3^\circ$ ,  $66.4^\circ$ ,  $67.9^\circ$ ,  $70.0^\circ$ , and  $77.0^\circ$  in entire XRD patterns, corresponding to (100), (002), (101), (102), (103), (200), (112), (004), and (202) crystal planes, respectively. It showed that the sample was crystallized and uniform lattice strain was obtained after annealing process. All peaks are shifted to the left as the ZnO crystals were well structured and denser after annealing process. The chemical formula ZnO and crystal system hexagonal with space group of P63mc. It also matched with the wurtzite type because the  $a = 3.25 \text{ \AA}$ ,  $b = 3.25 \text{ \AA}$  and  $c = 5.21 \text{ \AA}$ . The wurtzite type is important in

semiconductor application as compared to other crystal structures of ZnO; zinc blende and rocksalt. The significant of wurtzite type ZnO obtained from the ideal arrangement, by changing the  $c/a$  ratio or the  $u$  value. From experimentally observed,  $c/a$  ratios are smaller than ideal. In addition,  $c/a$  ratio also shows the association of differences for two constituents' electronegativities. Consequently, components with the greatest differences show largest departure from the ideal  $c/a$  ratio (Fierro, 2010; Kisi & Elcombe, 1989; Manasreh, 2000).

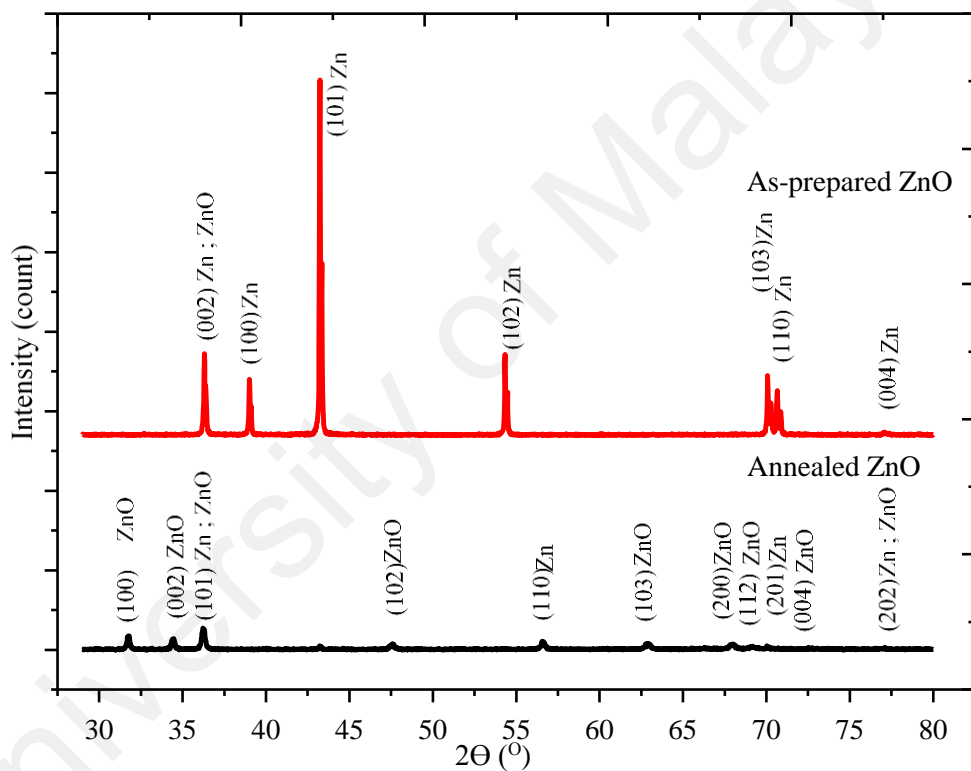


**Figure 4.7: XRD pattern of as-prepared ZnO and annealed ZnO nanodisk-dendritic.**

#### 4.1.2.3 Photoelectrochemical water splitting evaluation

A  $j$ - $V$  characteristic plots for the as-prepared nanodisk-dendritic ZnO film and annealed nanodisk-dendritic ZnO film at 400 °C. As it is a well-known fact that the efficiencies of over 90% is at -1 to 1 V for water electrolysis (S Licht *et al.*, 2000; Stuart Licht *et al.*, 2001). Figure 4.8 was plotted to exhibit  $j$ - $V$  characteristic curves for the (a)

nanodisk-dendritic ZnO film subjected to 400 °C heat treatment, (b) as-prepared ZnO film under UV ray and (c) nanodisk-dendritic ZnO film subjected to 400 °C heat treatment in dark condition. The significant photocurrent density,  $j_p$  of an average value of 19.87 mA/cm<sup>2</sup> for nanodisk-dendritic ZnO under UV ray [Figure 4.8 (a)] was obtained as compared to 6.45 mA/cm<sup>2</sup> and 1.49 mA/cm<sup>2</sup> for as-prepared ZnO under UV-ray [Figure 4.8 (b)] and nanodisk-dendritic ZnO without illumination [Figure 4.8 (c)] respectively. A maximum  $j_p$  of 19.87 mA/cm<sup>2</sup> was observed for the nanodisk-dendritic ZnO film subjected to 400 °C heat treatment, which is relatively high compared to the as-prepared sample (6.45 mA/cm<sup>2</sup>) under UV ray. These results are in line with literatures, which suggested that the presence of nanodisk-dendritic nanostructure can provide a high degree of electrons mobility to the substrate, which will greatly reduce interface recombination. In addition, large number of active reaction sites for chemical reactions to occur and allow more photo-induced electrons generated for the hydrogen reduction process during illumination. However, it could be noticed that the current density,  $j$  value decreased with the increasing of spectrum wavelength until visible light spectrum (390-700 nm) reached. Under visible light, average  $j_p$  of 14.05 mA/cm<sup>2</sup> was observed for the nanodisk-dendritic ZnO film subjected to 400 °C heat treatment [Fig. 4.9 (a)], which is relatively high as compared to as-prepared ZnO under visible light;  $j_p$  2.14 mA/cm<sup>2</sup> [Fig. 4.9 (b)] and 1.49 mA/cm<sup>2</sup> nanodisk-dendritic ZnO without illumination [Fig. 4.9 (c)].

Based on the results of  $j_p$ - $V$  characteristic curves [Fig. 4.8 and 4.9], as-prepared-ZnO film showed poor PEC water splitting response due to the existence of oxygen vacancies point defect inside ZnO bulk, which point to the increasing number of recombination centers (Abd Samad *et al.*, 2015a). The recombination centers clearly contributed to the decreasing of photo-induced charge carrier mobility back to the contact of Zn substrate because series of resistance caused by these trap states has been increased. Besides, the amorphous phase of ZnO comprised of high concentration of other material defects

including impurities, dangling bonds, and micro-voids, which similarly acted as recombination charge carriers center and eventually resulted in a decrease of  $j_p$  (Lai & Sreekantan, 2014). Predominantly, as-prepared-ZnO film is basically unable to develop a regular depletion region (Ahn *et al.*, 2007). It was found that the  $j_p$  of heat treated nanodisk-dendritic ZnO sample was slightly increased to 19.87 mA/cm<sup>2</sup>, which suggested that crystal structure of nanodisk-dendritic ZnO sample could improve the current generation effectively. In addition, the higher  $j_p$  of nanodisk-dendritic architecture might be contributed to the strong light scattering effects and high active surface area for nanodisk-dendritic architecture for incident light absorption from any direction. The reason for the observed trend is attributed mainly to the nanodisk-dendritic ZnO film subjected to 400 °C heat treatment can harvest more incident photons from the illumination to generate photo-induced charge carriers for PEC water splitting reactions [2H<sup>+</sup> + 2e<sup>-</sup> → H<sub>2</sub>].

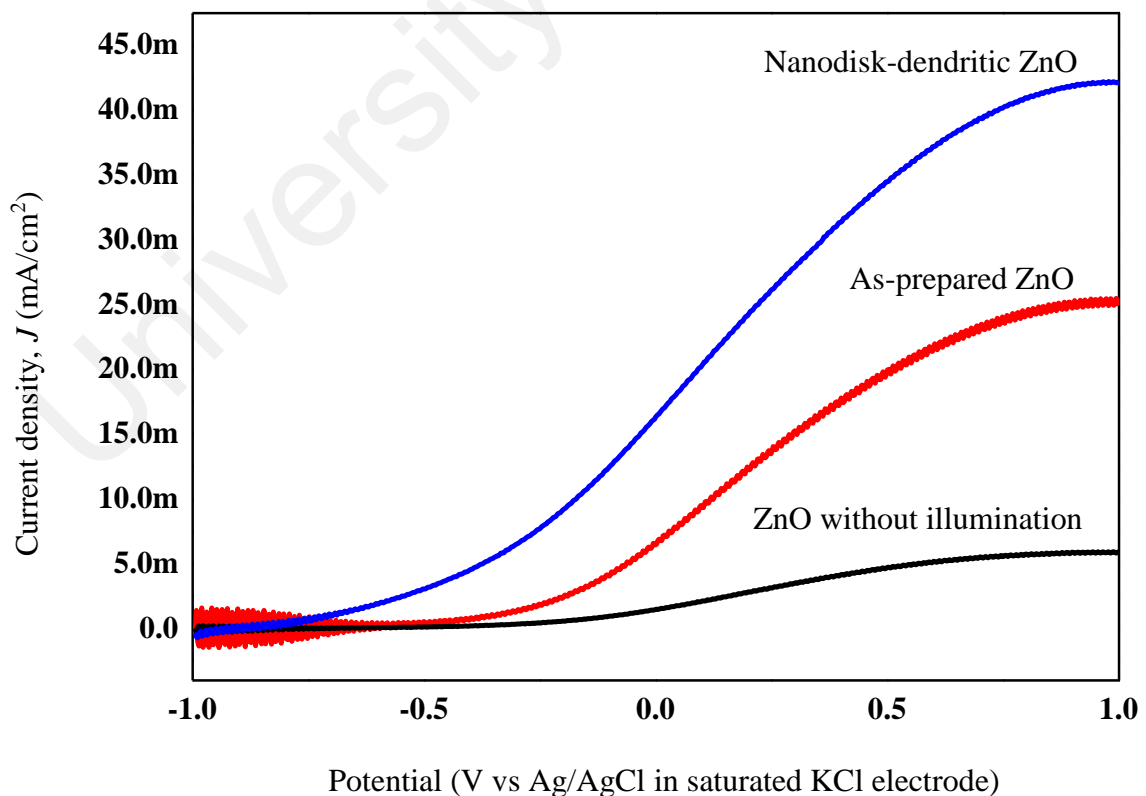


**Figure 4.8: Photocurrent response for nanodisk-dendritic ZnO, as-prepared ZnO under UV ray and nanodisk-dendritic ZnO without illumination.**

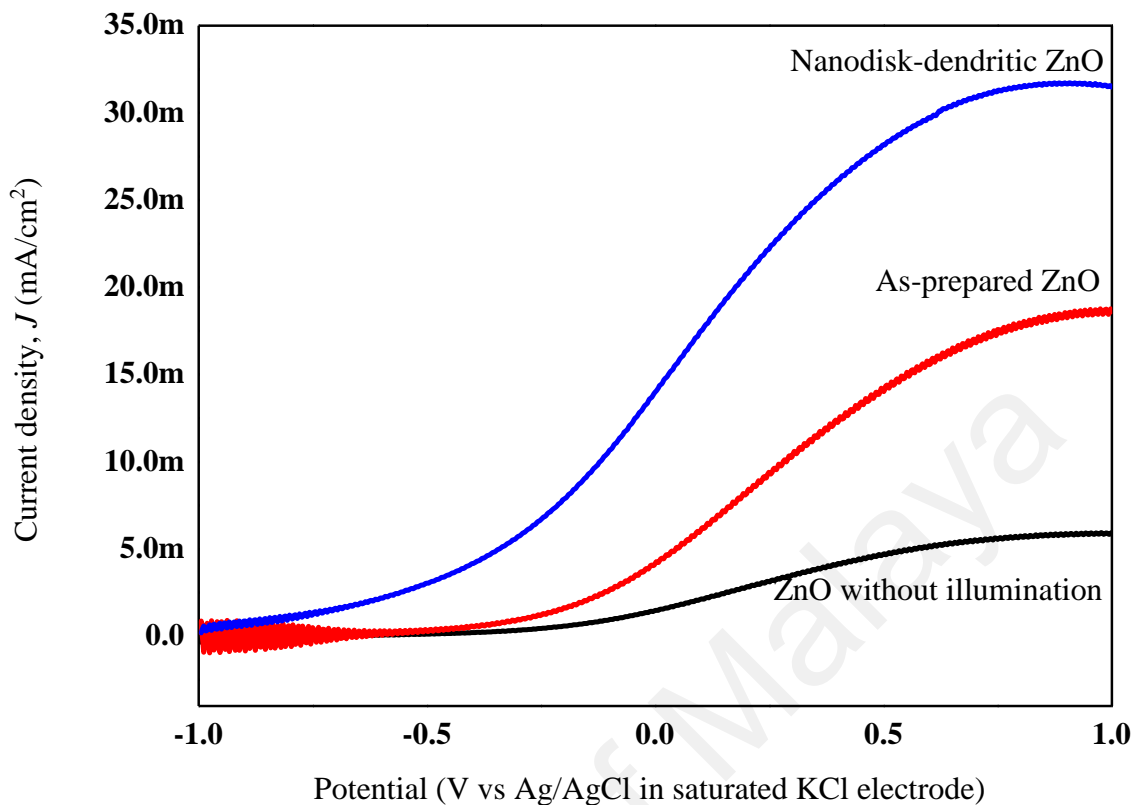


**Figure 4.9: Photocurrent response for nanodisk-dendritic ZnO, as-prepared ZnO under visible light and nanodisk-dendritic ZnO without illumination.**

#### 4.1.3 The influence of reaction temperature towards the formation of ZnO nanostructure film

##### 4.1.3.1 Morphological studies and elemental analysis by FESEM-EDX

The current section discusses the influence of reaction temperature on the morphology of the ZnO nanostructure film. The reaction temperature was varied from 40 °C to 100 °C. But, 0.5 mM ZnCl<sub>2</sub> electrolyte containing 0.1 M KCl electrolyte, very slow stirring rate, exposure time of 60 mins, applied potential of 3 V, and heat treatment at 400°C were constant for all samples.

Figure 4.10 clearly shows that the reaction temperature during electrodeposition process affects the geometric features of the nanostructure on the Zn substrate. Goux *et al.* stated that the main effect of reaction temperature is the texturation of *c*-axis ZnO film.

It could be noticed that at reaction temperatures between 40 °C to 60 °C [Figure 4.10 (a)-(c)], it lack crystal growth of ZnO after 60 minutes of electrodeposition technique. Indeed, this processing condition can be proven by the FESEM image that illustrated in the formation of small and irregular structures of ZnO architecture on the Zn substrate. From the EDX analysis, a high atomic percentage ratio of Zn was deposited onto the substrate as compared to O could be observed. Therefore,  $Zn^{2+}$  tended to be deposited rather than  $Zn(OH)_2$  could be proposed because the pH was neutral and condition of solubility was not sufficient to achieve the supersaturation condition for the nucleation of  $Zn(OH)_2$ , followed by the dehydration process and then ZnO formation. Several researchers have been stated that the formation of ZnO could be observed after a time delay. Prolonged electrodeposition exposure time would give more time to  $Zn(OH)_2$  to dehydrate and form ZnO. This reason mainly attributed to the slow dehydration process for ZnO formation (Goux *et al.*, 2005; Peulon & Lincot, 1998).

Starting from 70 °C to 80 °C [Figure 4.10 (d) - (e)], the nucleation of  $Zn(OH)_2$  occurred quickly because the temperature increase helped in increasing the local pH. Increasing in local pH at Zn substrate initiated the  $Zn(OH)_2$  nucleation, and was followed by the dehydration process and induced ZnO crystal growth (Goux *et al.*, 2005). Further increasing the temperature to 90 °C to 100 °C [Figure 4.10 (f) - (g)], the crystal growth lacked direction. However, the EDX analysis showed it had an acceptable stoichiometry of the Zn to O ratio [Table 4.5].

Otani *et al.*, Li *et al.*, and Goux *et. el.* proposed polar (001), non-polar (101), and surface (100) were influenced when the reaction temperature were increased. Thermodynamic stability was increased at high temperature (Goux *et al.*, 2005; Q. Li *et al.*, 2010; Otani *et al.*, 2006). Otani *et al.* and Goux *et. al.* indicated increase in reaction temperature will increase the local pH at substrate.  $H^+$  and  $OH^-$  ions are highly consumed

at higher temperature with pH increased. Therefore, thermodynamic stability was achieved to form  $\text{Zn(OH)}_2$  and followed by formation of  $\text{ZnO}$  (Goux *et al.*, 2005; Otani *et al.*, 2006). Increase in temperature helped in pH increment via the highest activity of  $\text{H}^+$  and  $\text{OH}^-$  ions activity (Barron *et al.*, 2006). The mechanism under the influenced of reaction temperature as in Figure 4.11. At high reaction temperature, the crystals arrangement are more organize as compared to low reaction temperature which produces loosely arrangement of  $\text{ZnO}$  crystals.

University of Malaya

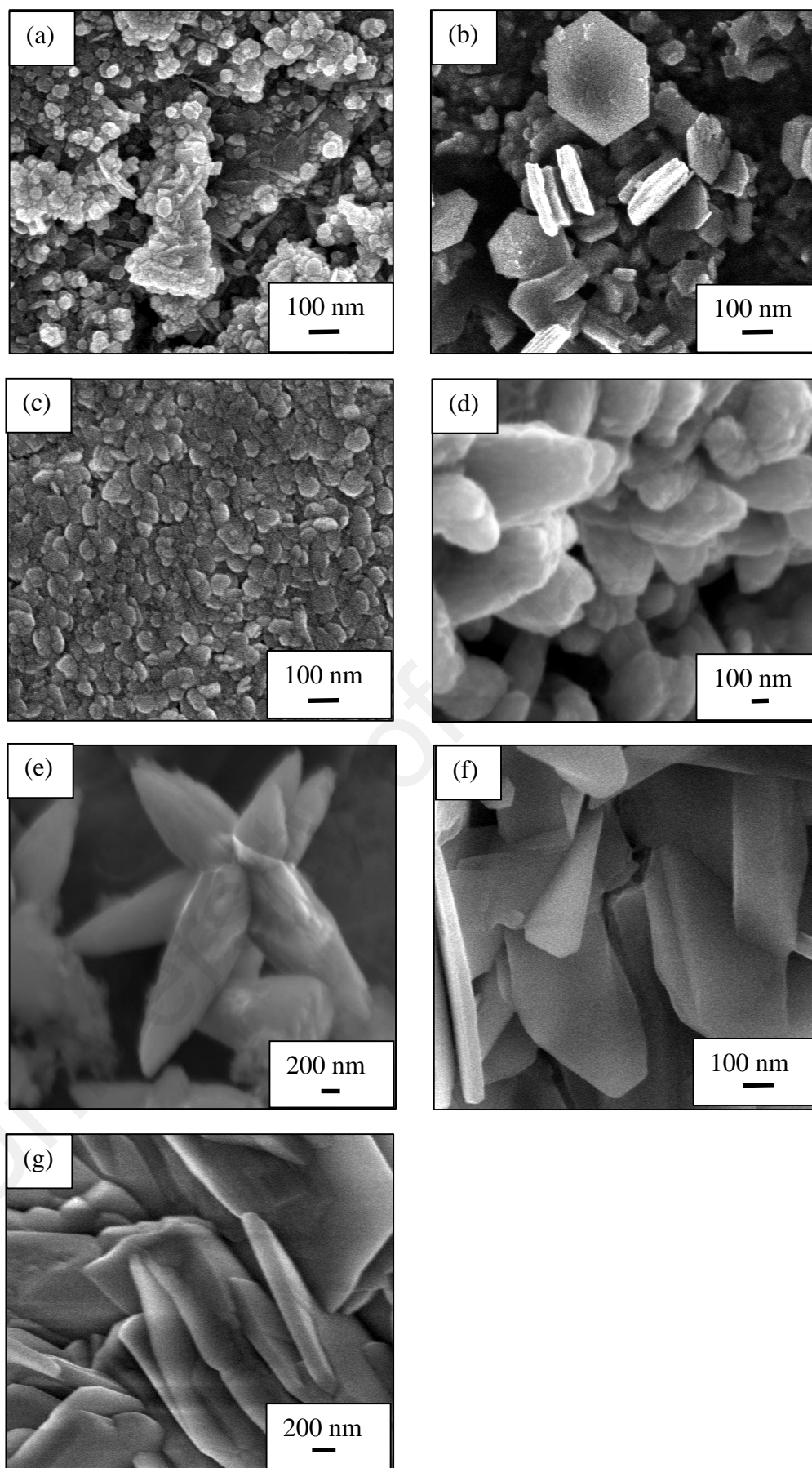


**Figure 4.10: FESEM images of ZnO nanostructures (a) 40°C, (b) 50°C, (c) 60°C, (d) 70°C, (e) 80°C, (f) 90°C, and (g) 100°C electrolyte bath temperature.**

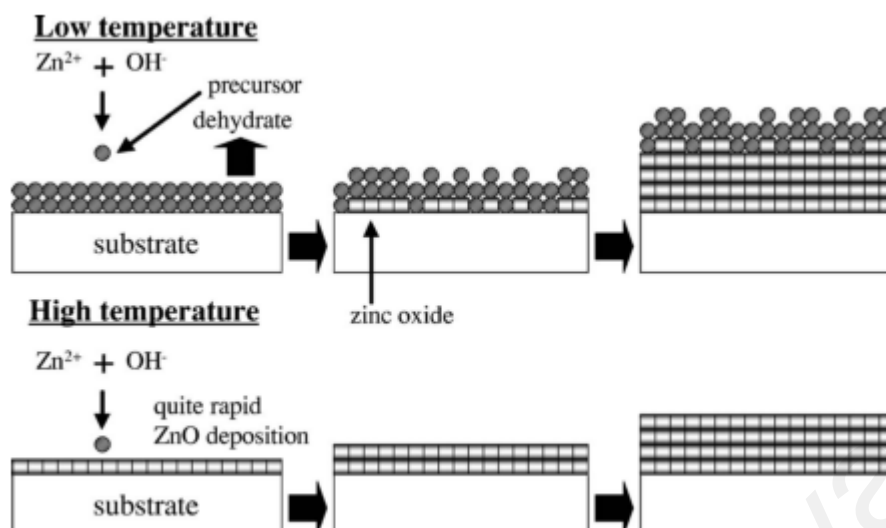


**Figure 4.11: Schematic diagram of ZnO nanostructure mechanism under the influenced of reaction temperature adapted from “Effect of Bath Temperature on the Electrodeposition Mechanism of Zinc Oxide Film from Zinc Nitrate Solution” by Otani *et. al.* (2006). Copyright 2014 by the authors.**

**Table 4.5: Average compositional ratio of ZnO nanostructures at 40°C, 50°C, 60°C, 70°C, 80°C, 90°C, and 100°C electrolyte bath temperature.**

Element	Atomic percentage (%)						
	40°C	50°C	60°C	70°C	80°C	90°C	100°C
Zn	83.6	72.1	65.2	55.9	54.8	40.6	52.1
O	16.4	27.9	34.8	44.1	45.2	59.4	47.9

#### 4.1.4 The influence of exposure time towards the formation of ZnO nanostructure film

##### 4.1.4.1 Morphological studies and elemental analysis by FESEM

The exposure time during electrodeposition process known to play a crucial role in determining the formation mechanism of ZnO nanostructure. Therefore, in this part of experiment, electrolyte containing 0.5 mM ZnCl<sub>2</sub> and 0.1 M KCl was investigated in

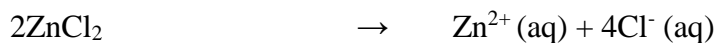
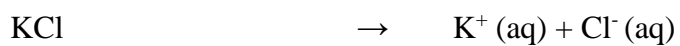
different exposure time from 15 min up to 2 h. In addition, very slow stirring rate, electrolyte temperature of 70°C, applied potential of 3 V, and heat treatment at 400°C were constant for all samples.

The variations in surface morphologies of the ZnO with different exposure time during electrodeposition process are shown in Figure 4.12. In the present study, two steps process took place under dynamic electrolyte for the formation of ZnO nanostructures film. The first step was the formation of zinc hydroxide ( $\text{Zn(OH)}_2$ ), followed by formation of zinc oxide (ZnO). However, this process occurred at all time until the reaction stopped. In the first place, the process started with dissolution of zinc chloride, potassium chloride and water into potassium ion ( $\text{K}^+$ ), zinc ion ( $\text{Zn}^{2+}$ ), chloride ion ( $\text{Cl}^-$ ), hydroxide ion ( $\text{OH}^-$ ) and formation of hydrogen gas ( $\text{H}_2$ ) occurred in the electrolyte (Equation 4.1). The dissolution process occurred due to the energy supplied from direct electric current separated the electrolyte into ions (Barthel *et al.*, 1998; Boddenberg, 1996).

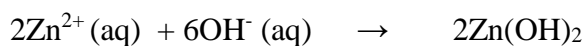
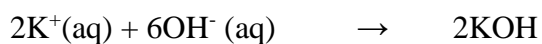
Then, formation of zinc hydroxide ( $\text{Zn(OH)}_2$ ) (intermediate growth stage) (Equation 4.2) followed by zinc oxide (ZnO) (Equation 4.3) occurred at nearby the cathode. The potassium ion ( $\text{K}^+$ ) attracted hydroxide ion ( $\text{OH}^-$ ) to the cathode which played a role as a directing agent. Normally, the unit growing in the [1000] direction was preferred and therefore increased in diameter (Abd Samad *et al.*, 2015b; XY Zhang *et al.*, 2007). However, upon achieving steady state, the propagation or crystal growth at direction [1000] would be terminated and the nucleation of new crystals started in the direction of [0001] again. The process would repeat until the applied potential stopped.

A summary on the formation of ZnO is as follows [Figure 4.13]: (A) The substrate was given an electric supply, (B) deposition of  $\text{Zn(OH)}_2$ , (C) formation of ZnO seeds, and (D) dehydration process, followed by the formation of ZnO. Given below are the chemical reactions involved in the formation of ZnO:

Dissolution of  $\text{KCl} + \text{ZnCl}_2 + \text{H}_2\text{O}$  :



Formation of zinc hydroxide ( $\text{Zn}(\text{OH})_2$ ) :



Formation zinc oxide ( $\text{ZnO}$ ) :



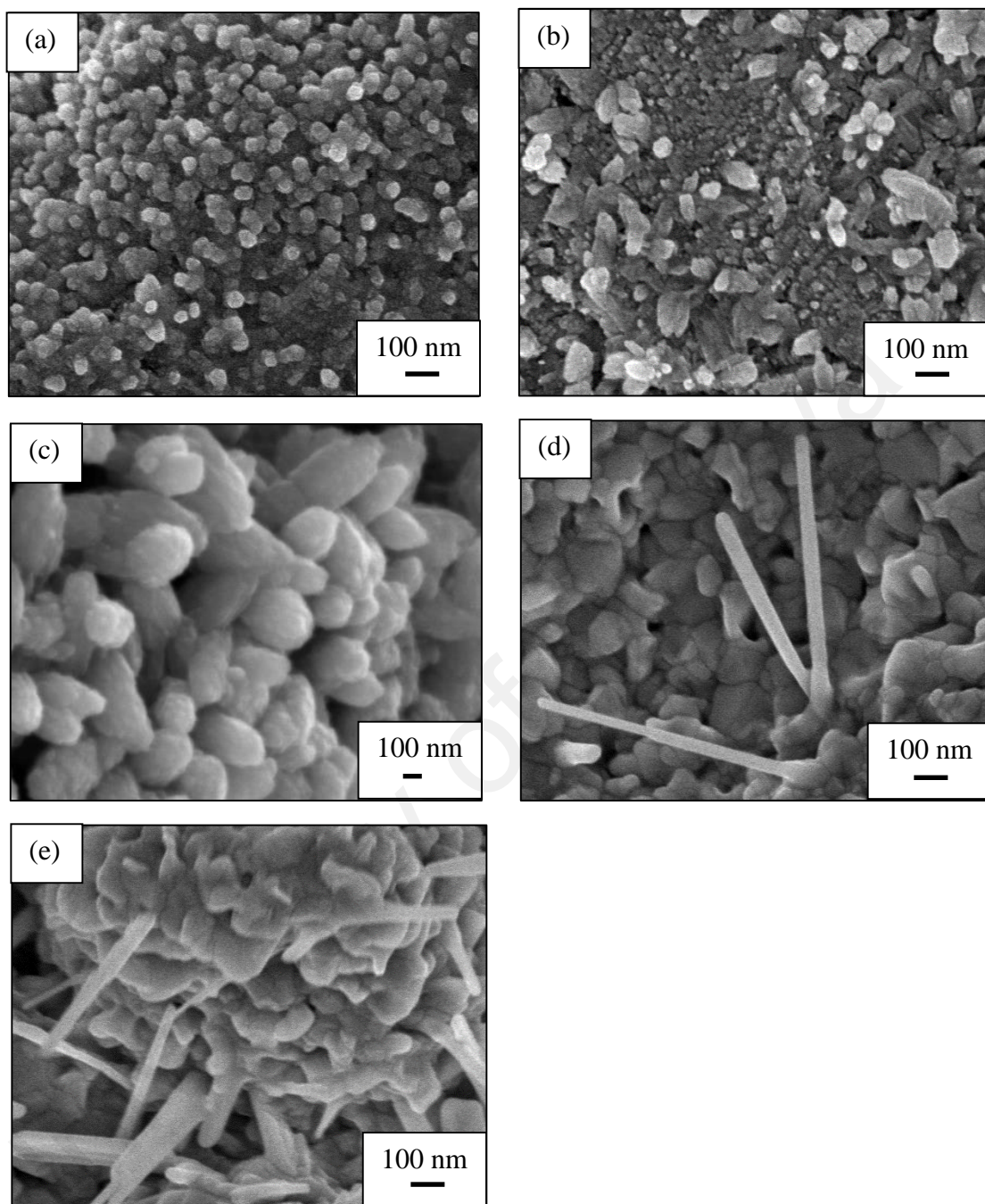


**Figure 4.12: FESEM images of ZnO nanostructures at (a) 15 min, (b) 30 min, (c) 60 min, (d) 90 min, and (e) 120 min exposure time**

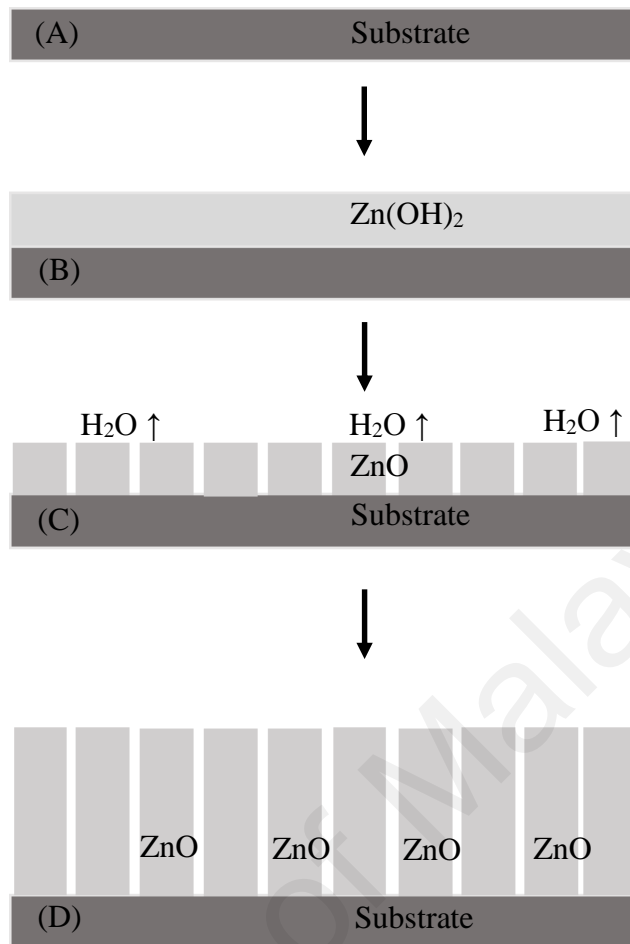


**Figure 4.13: Formation of the ZnO.**

#### **4.1.5 The influence of applied potential towards the formation of ZnO nanostructure film**

An electrodeposition applied voltage controls electrodeposition reactions and, thus, varies the nanostructure of the ZnO could be formed. Therefore, the experimental works was performed in 0.5 mM ZnCl<sub>2</sub> electrolyte containing 0.1 M KCl for 60 min. Other parameters that constant were electrolyte temperature of 70°C, very slow stirring rate, and heat treatment at 400°C.

The voltage was varied from 1 V to 3 V. Figure 4.14 clearly shows that the applied voltage affects the geometric features of the ZnO on Zn substrate. It was found that the optimum electrolyte mixture consisted of 0.5 mM ZnCl<sub>2</sub>, 0.1 M KCl, pH value of ~ 5-6, electrochemical deposition temperature of ~70 °C and a very low stirring rate. Since our

aim is to produce 1D ZnO, low stirring process is preferred. When this optimum electrolyte mixture was run through an applied potential of 1 V and other important conditions, ZnO nanostructures film were successfully produced with the highest average aspect ratio morphology [Table 4.7]. Based on the results obtained, the resultant sample exhibited the highest photocurrent density,  $J_p$ , with a value 17.8 mA/cm<sup>2</sup> under UV ray and 12.94 mA/cm<sup>2</sup> under visible light throughout the potential window. The detail investigations on the influence of applied potential towards the formation of ZnO nanostructure film will be elaborated in the following section.

#### **4.1.5.1 Morphological studies and elemental analysis by FESEM-EDX and HRTEM**

The appearance of deposited ZnO on Zn substrate can be said to be dependent on the applied potential during electrodeposition with an optimum set of other variables like 0.5 mM ZnCl<sub>2</sub> and 0.1 M KCl electrolyte, pH level of ~5-6, electrochemical deposition temperature ~70°C. Dimensions and uniformity of the morphology of ZnO were a function of the applied potential in the ZnCl<sub>2</sub> and KCl electrolyte. For samples deposited under 1 V [Figure 4.14 (a)], nanorods with an average diameter of 37.9 nm and average length of 249.5 nm were produced with near perfect *c*-direction when the applied potential was increased to 2 V, the diameter of the nanorods become slightly larger with an average of 61.6 nm but with shorter average lengths of 211.2 nm [Figure 4.14 (b)].

In this manner, increases in applied potential produced reductions in lengths as higher precursor dissolution occurred at higher potentials and the Zn<sup>2+</sup> concentrations were higher in the [0001] direction. Hence, the unit growing in the [1000] direction was preferred and therefore lead to increase in diameter (Abd Samad *et al.*, 2015b; XY Zhang *et al.*, 2007). The propagation or crystal growth at direction [1000] would be terminated upon steady state and the nucleation of new crystals started in the direction of [0001]

again. The process would repeat until the applied potential stopped. However, any further increases in applied potential to 3V would cause irregular features on the surface of the Zn foils and create a dense ZnO structure instead of ordered nanopores that were previously observed.

It can be concluded that higher applied potentials produced negative effects on the self-ordering of the deposited zinc oxide, whereby the nanorods structure disappeared and the deposited zinc oxide would be composed of irregular and dense structures with thicknesses of  $\sim 2.78 \mu\text{m}$ , as shown in Figure 4.14 (c). Therefore, a minimum potential of 1 V was found to be optimum for the formation of self-organized ZnO nanorods with lengths approaching 249.5 nm in 60 minutes. On the other hand, the lattice fringes of 1 V samples measured 0.23 nm and indicated a (101) ZnO wurtzite [Figure 4.14 (d)]. The final morphology of ZnO nanorods was the competition of field-assisted dissolution and field-assisted deposition of ZnO. By applying higher potentials, strong electric fields helped to accelerate the three-step formation of ZnO nanorods. The driving force of externally applied potential lead to the dissolution of  $\text{ZnCl}_2$ , KCl, and water (field-assisted dissolution). When the ionic species arrived at the cathode under the influence of applied potential, there was a difference between the actual concentration and solubility concentration (supersaturation) due to the increased local pH of KOH at the cathode which produced a very high supersaturation. Therefore, [3] the nucleation of ZnO was started (the field-assisted deposition) by the dehydration process of  $\text{Zn}(\text{OH})_2$  to ZnO (Abd-Ellah *et al.*, 2013; Abd Samad *et al.*, 2015b). EDX spectroscopy showed averages of 50.3 at% Zn and 49.7 at% O, 51.7 at% Zn and 48.3 at% O and 55.9 at% Zn and 44.1 at% O for the respective 1V, 2V and 3V applied potential samples [Table 4.6]. Below is the summary of the diameter, length and aspect ratios of 1V, 2V, and 3V are shown in Table 4.7.

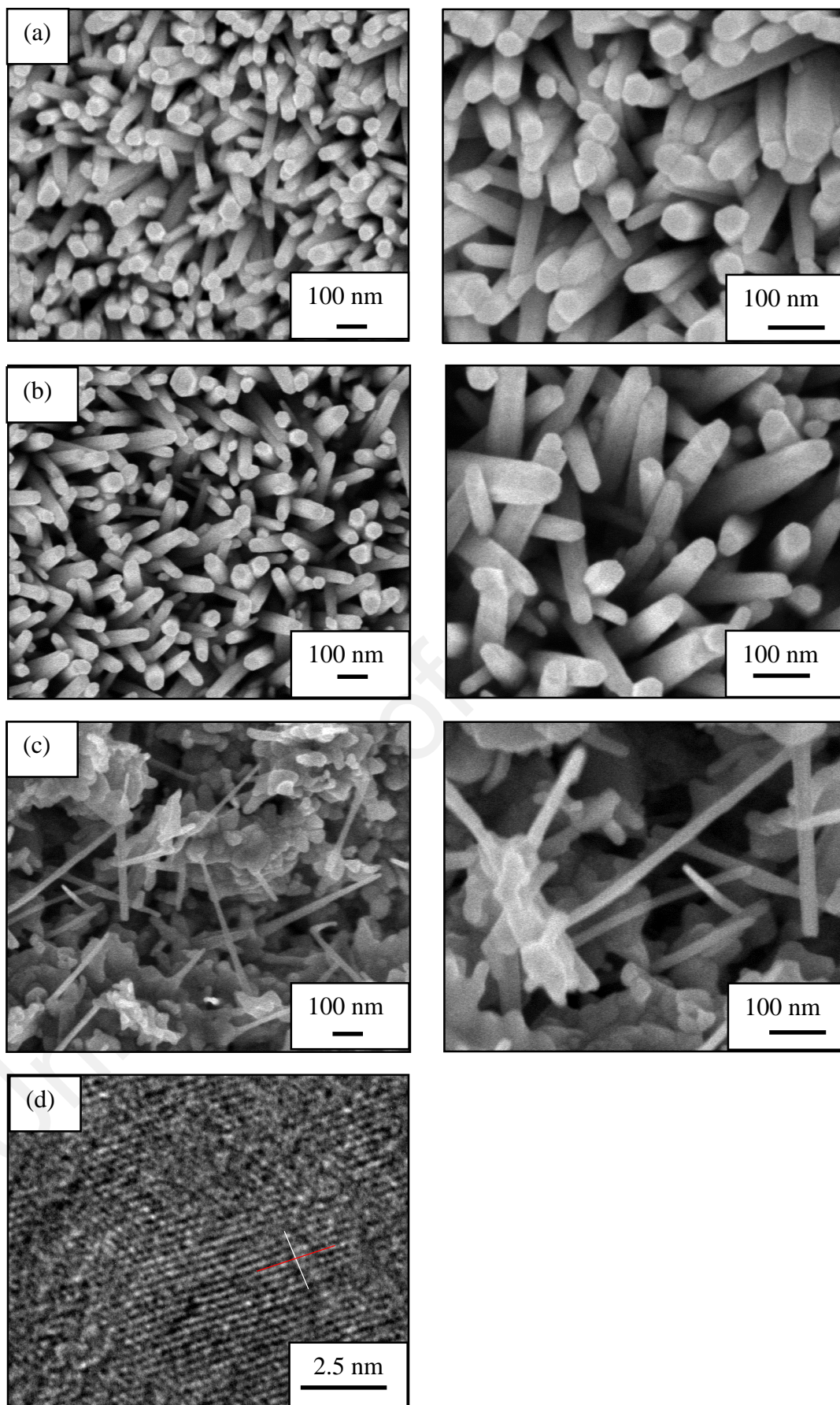


**Figure 4.14: FESEM images (a) 1V of electrodeposition applied potential; (b) 2V of electrodeposition applied potential; (c) 3V of electrodeposition applied potential; and HRTEM image (d) 1V of electrodeposition applied potential.**

**Table 4.6: Average compositional ratio for 1 V, 2 V, and 3 V applied potential from EDX spectroscopy.**

Element	Atomic percentage (%)		
	1 V	2 V	3 V
Zn	50.3	51.7	55.9
O	49.7	48.3	44.1

**Table 4.7: Average value for length, diameter and aspect ratio for different applied potential.**

Potential (V)	Surface morphology	Length (Å)	Diameter (Å)	Average aspect ratio
1	Nanorod	2495 ± 103	379 ± 12	6.58
2	Nanorod	2112 ± 98	616 ± 16	3.43
3	Dense structure	27890 ± 225	-	-

#### 4.1.5.2 Phase structure analysis by XRD and Raman Scattering

In this study, Raman analysis was used to determine and understand the structural changes of ZnO with different applied potential. Raman inelastic scattering is shown at peak E<sub>2</sub> (high) mode at 438 cm<sup>-1</sup> and indicated that the ZnO nanostructures' thin film had crystal wurtzite structures and with the highest intensity at 1 V (796.5 counts) [Figure 4.15 (a)] as compared to 2 V (468.4 counts) and 3 V (459.7 counts) [Figure 4.15 (b) and (c)]. However, these thin films in both samples were still weak in pure stoichiometric ZnO due to the dominant of E<sub>1</sub> (LO) and A<sub>1</sub> (LO) mode (570-585 cm<sup>-1</sup>) as compared to

$E_2$  (high) mode at  $438\text{ cm}^{-1}$  and this situation normally occurs in Zn rich ZnO thin films. This can also be due to a deficiency in oxygen atoms represented by these two modes ( $E_1$  (LO) and  $A_1$  (LO) mode ( $570\text{-}585\text{ cm}^{-1}$ )) and with the existence of Zn elements from the Zn substrate (Exarhos & Sharma, 1995; Schumm *et al.*, 2007). Besides this, the shift in the peaks occurred due to the differences in structure. For the 1 V and 2 V sample, it appeared that ZnO nanorods and the asymmetric LO phonon peaks were observed at  $571\text{ cm}^{-1}$ . Meanwhile, the 3 V samples has dense structures (ZnO bulk crystal), therefore the frequency of the LO phonon was located at  $574\text{ cm}^{-1}$  (K. Dai *et al.*, 2008). In addition to this, many researchers found that the shift occurred at least  $3\text{ cm}^{-1}$  (H.-M. Cheng *et al.*, 2005; Z. Wang *et al.*, 2002; Yingling Yang *et al.*, 2006). The shift of the peak occurred due to the defects or impurities in the nanocrystals, optical phonon confinement, laser irradiation heating, and the tensile strain effect (Alim *et al.*, 2005; K. Dai *et al.*, 2008). Furthermore, the intensity of the peaks was reduced by increasing the applied potential. This occurred due to the quality of the materials which in turn also affected the Raman intensity where higher crystalline quality exhibited higher intensity. Increases in grain size also produced a substantial reduction in asymmetry and intensity of the peaks (Roy *et al.*, 2003).

The XRD pattern supported the Raman scattering as it showed that the ZnO nanorods are in wurtzite phase which belong to the reference code ICDD 00-036-1451 with a hexagonal crystal system. The plane attributes for this ZnO were  $31.7^\circ$  (100),  $34.4^\circ$  (002),  $36.3^\circ$  (101),  $47.5^\circ$  (102),  $56.6^\circ$  (110),  $62.9^\circ$  (103), and  $67.9^\circ$  (112) [Figure 4.16]. The wurtzite ZnO crystallographic lattice parameters were  $a=3.25\text{\AA}$ ,  $b=3.25\text{\AA}$  and  $c=5.21\text{\AA}$ , which confirmed that the number of alternating planes consisted of  $\text{O}^{2-}$  and  $\text{Zn}^{2+}$  that were stacked in tetrahedral along the  $c$ -axis (Z. L. Wang, 2004). The  $43.2^\circ$  (101) and  $76.9^\circ$  (004) showed the apparent existence of Zn elements which also reinforced the Raman scattering results [Figure 4.16].

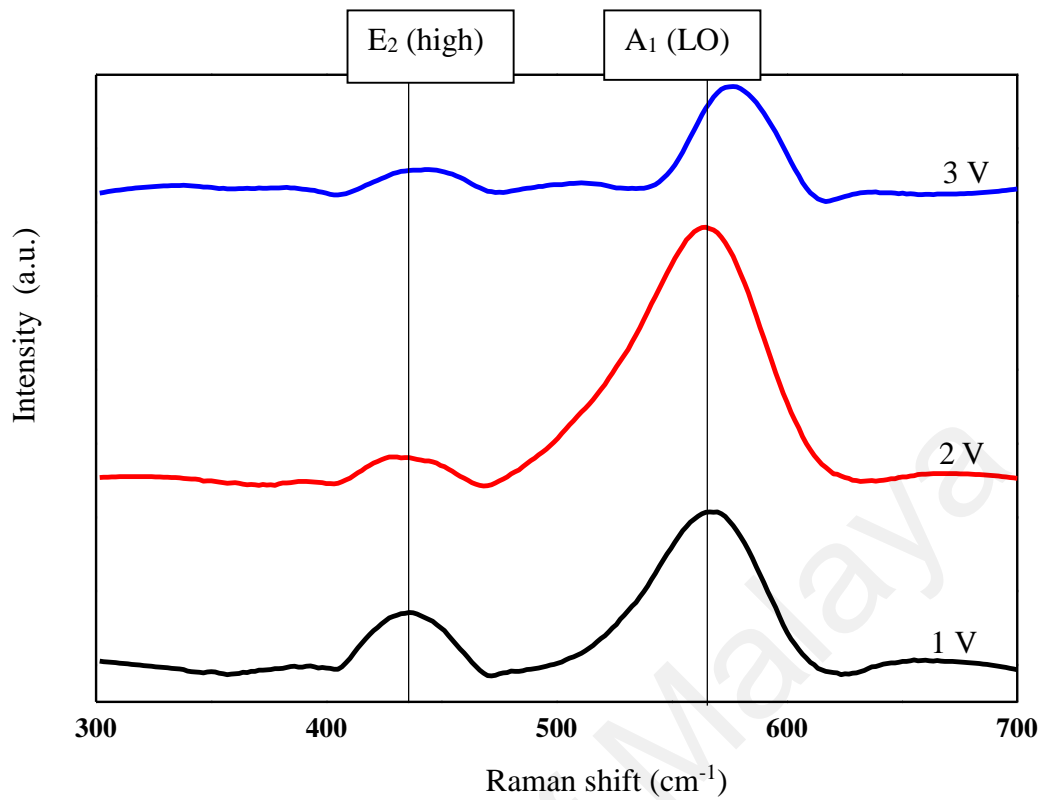


**Figure 4.15:** Raman spectra for 1 V, 2 V, and 3 V (excitation:  $\lambda = 514 \text{ nm}$ ).

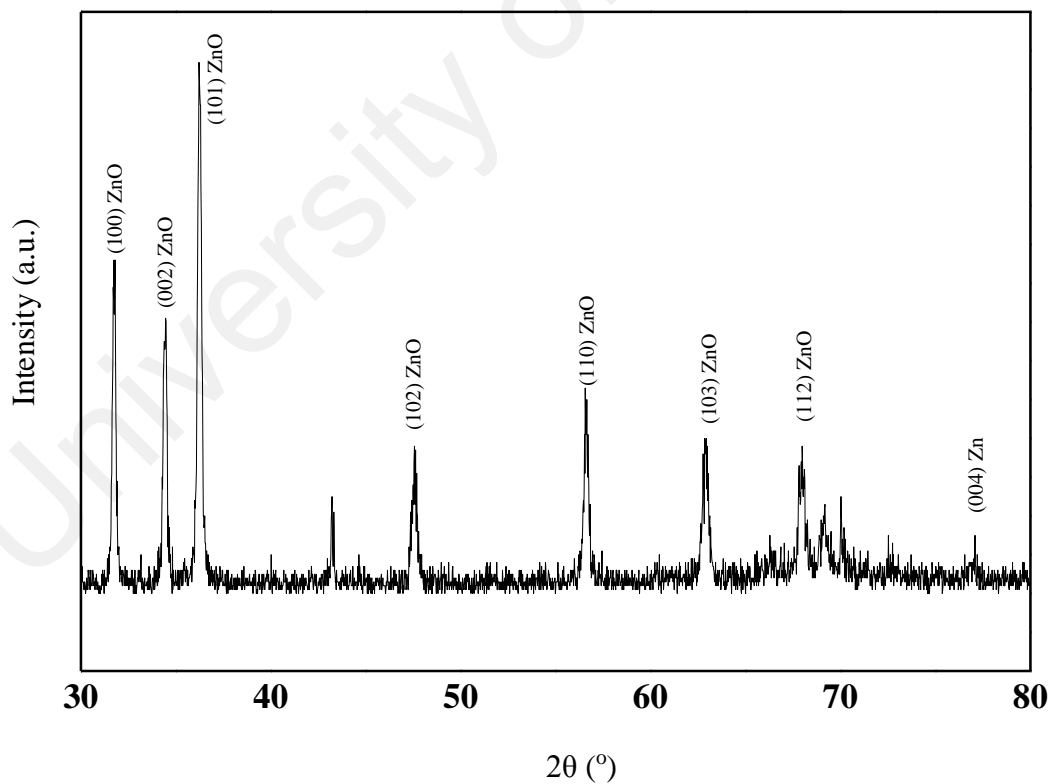


**Figure 4.16:** The XRD pattern for ZnO nanorod for 1 V applied potential.

#### 4.1.5.3 Charge carriers recombination by PL

The photoluminescence study for ZnO nanorods was mainly related with some defects, for instance the zinc vacancies, zinc interstitial, oxygen vacancies, oxygen interstitial and oxygen anti-sites. In the 350-450 nm region, it determine the exciton recombination process and is triggered by the recombination of free excitons, which points to the good crystallinity of the ZnO nanorods (Chandrinou *et al.*, 2009; Shen *et al.*, 2010). 1 V sample showed the greatest ZnO nanorod crystallinity arrangement since it had the least emissions at the 50–450 nm region (UV region) but small emissions at the 600-700 nm region (orange-red region) indicated small intrinsic defects which was attributed to the presence of a small excess oxygen such as oxygen interstitial (Djurišić *et al.*, 2007). This result is supported by EDX which shows a high atomic percentage of oxygen at 49.7% [Figure 4.17]. On the other hand, the sample 2 V showed combinations of more than one defects. Based on available literature, this could be a combination of an oxygen vacancy and zinc interstitial,  $V_oZn_i$  (Alvi, 2011). The origin of green emissions normally came from oxygen based-defects (Alvi, 2011; Kröger & Vink, 1954; Studenikin *et al.*, 1998; Yamauchi *et al.*, 2004) and a combination of both defects, oxygen vacancy and zinc interstitial defect, produced broad peak which covers the green, yellow, and orange region [Figure 4.17] (Alvi, 2011; Janotti & Van de Walle, 2007). EDX proved that the % imbalance occurred in the 2 V sample; the atomic percentage of oxygen (48.3 at %) was lower than that of zinc (51.7 at %). Nevertheless, a few researchers proposed that high volumes of  $Zn(OH)_2$  could also produce the broad green, yellow and orange region (Djurišić *et al.*, 2007; Zhou *et al.*, 2002). In this case, insufficient annealing could be one of the reasons. A second reason would be the rate of field-assisted deposition was higher compared to the rate of dehydration (formation of ZnO). It therefore produced a high volume of  $Zn(OH)_2$  on the nanorod surface. This proposed reason would need

further investigation for confirmation. The 3 V sample showed that the superlattice performance at the 500-800 nm region for ZnO indicated less defects but had very high free exciton recombination at the 350 – 450 nm region which showed poor crystallinity arrangements of ZnO. The 3 V sample results indicated that the dense structure was based on its morphology and was in the bulk ZnO as per the results of Raman analysis.

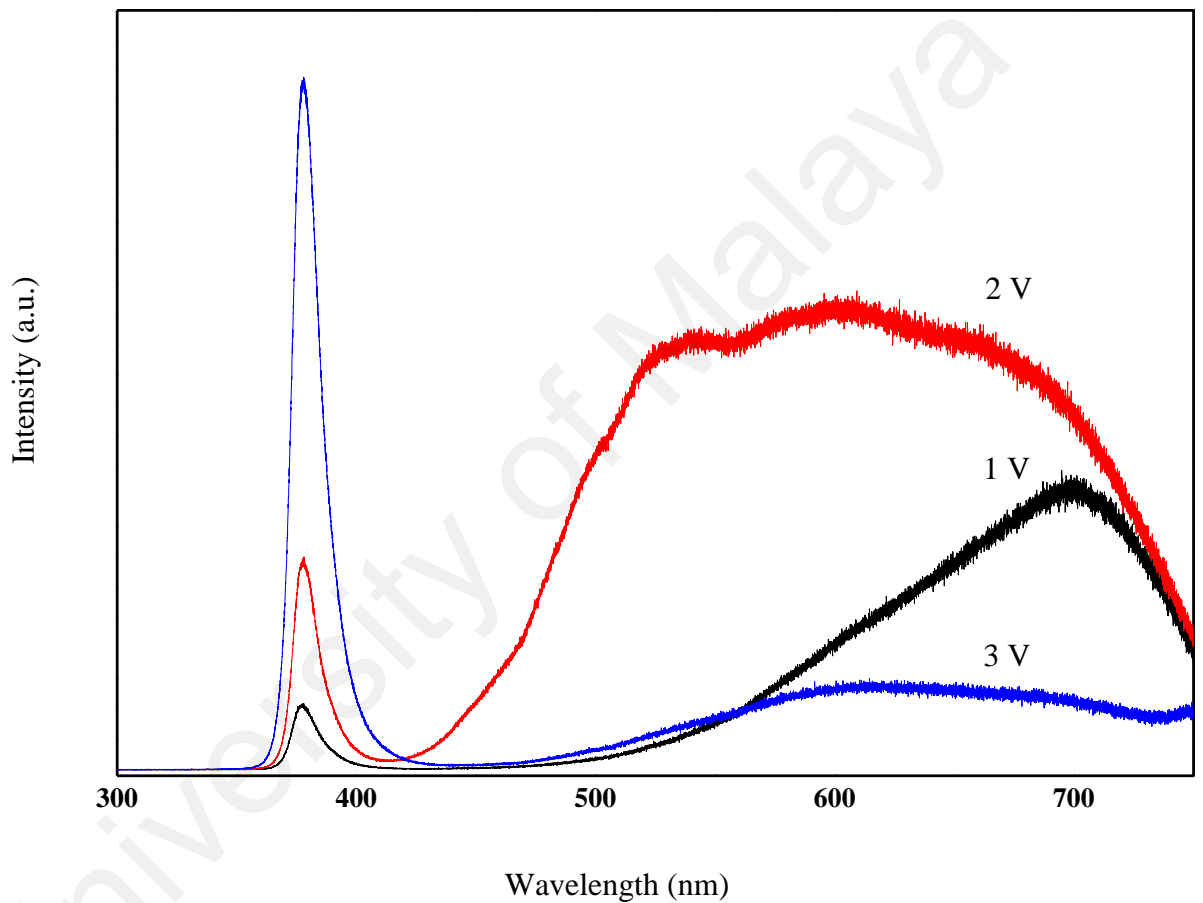


**Figure 4.17: PL spectra for sample 1V, 2V, and 3V (excitation:  $\lambda = 325$  nm)**

#### 4.1.5.4 Photoelectrochemical water splitting evaluation

ZnO with its excellent electronic properties and interfacial stability exhibited great photoelectrochemical response for hydrogen generation. The electrical simulation for water electrolysis (hydrogen generation) was studied by using photoelectrochemical response focusing on the photocurrent density analysis [Figure 4.18 & 4.19]. Water

splitting in excess of 90% occurred with applied potentials of -1 to 1 V (Stuart Licht *et al.*, 2001). This small current was needed to maintain the double-layer (surface charging and redox reaction) electron flow at the electrodes' surface [54]. A lot of literature has reported that the high active surface areas of photocatalysts generally exhibited excellent photocatalytic and photoelectrochemical responses due to the high percentage of produced and exposed atoms and ions on the catalyst surface. Therefore, a high volume of active sites was crucial for catalytic reactions (Lai & Sreekantan, 2011). Furthermore, the increments in rod lengths provided the fastest way for the charges to be transported along the longitudinal direction of a 1D single-crystalline nanomaterial (Crawford & Chawla, 2009; Lai & Sreekantan, 2011). In addition, it helped ionic species to have higher driving force in order to move through the barrier layer of the ZnO nanorod tip. The large active area referred to a high average aspect ratio [Table 4.7].

The 1V sample applied potential exhibited the highest photocurrent density,  $J_p$ , for UV ray (17.8 mA/cm<sup>2</sup>) [Figure 4.18] and visible light (12.94 mA/cm<sup>2</sup>) [Figure 4.19] as compared to 2V (UV ray,  $J_p = 11.78$  mA/cm<sup>2</sup> and visible light,  $J_p = 10.78$  mA/cm<sup>2</sup>) [Figure 4.18 and Figure 4.19]. Based on the above statements, the 1V applied potential exhibited the highest photocurrent density results due to it possessing the highest aspect ratio as compared to 2V [Table 4.7]. Meanwhile, the 3V applied potential exhibited an UV ray photocurrent density,  $J_p$ , of 6.83 mA/cm<sup>2</sup> and 5.74 mA/cm<sup>2</sup> for visible illumination [Figure 4.18 and Figure 4.19]. The dense porous structures (3V applied potential) inhibited the charge transfer competence via ZnO (anode) and it significantly decreased the collection of current density,  $J$ , and thus reduced the photocurrent density,  $J_p$ , which represented the photoresponse activity.

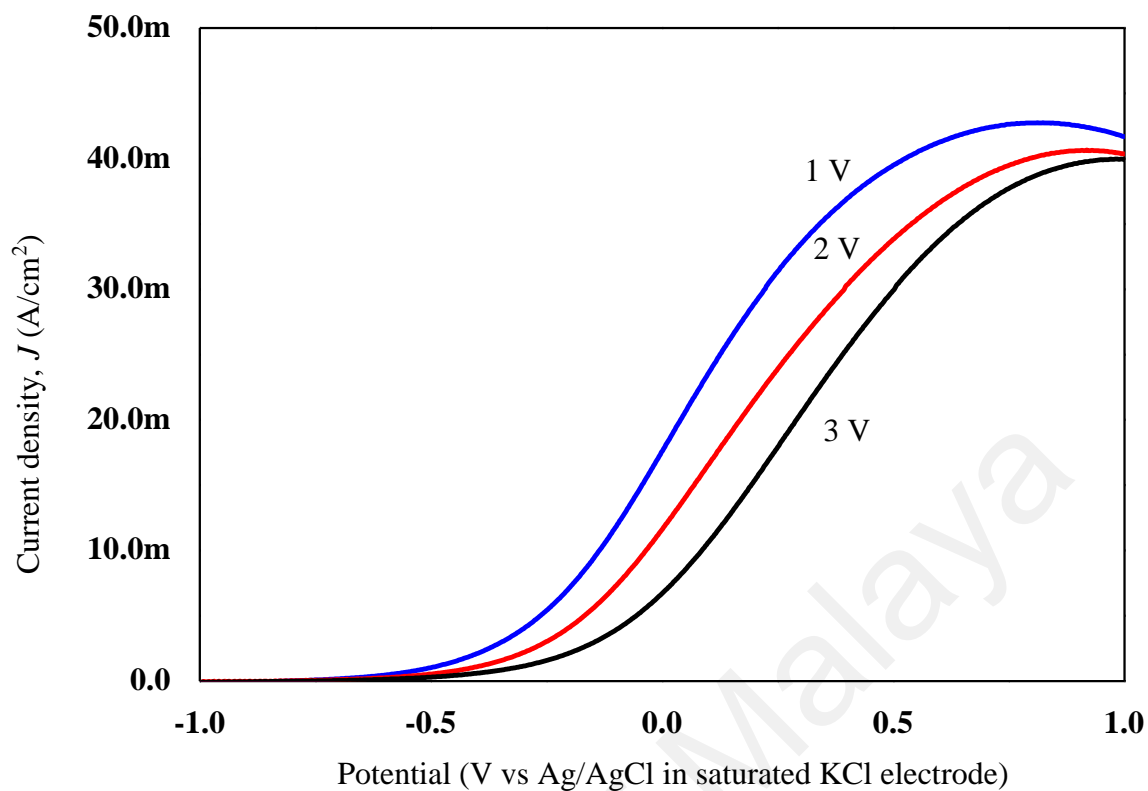


Figure 4.18: Photocurrent response for 1V, 2V, and 3V under UV ray.

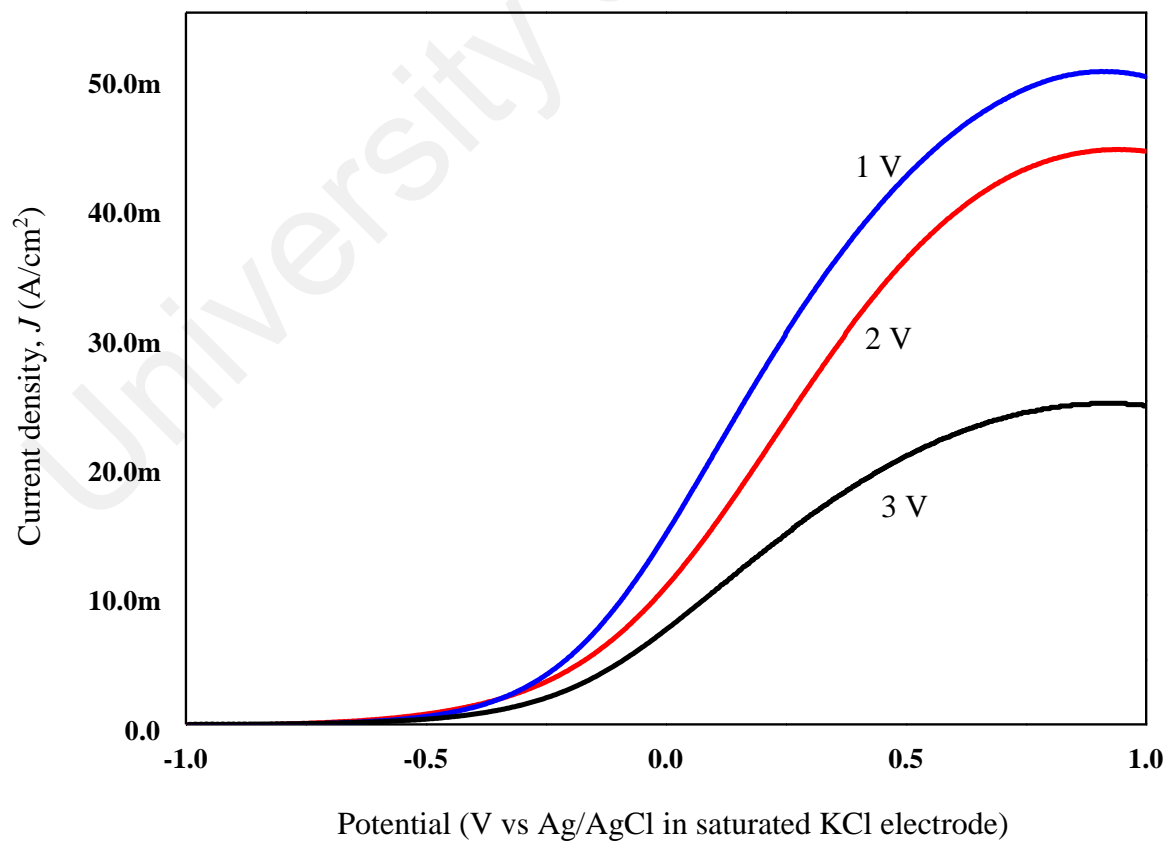


Figure 4.19: Photocurrent response for 1V, 2V, and 3V under visible illumination.

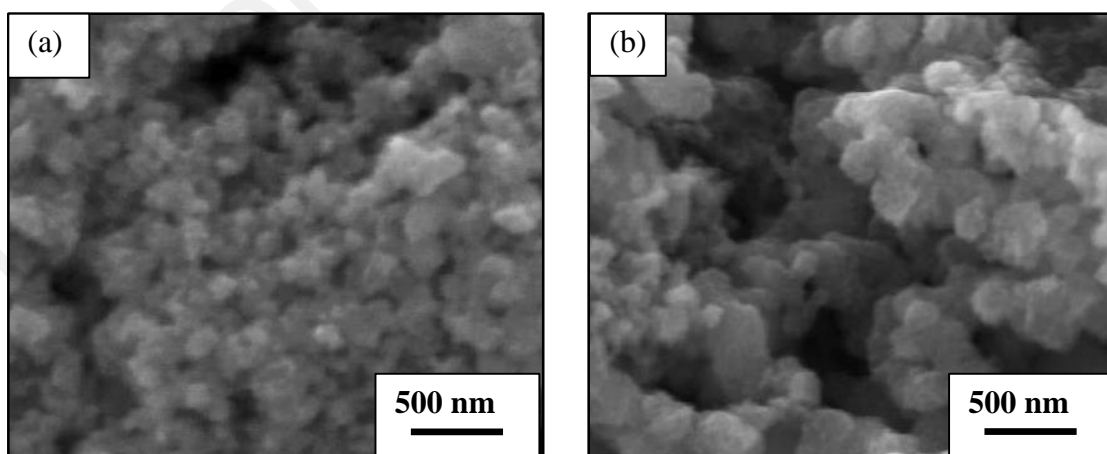
## 4.2 Formation of TiO<sub>2</sub> nanoparticles via precipitation-peptization technique

### 4.2.1 The influence of temperature towards the formation of TiO<sub>2</sub> nanoparticles

In this experiment, the aim of the study was to investigate the influence of the thermal effect on the crystallite size and phase of TiO<sub>2</sub>. The temperature, 60 °C of the chemical precipitation-peptization process is sufficient to form a small TiO<sub>2</sub> crystallite size of approximately 10.3 nm. In addition, the phases formed were the anatase and the brookite phases. However, anatase phase of TiO<sub>2</sub> was the main phase that appeared in all the samples.

#### 4.2.1.1 Morphological studies and elemental analysis by FESEM-EDX

FESEM showed that with an increase in the chemical precipitation-peptization temperature, the crystallite size of the TiO<sub>2</sub> decreased significantly. However, the morphology given below shows the agglomeration of TiO<sub>2</sub> [Figure 4.20]. The EDX analysis shows the compositional ratio of TiO<sub>2</sub> with an atomic ratio of Ti to O was approximately 1:2 [Table 4.8], indicating that only the elements Ti and O were present without any impurities.



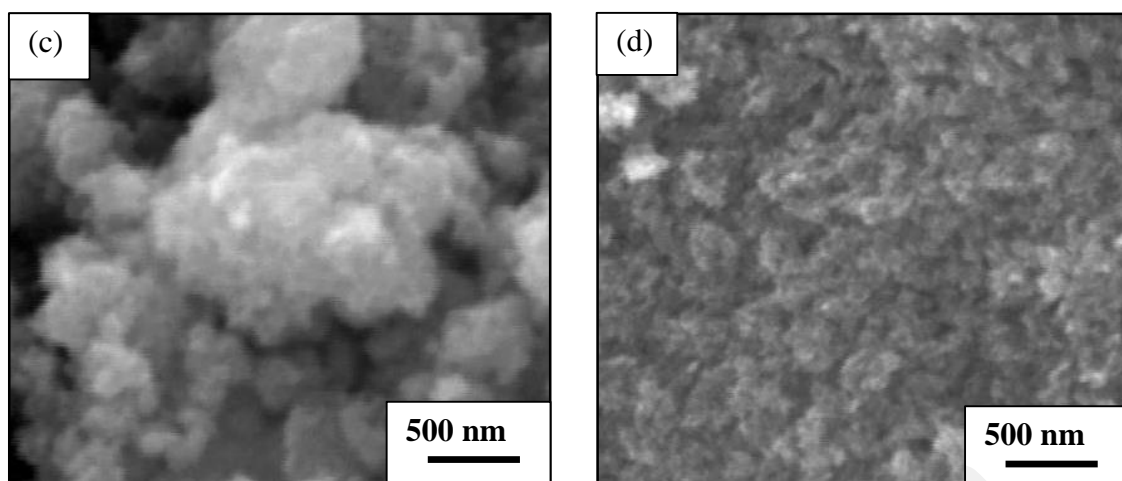


**Figure 4.20: FESEM micrographs of TiO<sub>2</sub> synthesized at different reaction temperatures, (a) Room temperature, (b) 40°C, (c) 60°C, and (d) 80°C.**

**Table 4.8: Compositional ratio of TiO<sub>2</sub> synthesized at different reaction temperatures: (a) room temperature, (b) 40°C, (c) 60°C, and (d) 80°C.**

Sample	Atomic percentage (at%)	
	Ti	O
Room temperature	28.93	71.07
40°C	28.19	71.81
60°C	34.57	65.43
80°C	32.99	67.02

#### 4.2.1.2 Phase structure analysis by XRD

In order to understand the effect of chemical precipitation-peptization temperature on the phase transition of TiO<sub>2</sub>, the different reaction temperatures were varied from room temperature to 40 °C, 60 °C and 80 °C [Figure 4.21]. XRD analysis was used to investigate the crystallization, crystallite size, and phase transition of TiO<sub>2</sub>. In addition, the variation in precipitation–peptization temperatures was studied to find the relevance of external forces (heat) towards the crystallinity of TiO<sub>2</sub> particle size. Based on the experimental results, it was found that a high temperature of 60 °C during the chemical precipitation-

peptization process is enough to form small TiO<sub>2</sub> particles of approximately 10.3 nm [Table 4.9]. Temperature influenced nucleation and crystal growth occurred by manipulating the solubility and supersaturation of the solution. An increase in temperature produced a higher solubility and a higher supersaturation index which led to a small particle size. Besides, temperature was shown to affect the quantity, size, and quality of the crystals. Diffusion rates were less and equilibration occurred more slowly at low than at high temperatures. Crystallization may occur more slowly at a low temperature rather than a high temperature. In addition, such interactions may have an impact on crystal packing as well as the termination of crystal growth. Hence, temperature has a big impact nucleation, growth, packing, and termination (Giulietti *et al.*, 2001; Rohani *et al.*, 1990).

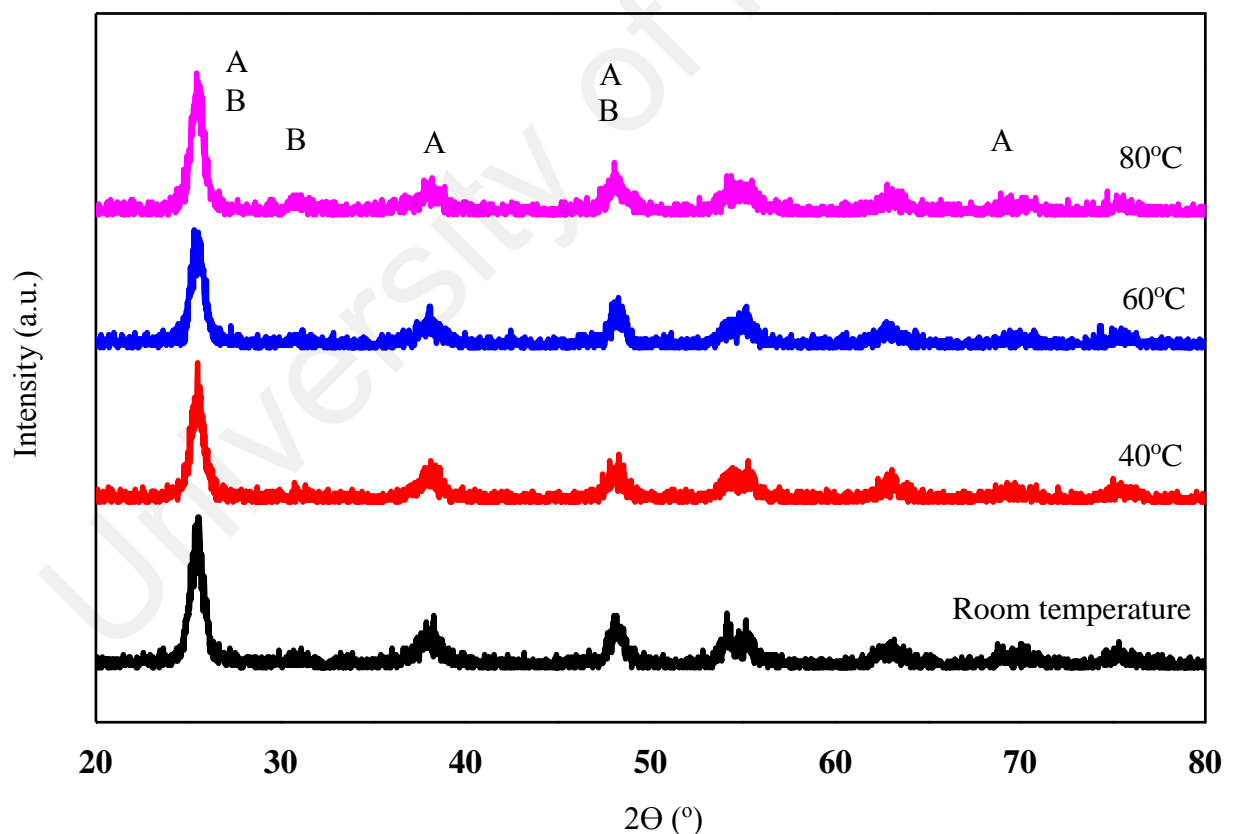


**Figure 4.21: XRD patterns of the TiO<sub>2</sub> synthesized at different reaction temperatures: room temperature, 40°C, 60°C, and 80°C. [A: Anatase, and B: Brookite]**

**Table 4.9: Diffraction peak position ( $^{\circ}$ ), FWHM, and crystallite size ( $\text{\AA}$ ) for  $\text{TiO}_2$  synthesized at different reaction temperatures.**

Sample	Peak position ( $^{\circ}$ )	FWHM	Crystallite size ( $\text{\AA}$ )
Room temperature	25.5	0.6298	129
40 $^{\circ}\text{C}$	25.6	0.6298	129
60 $^{\circ}\text{C}$	25.4	0.7872	103
80 $^{\circ}\text{C}$	25.6	0.7872	103

#### 4.2.2 The influence of stirring towards the formation of $\text{TiO}_2$ nanoparticles

To understand the stirring effect during the precipitation-peptization process on the phase transition of  $\text{TiO}_2$ , the stirring rate was varied from 60 rpm (revolutions per minute) to 125 rpm, 350 rpm, 700 rpm and 900 rpm. All speeds were fixed by the magnetic stirrer.

##### 4.2.2.1 Morphological studies and elemental analysis by FESEM-EDX

FESEM showed that with an increase in stirring there was a significant decrease in the crystallite size of  $\text{TiO}_2$  [Figure 4.22]. But, with a further increase in the stirring speed the crystallite size dropped. The morphology given below shows the agglomeration of  $\text{TiO}_2$ . Stirring affect the solubility of a solute. EDX analysis shows the compositional ratio of  $\text{TiO}_2$  with an atomic ratio of Ti to O was approximately 1:2, indicating that only the elements Ti and O were present without any impurities [Table 4.9]. The kinetic control (stirring rate) gave effect on the chemical composition ratio of  $\text{TiO}_2$  produced because stirring rate was directly proportional to evaporation rate. In this case, the evaporation of 2-propanol was occurred because the temperature of 80 $^{\circ}\text{C}$ ..Therefore, high intensity of O

ions left in the mixture (belongs to water content) and resulted with high composition of O element when increase in stirring rate.

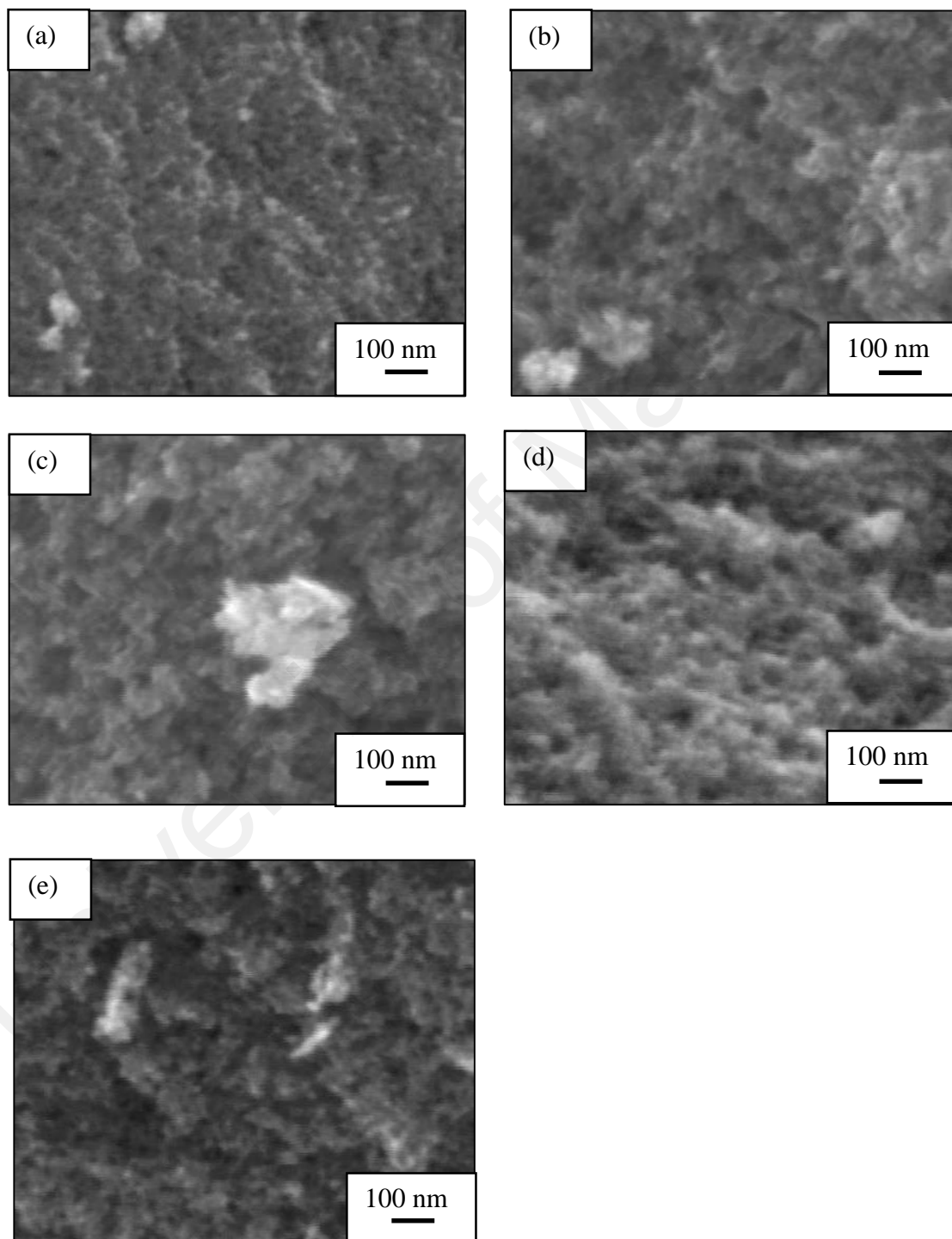


**Figure 4.22: FESEM images of TiO<sub>2</sub> nanoparticles at (a) 60 rpm, (b) 125 rpm, (c) 350 rpm, (d) 700 rpm, and (e) 900 rpm**

**Table 4.10: Compositional ratio of TiO<sub>2</sub> synthesized at different reaction temperatures: (a) 60 rpm, (b) 125 rpm, (c) 350 rpm, (d) 700 rpm, and (e) 900 rpm.**

Sample	Atomic percentage (at%)	
	Ti	O
60 rpm	29.4	70.6
125 rpm	33.8	66.2
350 rpm	33.0	67.0
700 rpm	17.2	82.8
900 rpm	40.1	59.9

#### 4.2.2.2 Phase structure analysis by XRD

XRD analysis was used to investigate the crystallization, crystallite size, and phase transition of TiO<sub>2</sub> [Figure 4.23]. In addition, the variation in stirring effect was studied to find the relevance of kinetic control towards the crystallinity of the TiO<sub>2</sub> particle size. Based on the experimental results, it was found that a stirring rate of 350 rpm is sufficient to form a small TiO<sub>2</sub> crystallite size of approximately 10.3 nm [Figure 4.23 (c) and Table 4.10]. 350 rpm is a sufficiently high speed for the formation of a sufficiently small crystallite size. The mechanical energy of stirring may cause particles collision and thus increased in surface area. Furthermore, stirring also controlled the seeding of TiO<sub>2</sub> nanoparticles (nucleation and crystal growth). The stirring rate is directly proportional to the evaporation rate (Erdođdu *et al.*, 2004; Gad, 2008; Lascelles *et al.*, 1998). In this case, 2-propanol was evaporated because the temperature was applied. The 2-propanol content influenced the solubility of the precipitation-peptization solution. A further increase in the stirring speed up to 700 rpm and 900 rpm produced a higher evaporation rate and led to a low solubility and supersaturation index. Thus, the crystal tended to grow rather than

nucleated a new crystal. Therefore, increase in stirring produced a bigger crystallite size. The results showed that the samples were in line with reference code ICDD 01-083-2243, which indicates the anatase phase. The Bragg reflection of the anatase phase was detected at  $2\theta$  values of  $25.3^\circ$  (101),  $37.8^\circ$  (004),  $48.1^\circ$  (200),  $53.9^\circ$  (105),  $62.8^\circ$  (204),  $68.8^\circ$  (116),  $70.4^\circ$  (220), and  $75.1^\circ$  (215) crystal planes.

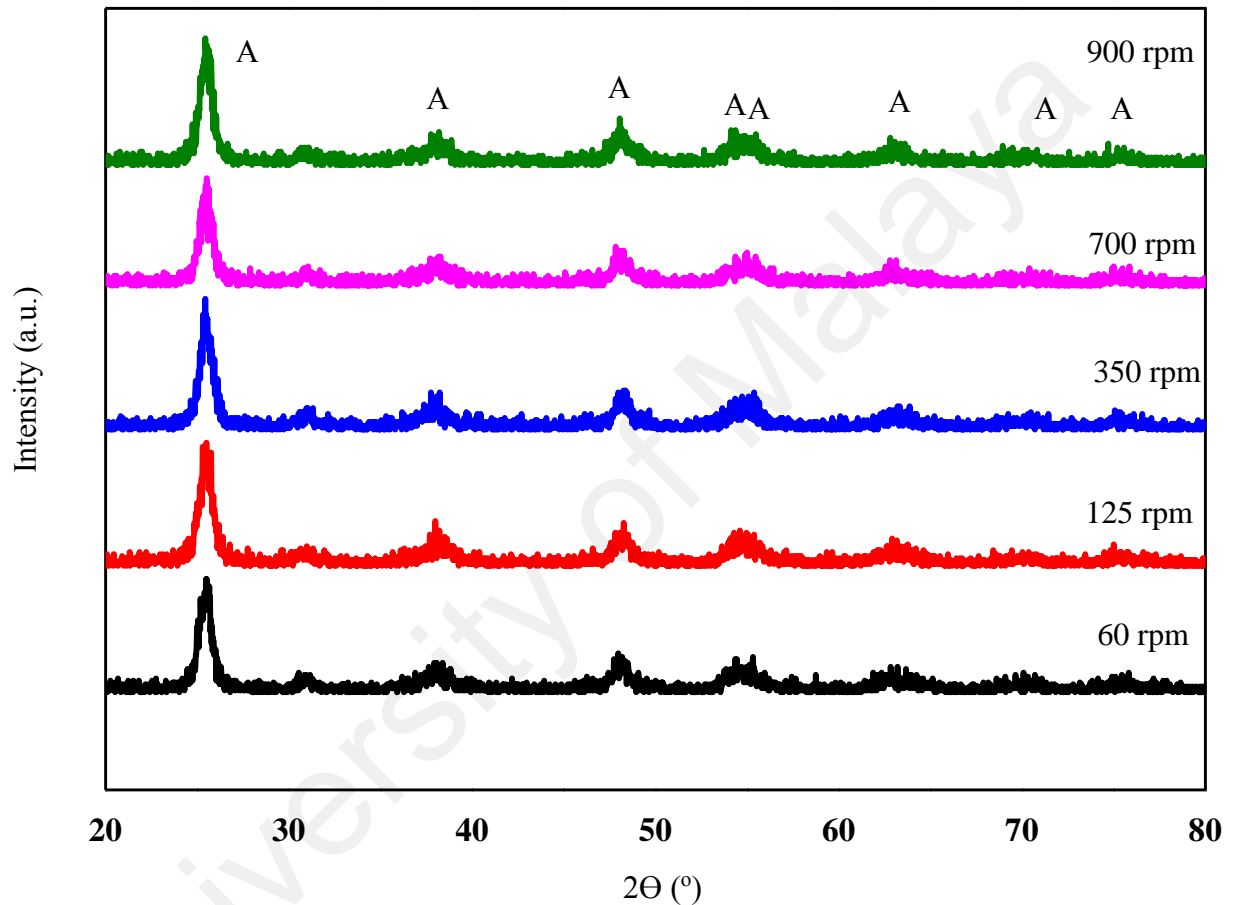


Figure 4.23: XRD patterns of the TiO<sub>2</sub> synthesized at different stirring speed 60 rpm, 125 rpm, 350 rpm, 700 rpm, and 900 rpm. [A: Anatase]

**Table 4.11: Diffraction peak position (°), FWHM, and crystallite size (Å) for TiO<sub>2</sub> synthesized at different stirring speed.**

Sample	Peak position (°)	FWHM	Crystallite size (Å)
60 rpm	25.6	0.3936	207
125 rpm	25.4	0.3936	207
350 rpm	25.6	0.7872	103
700 rpm	25.3	0.7085	115
900 rpm	25.6	0.6298	129

### 4.3 Hybrid TiO<sub>2</sub>-ZnO nanostructure film

Continuous efforts have been exerted to further improve the PEC water splitting performance by incorporating an optimum content of TiO<sub>2</sub> into ZnO nanorods using the dip-coating technique. It was found that long exposure to dip-coating did not produce the desired result. Based on aforementioned discussion, highly ordered ZnO nanorods film was synthesized via electrodeposition technique in an electrolyte 0.5 mM ZnCl<sub>2</sub>, 0.1 M KCl, 70 °C temperature, 1 V applied potential, low stirring process, and exposure time 60 min exhibited excellent PEC water splitting performance. A maximum  $j_p$  of 17.8 mA/cm<sup>2</sup> under UV ray and 12.94 mA/cm<sup>2</sup> under visible light were achieved. Therefore, in the following studies, ZnO nanorods films were synthesized in such condition mentioned above to study the effect of TiO<sub>2</sub> loaded on hybrid TiO<sub>2</sub>-ZnO nanostructure studies. The aim of this section is to improve the solar illumination absorption and further minimize the recombination loss of photo-induced charge carrier.

### 4.3.1 The influence of exposure time during dip-coating technique

Dip-coating is commonly used for the preparation of composite or heterogeneous catalysts. Watanabe *et al.* investigated the electrochemical performance of solid oxide fuel cells using long exposure time dip-coating with precious metal particles, e.g. Pt and Ru (Jiang, 2006; Hiroyuki Uchida *et al.*, 2002; H Uchida *et al.*, 2000; Hiroyula Uchida *et al.*, 1996; Hiroyuki Uchida *et al.*, 1998). It is agreed with Watanabe *et al.* that the long exposure time dip-coating technique produces heterogeneous catalysts with a porous structure, referring to the results given below.

#### 4.3.1.1 Morphological studies and elemental analysis by FESEM

The FESEM images showed that the long exposure time dip-coating technique produced a porous-like structure for the TiO<sub>2</sub>-ZnO film [Figure 4.24]. None of the samples showed ZnO nanorod structures. Two possibilities arise from the experiments; the TiO<sub>2</sub> solution etched away the ZnO nanorods or the TiO<sub>2</sub> nanoparticles fully covered the ZnO nanorods. The possibility of etching away the ZnO nanorods was proposed because the TiO<sub>2</sub> solution was previously prepared at a pH level of 3. This pH level of 3 was needed to prevent the agglomeration of the TiO<sub>2</sub> nanoparticles. Therefore, it might have etched away the ZnO nanorods. It can be clearly seen that 15 min of the exposure time dip-coating process produced a porous structure film. With a further increase the exposure time to 30 min, thick porous structure could be observed. Meanwhile, 60 min of the exposure time dip-coating process produced another transparent layer on top of the thick porous structure. The FESEM characterization could not show the edge as it was also fully covered by TiO<sub>2</sub> nanoparticles. Therefore, number of dipping cycles were studied to overcome this problem. The results are given in the following section.

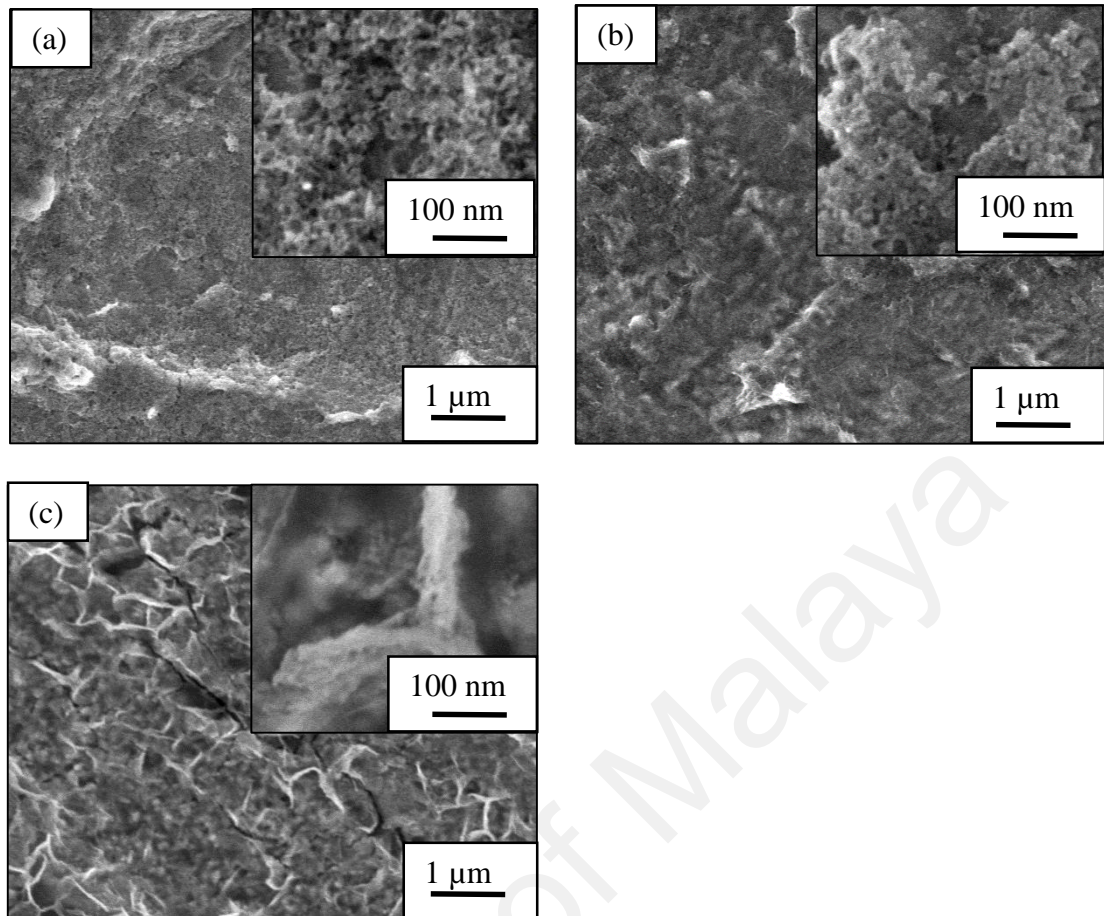


**Figure 4.24: FESEM for dip-coating of TiO<sub>2</sub> onto ZnO nanostructure at exposure time (a) 15 min, (b) 30 min, and (c) 60 min**

#### 4.3.1.2 Phase structure analysis by XRD

Figure 4.25 shows the XRD pattern for 15-minute wet-impregnation TiO<sub>2</sub>-ZnO, 30-minute wet-impregnation TiO<sub>2</sub>-ZnO, and 60-minute wet-impregnation TiO<sub>2</sub>-ZnO. From Figure 4.25 (a) - (c), peaks of TiO<sub>2</sub> and ZnO can be observed. TiO<sub>2</sub> is denoted by 37.2° (111), 43.2° (200), 62.7° (220), 75.2° (311), and 79.2° (222) (ICDD 01-077-2170). Meanwhile, ZnO is denoted by 31.7° (100), 34.3° (002), 36.2° (101), 47.5° (102), 56.5° (110), 62.8° (103), 67.9° (112), and 69.0° (201) (ICDD 01-080-0074). The quantification of 15-minute wet-impregnation TiO<sub>2</sub>-ZnO, 30-minute wet-impregnation TiO<sub>2</sub>-ZnO, and 60-minute wet-impregnation TiO<sub>2</sub>-ZnO were 32%-68%, 82%-18%, and 84%-16%, respectively. The quantification of TiO<sub>2</sub>-ZnO were measured using normal Rietveld Quantitative Analysis. Meanwhile, the crystallite size for all samples are showed approximately 108.5 nm [Table 4.12].

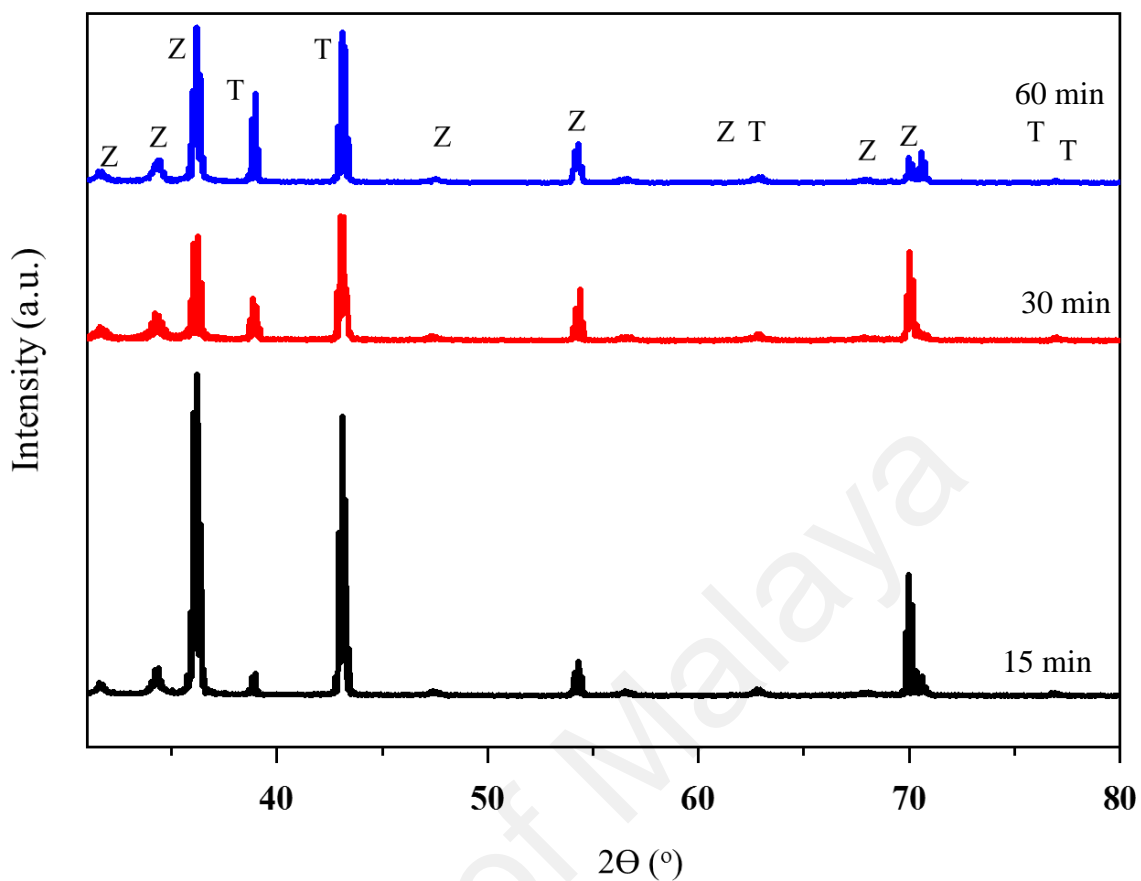


Figure 4.25: XRD patterns for exposure time dip-coating of TiO<sub>2</sub> nanoparticles onto ZnO nanostructure 15 min, 30 min, and 60 min. [Z: ZnO, and T: TiO<sub>2</sub>]

Table 4.12: Crystallite size (Å) for dip-coating TiO<sub>2</sub>-ZnO synthesized at different exposure time.

	Crystallite size (Å)	
	ZnO	TiO <sub>2</sub>
15 min	870	1085
30 min	1061	1086
60 min	1062	1086

### 4.3.2 The influence on the number of dipping cycles

The hybrid TiO<sub>2</sub>-ZnO film can benefit efficient excitonic charge separation and minimize recombination in the heterostructure coating. Moreover, the TiO<sub>2</sub> nanoparticles also acts as an antireflection layer that effectively enhances the light absorption efficiency. PEC water splitting fabricated from the hybrid TiO<sub>2</sub>-ZnO film demonstrated a greatly improved PEC performance under UV ray and visible light as compared to the pure ZnO nanostructures film.

#### 4.3.2.1 Morphological studies and elemental analysis by FESEM-EDX and HRTEM

Each additional dip-coating cycle produced a small change in TiO<sub>2</sub>-ZnO thin film morphology [Figure 4.26]. However, all samples were very nearly vertically aligned and were of the average length, diameter and aspect ratio shown in Table 4.14. In addition, Figure 4.26 (a) – (d) shows a decrease in the length and diameter with the increase in dip-coating cycles. This result is attributed to the etching phenomenon by the TiO<sub>2</sub> solution which was in an acidic (pH 1-3) solution to maintain the dispersion of TiO<sub>2</sub>. From the HRTEM result, there was a boundary that split the two different materials [Figure 4.26 (e)]. This was confirmed by the lattice spacing by each material: 0.27 nm (TiO<sub>2</sub>) and 0.33 nm (ZnO). Also, the existence of the two different materials could be recognized by the arrangement of atoms in different directions.

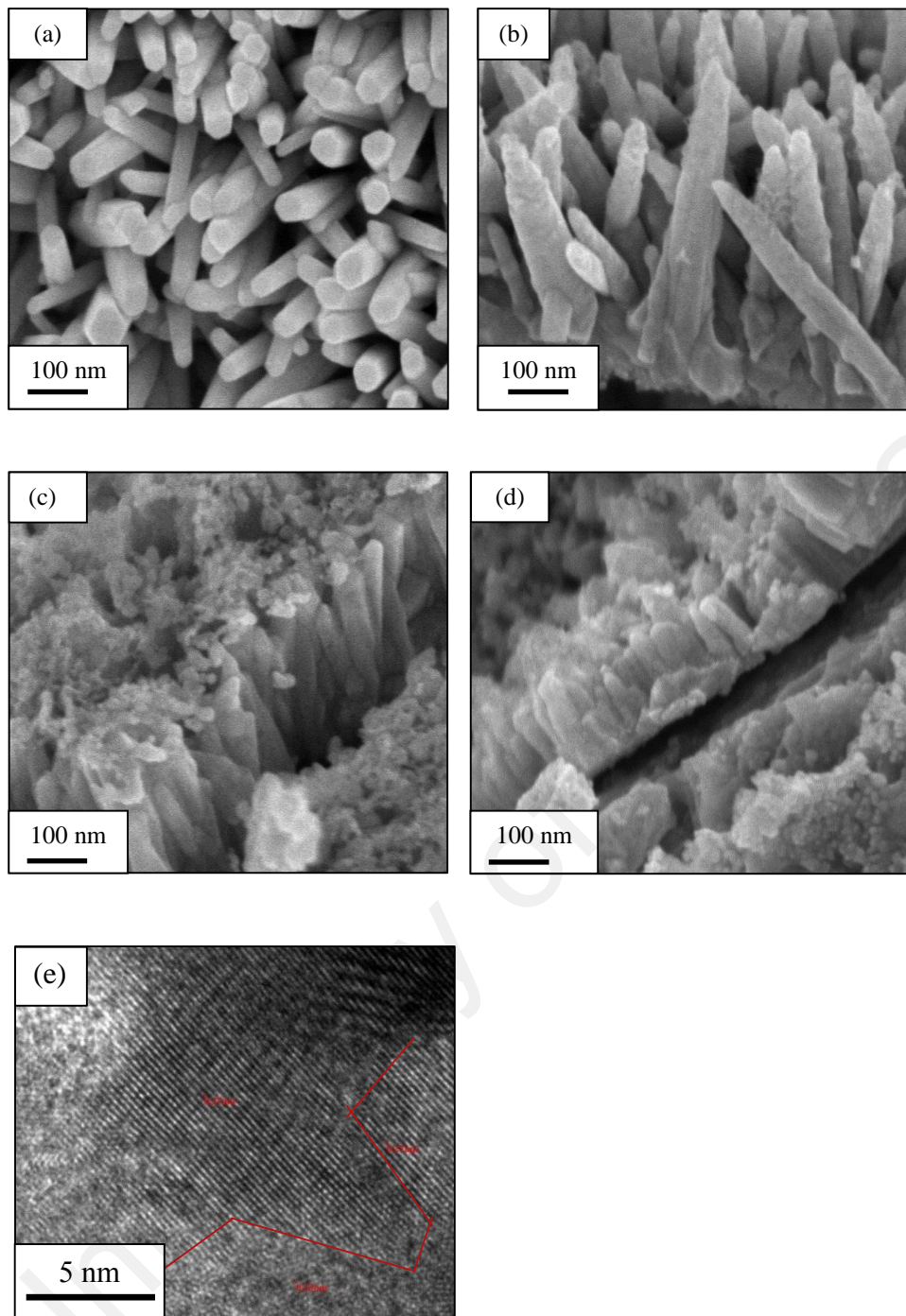


**Figure 4.26: FESEM images with 100k magnification (a) ZnO nanostructure, (b) 0.25 at% TiO<sub>2</sub>-ZnO, (c) 0.50 at% TiO<sub>2</sub>-ZnO, and (d) 1.0 at% TiO<sub>2</sub>-ZnO and HRTEM image for TiO<sub>2</sub>-ZnO.**

**Table 4.13: Average compositional ratio for pure ZnO, 0.25 at% TiO<sub>2</sub>-ZnO, 0.50 at% TiO<sub>2</sub>-ZnO, and 1.0 at% TiO<sub>2</sub>-ZnO using EDX spectroscopy analysis.**

	Atomic percentage (at%)		
	Zinc	Oxygen	Titanium
<b>Pure ZnO</b>	44.54	55.46	<i>Nil.</i>
<b>1 cycle dip-coating TiO<sub>2</sub>-ZnO</b>	52.95	46.80	0.25
<b>2 cycle dip-coating TiO<sub>2</sub>-ZnO</b>	53.25	46.29	0.46
<b>3 cycle dip-coating TiO<sub>2</sub>-ZnO</b>	61.96	36.98	1.06

**Table 4.14: The average value of length, diameter and aspect ratio for pure ZnO, 0.25 at% TiO<sub>2</sub>-ZnO, 0.50 at% TiO<sub>2</sub>-ZnO, and 1.0 at% TiO<sub>2</sub>-ZnO.**

	Length (nm)	Diameter (nm)	Aspect ratio
<b>Pure ZnO</b>	~500 ± 103	~75 ± 15	6.7
<b>0.25 at% TiO<sub>2</sub>-ZnO</b>	~500 ± 98	~65 ± 11	7.7
<b>0.50 at% TiO<sub>2</sub>-ZnO</b>	~350 ± 67	~60 ± 21	5.8
<b>1.0 at% TiO<sub>2</sub>-ZnO</b>	~350 ± 103	~55 ± 16	6.4

#### 4.3.2.2 Phase structure analysis by XRD and Raman Scattering

Figure 4.27 shows the XRD pattern for 0.25 at% TiO<sub>2</sub>-ZnO, 0.5 at% TiO<sub>2</sub>-ZnO, 1.0 at% TiO<sub>2</sub>-ZnO and pure ZnO thin film. In Figure 4.27 (a) – (c), peaks of TiO<sub>2</sub> and ZnO could be observed. TiO<sub>2</sub> is denoted by 25.4°, 37.3°, 38.2°, 38.9°, 48.3°, 54.0°, 55.5°, and 63.2° (ICDD 01-073-1764). Meanwhile, ZnO is denoted by 31.9°, 34.6°, 36.2°, 47.4°,

56.4°, 62.9°, 68.1°, and 69.0° (ICDD 01-080-0074). Increasing the dip-coating cycle produced a lower intensity of FWHM of ZnO. This is because the TiO<sub>2</sub> volume started to increase. Moreover, the hybrid TiO<sub>2</sub>-ZnO thin film showed that no other element existed. The quantification 0.25 at% TiO<sub>2</sub>-ZnO, 0.5 at% TiO<sub>2</sub>-ZnO, and 1.0 at% TiO<sub>2</sub>-ZnO were noted as 75%-25%, 66%-34%, and 67%-33%, respectively. Meanwhile, pure ZnO can be indexed to wurtzite ZnO (ICDD 00-036-1451) without any impurity peaks [Figure 4.27 (d)]. Good crystallinity can be seen from the sharp peaks of ZnO prior to the dip-coating process for TiO<sub>2</sub>- ZnO.

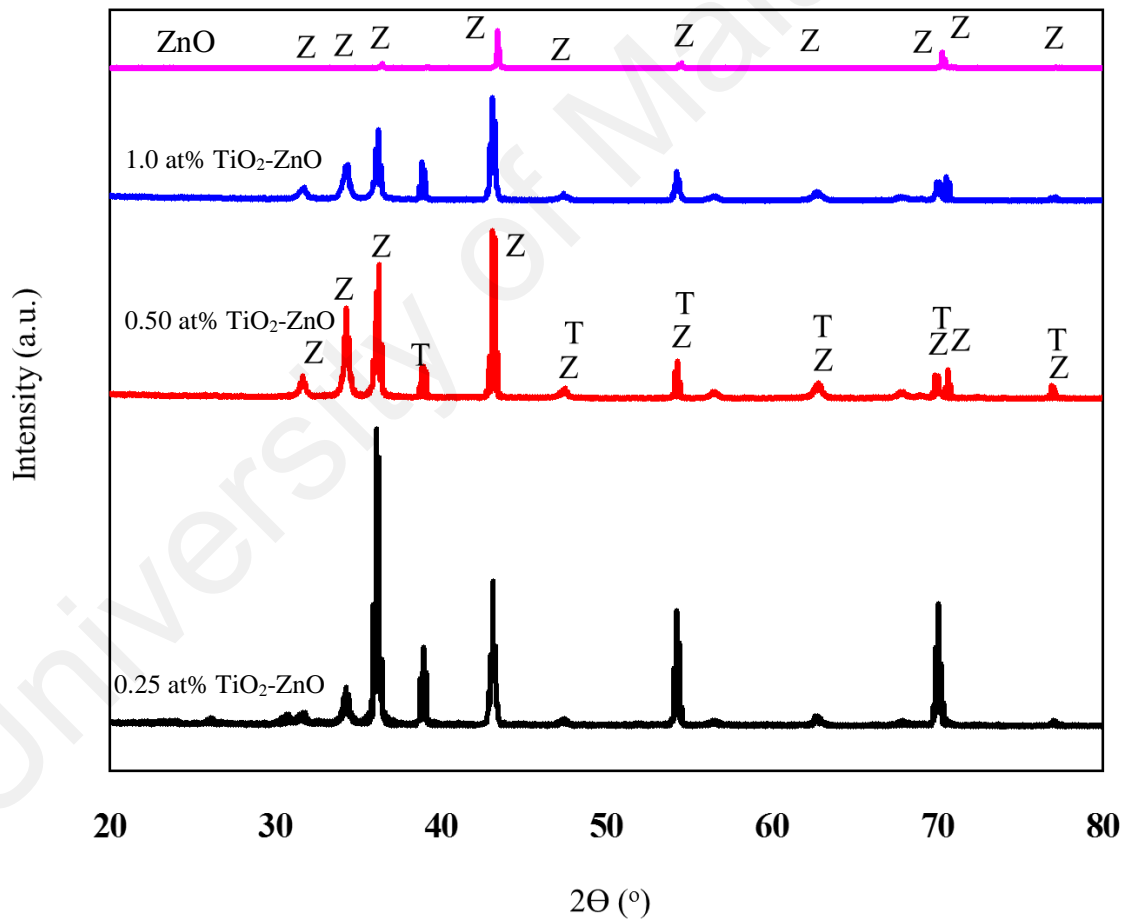


**Figure 4.27: XRD pattern of 0.25 at% TiO<sub>2</sub>-ZnO, 0.50 at% TiO<sub>2</sub>-ZnO, 1.0 at% TiO<sub>2</sub>-ZnO and pure ZnO. [Z: ZnO and T: TiO<sub>2</sub>].**

Raman analysis was used to determine and understand the structural changes of ZnO and TiO<sub>2</sub> upon increasing the dip-coating cycle. However, Figure 4.28 shows no signature of the TiO<sub>2</sub> substance, with the Raman peaks mainly belonging to wurtzite ZnO. This might be due to the small amount of TiO<sub>2</sub> and to the scattering spectra that could be negligible as they were too small to be seen. These thin films were still weak in pure stoichiometric ZnO due to the dominance of the E<sub>1</sub> (LO) and A<sub>1</sub> (LO) modes (570-585 cm<sup>-1</sup>) for all samples, compared to the E<sub>2</sub> (high) mode 438 cm<sup>-1</sup>. This can be explained by the oxygen atom deficiency that was represented by these two modes (E<sub>1</sub> (LO) and A<sub>1</sub> (LO) mode (570-585 cm<sup>-1</sup>)) and with the existence of the Zn element from the Zn substrate (Exarhos & Sharma, 1995; Schumm *et al.*, 2007). Increasing the dip-coating cycle produced a lower E<sub>2</sub> (high) mode, which was attributed to the depreciation of the perfect crystal structure wurtzite ZnO. Meanwhile, as mentioned above, there was a dominance of the E<sub>1</sub> (LO) and A<sub>1</sub> (LO) mode (570-585 cm<sup>-1</sup>) for all samples compared to the E<sub>2</sub> (high) mode 438 cm<sup>-1</sup>. But, an increase in the dip-coating cycle produced a slight depreciation in the E<sub>1</sub> (LO) and A<sub>1</sub> (LO) modes. This may support evidence on the role of TiO<sub>2</sub> as an antireflective layer, and by increasing the dip-coating cycle, it may have increased the absorption of light, producing slightly lower Raman spectra. The small shift of spectra was probably due to the optical phonon confinement, a defect or impurity in the nanocrystal, laser irradiation heating, or the tensile strain effect (Alim *et al.*, 2005; R. Zhang *et al.*, 2009).

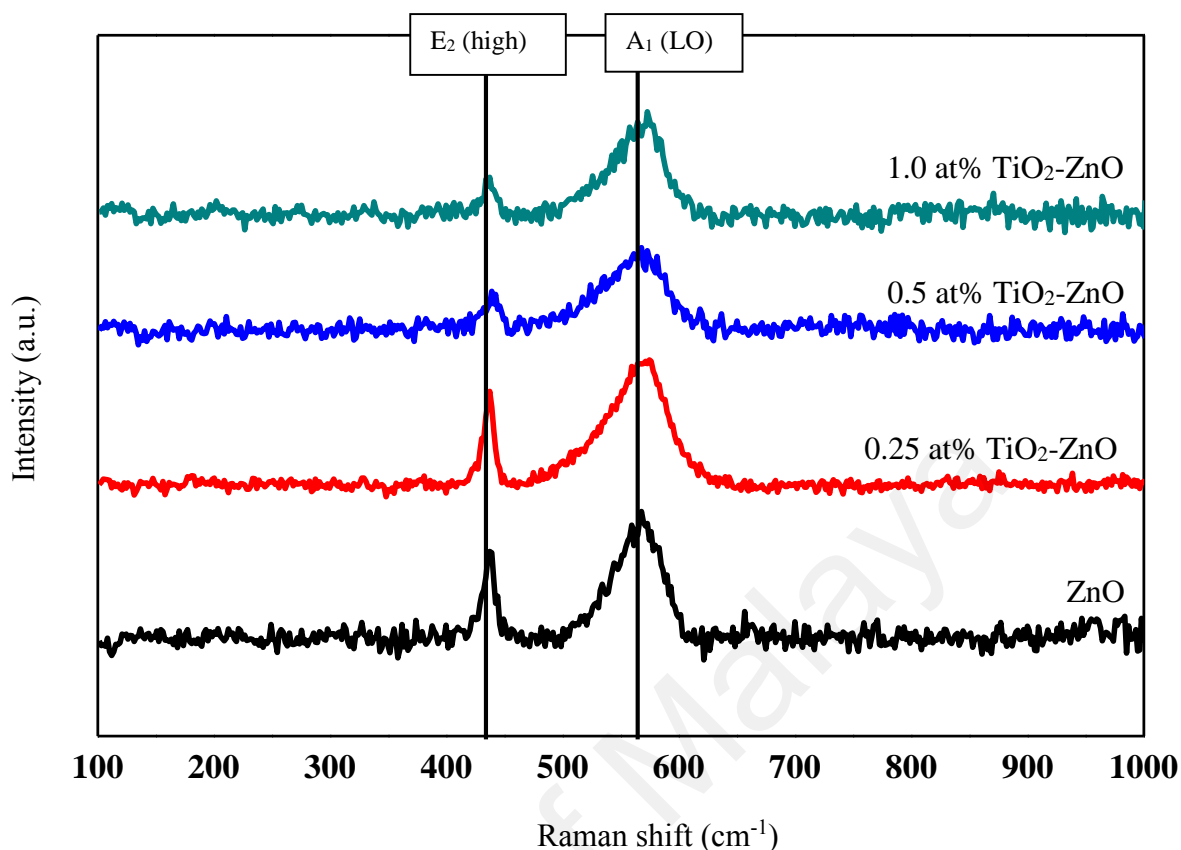


**Figure 4.28: Raman scattering for ZnO nanostructure, 0.25 at% TiO<sub>2</sub>-ZnO, 0.5 at% TiO<sub>2</sub>-ZnO, and 1.0 at% TiO<sub>2</sub>-ZnO.**

#### 4.3.2.3 Chemical state analysis

For a further understanding of the elements and chemical interactions of the TiO<sub>2</sub>-ZnO interface, an XPS analysis was carried out for samples ZnO, 0.25 at% TiO<sub>2</sub>-ZnO and 1.0 at% TiO<sub>2</sub>-ZnO. XPS survey spectra confirmed that TiO<sub>2</sub> was successfully deposited onto the ZnO film. The elements Zn, Ti, C, and O existed in the TiO<sub>2</sub>-ZnO nanostructures [Figure 4.29]. The XPS results show that the Ti peaks increased with the dip-coating cycle. This is in accordance with the EDX results. One peak of Zn2p<sub>3/2</sub> was detected at binding energy 1021 ± 10 eV [Figure 4.30] and this matched the CAS registry no. 1314-13-2, referring to National Institute of Standards and Technology (NIST), an agency of the U.S. Department of Commerce (Naumkin *et al.*, 2012). From this, the sample with the formula ZnO is classed as a catalyst and an oxide with the line designation 2p<sub>3/2</sub> and a related-binding energy of 1021 ± 1.0 eV (Nefedov *et al.*, 1977). With the increase in the dip-coating cycle, the binding energy of Zn2p<sub>3/2</sub> shifted to a lower

binding energy [Figure 4.30 (a) and (b)]. The difference in binding energies is attributed to the change of charge transfer from  $\text{Zn}^{2+}$  to  $\text{O}^{2-}$ . In addition, previous research has shown that oxygen deficiency is the main factor in the decrease in binding energy (Hosseini *et al.*, 2015; Sahu *et al.*, 2012). From the EDX results, it was confirmed that O at% is reduced with the increase in the dip-coating cycle [Table 4.13].

It can be clearly seen that all O1s curves were asymmetric; therefore, both lines were fitted with two Gaussian peaks (I and II) [Figure 4.31 (c)]. Peak I of O1s was located in the lower binding energy, as compared to peak II. Peak I was assigned to  $\text{O}^{2-}$  ions of the Zn-O bonding at the crystal lattice (J. Zheng *et al.*, 2011). Al-Gaashani *et al.* proposed that structural defects existing among crystals produced hydroxyl group adsorption, which is indicated by peak II (Al-Gaashani *et al.*, 2013). These hydroxyl groups helped to prevent the recombination of electron-holes (Chong *et al.*, 2010; Hosseini *et al.*, 2015). In addition, Zn2p and O1s binding energies were shifted to lower binding energies after the coating process. Another reason for the shift to lower binding energies for Zn2p and O1s is the reduction in the oxygen vacancy. The XPS results show a decrease in the Zn/O ratio for  $\text{TiO}_2$ -coated ZnO as compared to the pure samples. This confirmed a reduction in the density of the oxygen defect (Hosseini *et al.*, 2015; Y. Zheng *et al.*, 2007).

The XPS spectra for Ti2p showed binding energies at 458.7 and 464.6 eV, demonstrating  $\text{Ti}2\text{p}_{3/2}$  and  $\text{Ti}2\text{p}_{1/2}$  (Casaletto *et al.*, 2006; Y.-W. Chen *et al.*, 2012; Moreau & Bond, 2007; Moulder *et al.*, 1995; Soares *et al.*, 2003; Tabakova *et al.*, 2000). The Ti2p spectra indicated that the Ti in  $\text{TiO}_2$ -ZnO were all in a  $\text{Ti}^{4+}$  state, but the heterogeneous environments of  $\text{Ti}^{4+}$  resulted in the broadening of the  $\text{Ti}^{4+}$  2p in the XPS spectra. There is a slight decrease in the intensity of the  $\text{Ti}2\text{p}_{3/2}$  peak and a broadening of the  $\text{Ti}2\text{p}_{1/2}$  with an increase in the Ti/Zn ratio from 1.0 at% to 0.25 at% [Figure 4.32]. This indicated

a decrease in the  $\text{Ti}^{4+}$  state and the heterogeneous environment due to the mixed oxides.

Summary of XPS spectra as in Table 4.15.

University of Malaya

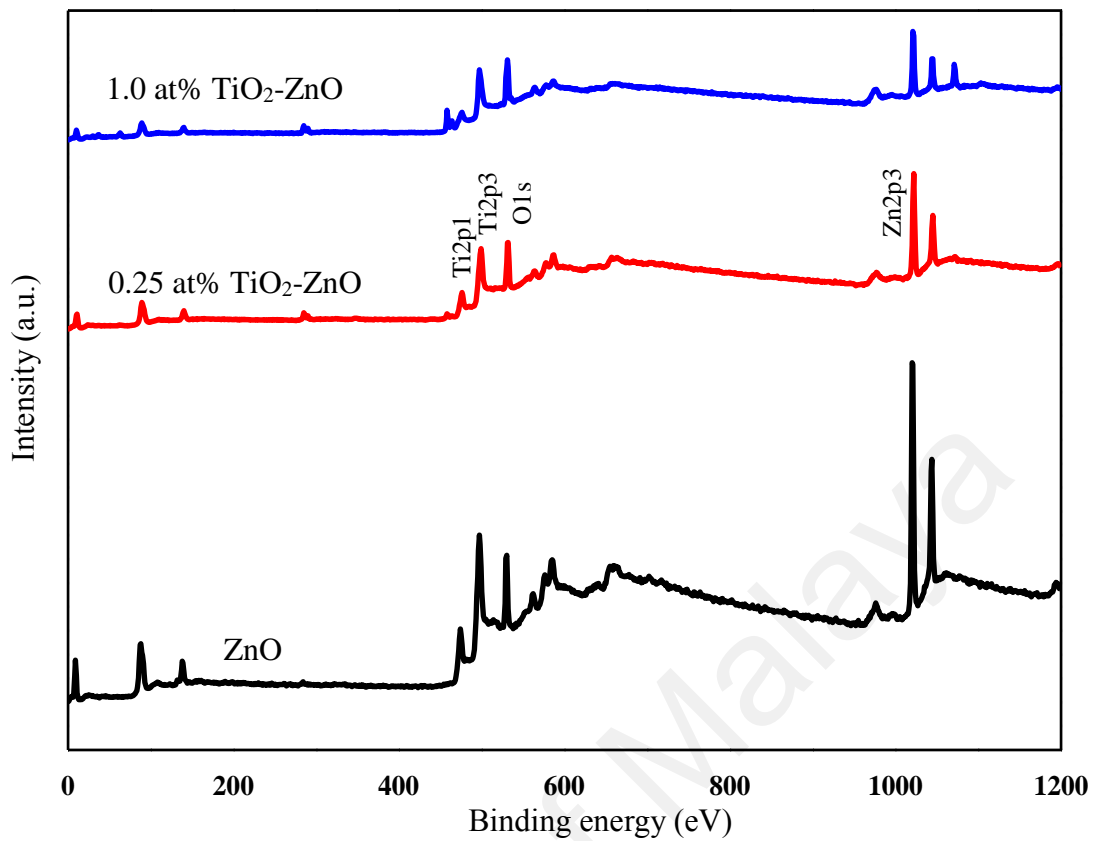


Figure 4.29: Full XPS survey spectra of ZnO, 0.25 at% TiO<sub>2</sub>-ZnO, and 1.0 at% TiO<sub>2</sub>-ZnO

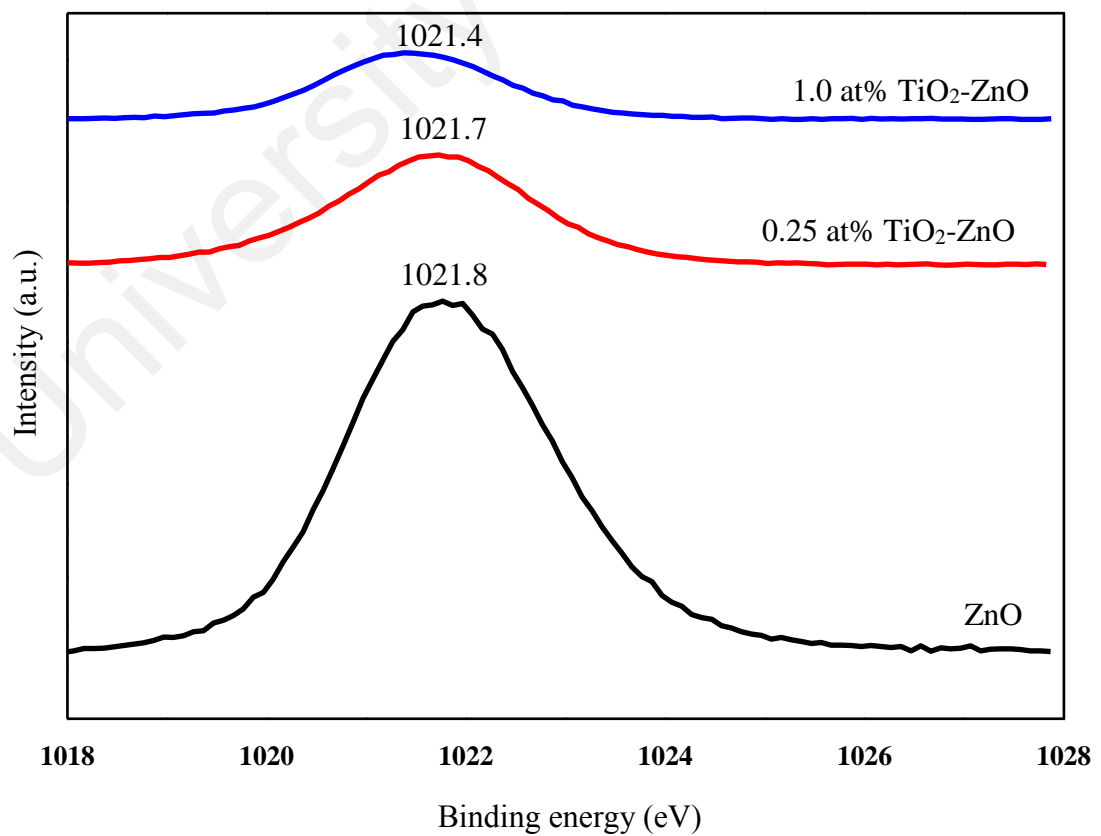
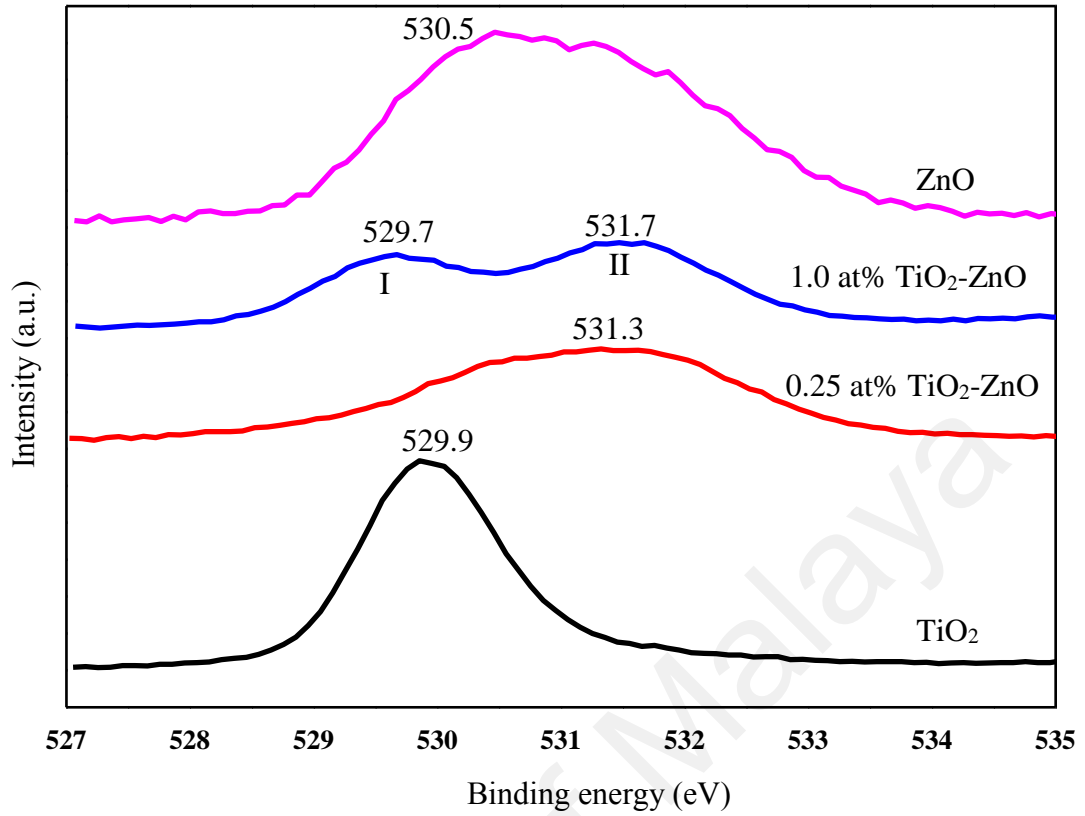
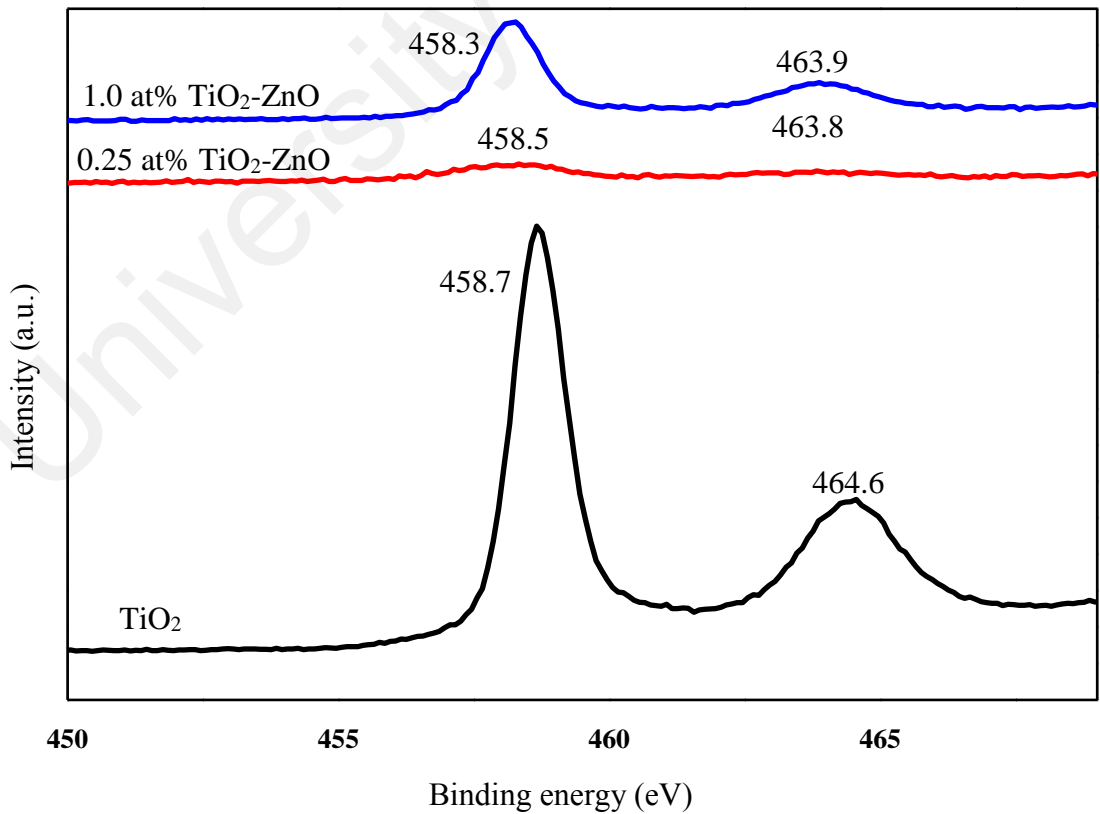


Figure 4.30: XPS spectra of Zn2p for ZnO, 0.25 at% TiO<sub>2</sub>-ZnO, and 1.0 at% TiO<sub>2</sub>-ZnO.



**Figure 4.31: XPS spectra of O1s for TiO<sub>2</sub>, 0.25 at% TiO<sub>2</sub>-ZnO, 1.0 at% TiO<sub>2</sub>-ZnO, and ZnO.**



**Figure 4.32: XPS spectra Ti2p for TiO<sub>2</sub>, 0.25 at% TiO<sub>2</sub>-ZnO, and 1.0 at% TiO<sub>2</sub>-ZnO.**

**Table 4.15: Summary of XPS spectra for Zn2p<sub>3/2</sub>, Ti2p<sub>1/2</sub>, Ti2p<sub>3/2</sub>, and O1s for samples TiO<sub>2</sub>, 0.25 at% TiO<sub>2</sub>-ZnO, 1.0 at% TiO<sub>2</sub>-ZnO, and ZnO.**

Sample	Zn2p <sub>3/2</sub>	Ti2p <sub>1/2</sub>	Ti2p <sub>3/2</sub>	O1s
TiO <sub>2</sub>	-	464.6	458.7	529.9
0.25 at% TiO <sub>2</sub> -ZnO	1021.7	463.8	458.5	531.3
1.0 at% TiO <sub>2</sub> -ZnO	1021.4	463.9	458.3	529.7, 531.7
ZnO	1021.8	-	-	530.5

#### 4.3.2.4 Photoluminescence behavior by PL

The photoluminescence study for the hybrid TiO<sub>2</sub>-ZnO film mainly showed some defects, for instance zinc vacancies, zinc interstitials, oxygen vacancies, oxygen interstitials, and oxygen anti-sites. The ZnO PL spectra showed the UV emission band centred at 380 nm (determined by the exciton recombination process), and the broad visible emission band (determined by the intrinsic defects) [Figure 4.33] (Chandrinou *et al.*, 2009). The PL intensity kept decreasing with the increasing TiO<sub>2</sub>-ZnO cycles. This is because of the increase in the TiO<sub>2</sub> layer and is attributed to the charge-separation effect of the type-II band alignment of ZnO and TiO<sub>2</sub> (heterojunction studies). (Shao *et al.*, 2014). The photogenerated electrons and holes at the staggered band offset are separated and connected mainly in the TiO<sub>2</sub> and ZnO, respectively, to achieve the excitonic charge separation state. The efficient charge separation decreases the recombination rate of electrons and holes and, at the same time, weakens the PL intensity of the hybrid TiO<sub>2</sub>-ZnO film (Greene *et al.*, 2007; Panigrahi & Basak, 2011; Shao *et al.*, 2014). In addition, the refractive index of anatase TiO<sub>2</sub> (~2.55) is higher than that of wurtzite ZnO (~1.99). Therefore, TiO<sub>2</sub> acts as antireflection layer and with the increasing TiO<sub>2</sub> cycle it may

increase the absorption of light. Efficient light absorption may also weaken the PL intensity.

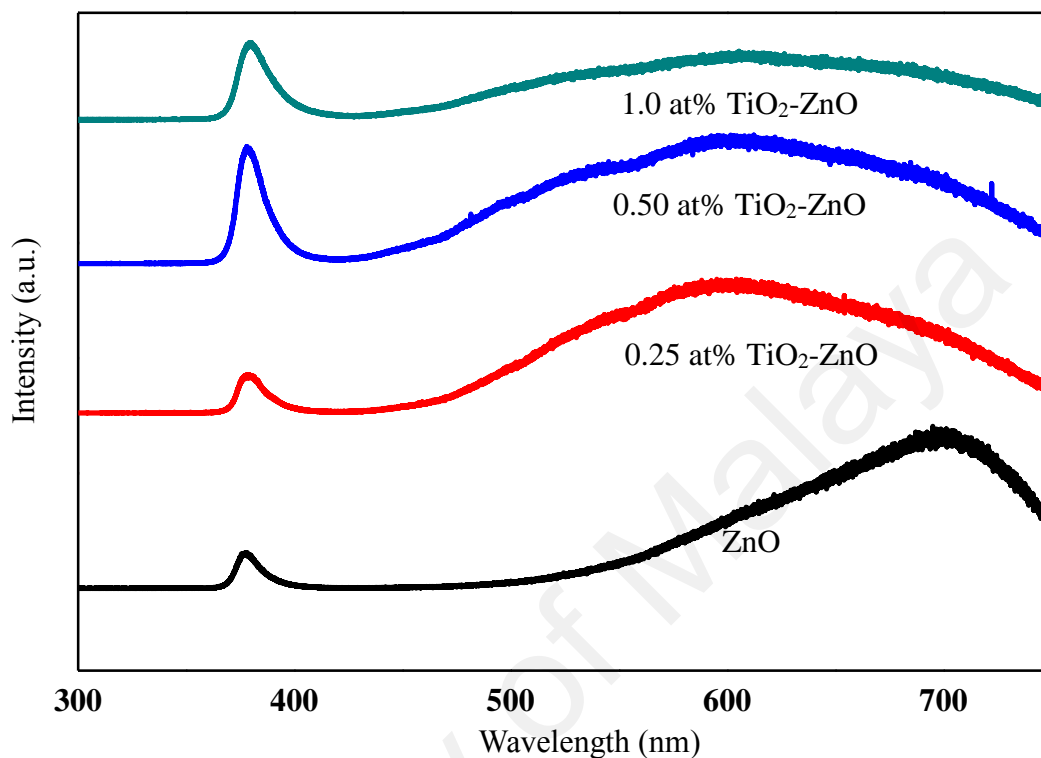


**Figure 4.33:** PL spectra for sample (a) pure ZnO, (b) 0.25 at% TiO<sub>2</sub>-ZnO, (c) 0.50 at% TiO<sub>2</sub>-ZnO, and (d) 1.0 at% TiO<sub>2</sub>-ZnO (excitation:  $\lambda = 325$  nm).

#### 4.3.2.5 Photoelectrochemical response and photoconversion efficiency

ZnO, with its excellent electronic properties and interfacial stability, exhibited a great PEC response for hydrogen generation. The electrical simulation for water electrolysis (hydrogen generation) has been studied using the PEC response, focusing on the current density analysis [Figure 4.34 and 4.35]. The photoconversion efficiency ( $\eta$ ), that is the light energy to chemical energy conversion efficiency, was subsequently calculated via Equation 3.3 and plotted in Figure 4.36 and 4.37 (Shankar *et al.*, 2007; Y. Sun *et al.*, 2011), whereby 0.25 at% TiO<sub>2</sub>-ZnO presented the highest photocurrent density and photoconversion efficiency, regardless of whether the PEC process occurred under UV ray or visible light [Figure 4.34 (b), 4.35 (b), 4.36 (b), and 4.37 (b)] as compared to the

sample of pure ZnO and samples with more than one cycle of the dip-coating process. Coating ZnO with TiO<sub>2</sub> produced a photocurrent density of 19.78 mA/cm<sup>2</sup>, as compared to pure ZnO 10.94 mA/cm<sup>2</sup> (UV ray) and 14.75 mA/cm<sup>2</sup> and with pure ZnO 9.06 mA/cm<sup>2</sup> (visible light). The enhancement in photocurrent density for the hybrid TiO<sub>2</sub>-ZnO film is due to the charge-separation effect that occurred at the type-II band alignment of ZnO and TiO<sub>2</sub>, as discussed earlier. Meanwhile, the increase in the dip-coating cycle produced a higher amount of TiO<sub>2</sub>, and the electrons produced in TiO<sub>2</sub> were trapped by the oxygen adsorption and could not be transferred to ZnO (Panigrahi & Basak, 2011). A photoconversion efficiency of ~ 1.66% (UV ray) and ~2.18% (visible light), compared to pure ZnO, resulted from the presence of the Ti element in the hybrid TiO<sub>2</sub>-ZnO film (below 1 at% Ti). Equally important, long 1D nanostructure in the presence of TiO<sub>2</sub> could harvest the excited- $h\nu$  better than the pure ZnO and other TiO<sub>2</sub> coated samples. A high aspect ratio 1D nanostructure could absorb more  $h\nu$ , resulting in an increase in  $j_p$  and  $\eta$  (Ong et al., 2005).

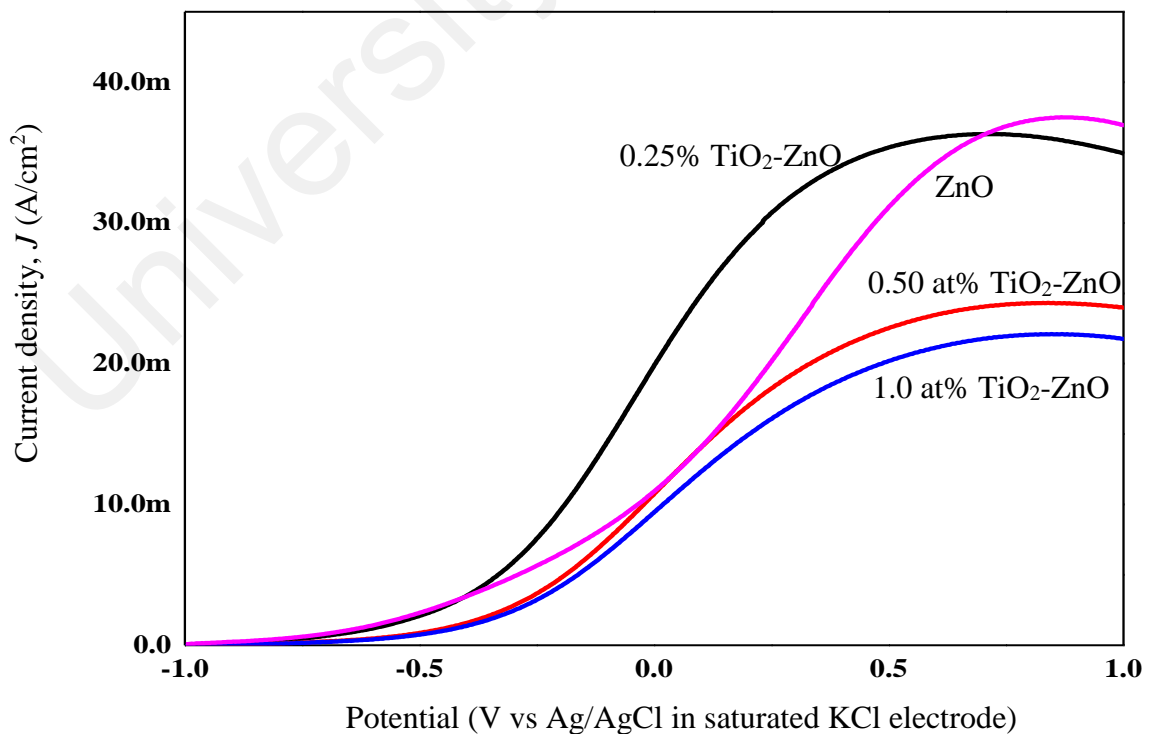


**Figure 4.34: Photocurrent response for (a) pure ZnO, (b) 0.25% TiO<sub>2</sub>-ZnO, (c) 0.50 at% TiO<sub>2</sub>-ZnO, and (d) 1.0 at% TiO<sub>2</sub>-ZnO under UV ray.**

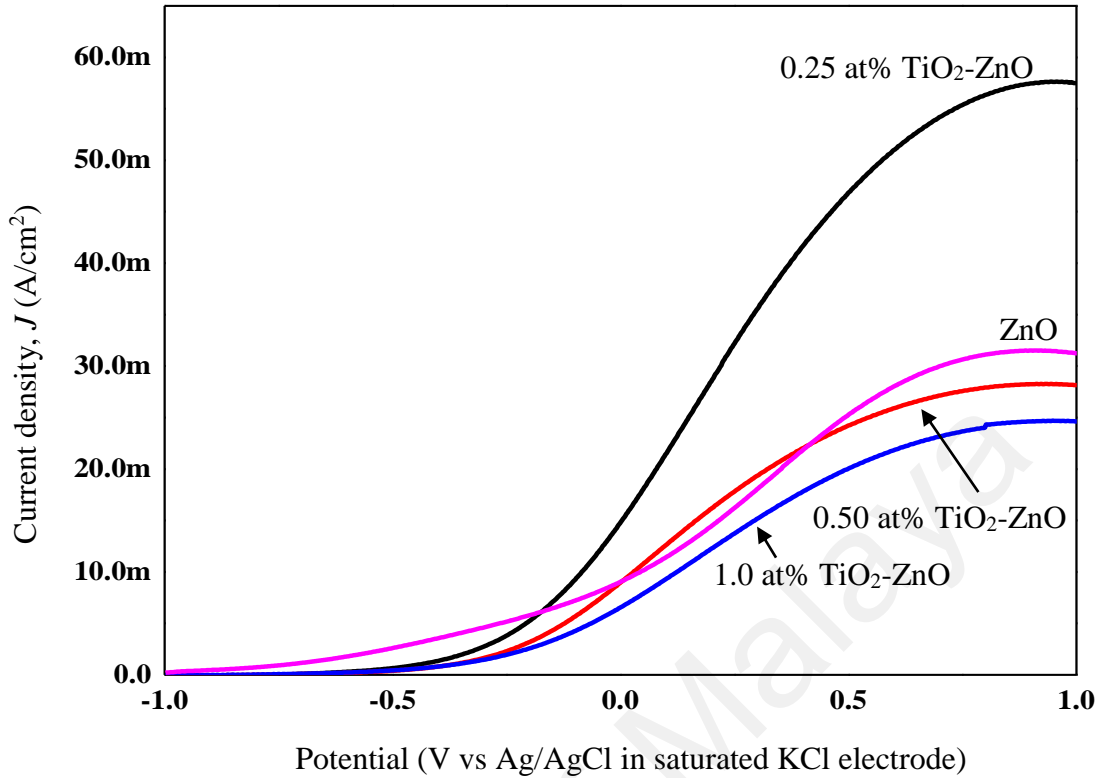


**Figure 4.35: Photocurrent response for (a) pure ZnO, (b) 0.25 at% TiO<sub>2</sub>-ZnO, (c) 0.50 at% TiO<sub>2</sub>-ZnO, and (d) 1.0 at% TiO<sub>2</sub>-ZnO under visible light.**

**Table 4.16: The photocurrent density (mA/cm<sup>2</sup>) for pure ZnO, 0.25 at% TiO<sub>2</sub>-ZnO, 0.50 at% TiO<sub>2</sub>-ZnO, and 1.0 at% TiO<sub>2</sub>-ZnO under UV ray and visible light.**

Sample	UV ray (300nm) (mA/cm <sup>2</sup> )	Visible light (500nm) (mA/cm <sup>2</sup> )
Pure ZnO	10.96	9.06
1 cycle dip-coating	19.78	14.75
2 cycles dip-coating	10.73	8.92
3 cycles dip-coating	9.40	6.52

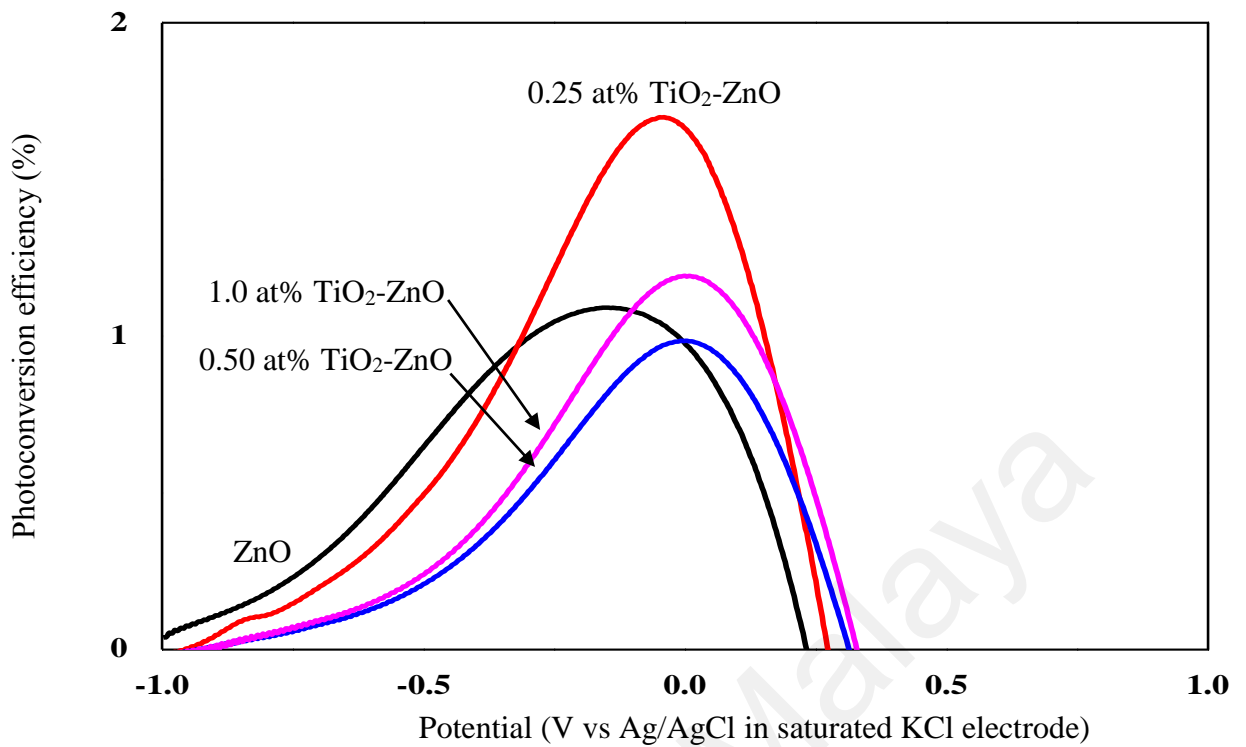


**Figure 4.36: Photoconversion efficiency for pure ZnO, 0.25 at% TiO<sub>2</sub>-ZnO, 0.50 at% TiO<sub>2</sub>-ZnO, and 1.0 at% TiO<sub>2</sub>-ZnO under UV ray.**

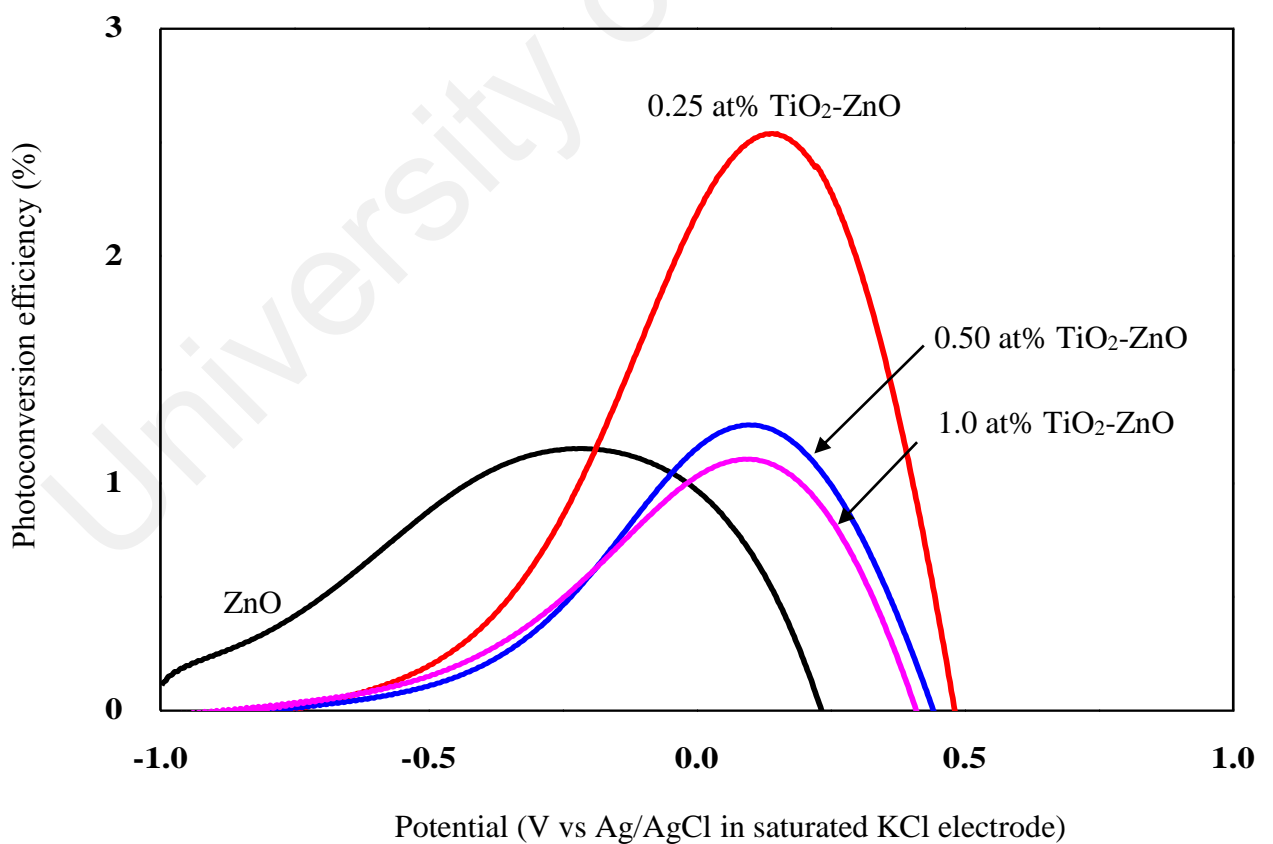


**Figure 4.37: Photoconversion efficiency for pure ZnO, 0.25 at% TiO<sub>2</sub>-ZnO, 0.50 at% TiO<sub>2</sub>-ZnO, and 1.0 at% TiO<sub>2</sub>-ZnO under visible light.**

#### 4.3.2.6 UV-vis diffusive reflectance analysis

The UV-DR Spectra of the TiO<sub>2</sub>-ZnO hybrid photocatalyst was based on the dip-coating cycle [Figure 4.38]. The band gap energies for pure ZnO, 0.25 at% TiO<sub>2</sub>-ZnO, 0.5 at% TiO<sub>2</sub>-ZnO, and 1.0 at% TiO<sub>2</sub>-ZnO are 3.20 eV, 2.85 eV, 2.96 eV, and 2.98 eV, respectively. The band gap increased with an increase in the dip-coating process. However, there was no large difference between the 0.5 at% and 1.0 at% TiO<sub>2</sub> and this was shown by the photocurrent response readings. Theoretically, three types of semiconductor heterojunction are organized by band alignment; straddling gap (type I), staggered gap (type II), and broken gap (type III). Hybrid TiO<sub>2</sub>-ZnO film had a staggered gap (type II), as proposed by previous researchers (C. Cheng *et al.*, 2014; Shao *et al.*, 2014). The proposed mechanism is as follows [Figure 4.39]. Electrons and holes in semiconductors are at their lowest energy states, originally. Therefore, the energy gradient at the interfaces tends to spatially separate those electrons and holes which were excited by the UV ray/visible light illumination on different sides of the heterojunction. Under illumination, the electrons were transferred from the conduction band (CB) of ZnO to CB of TiO<sub>2</sub>. At the same event, the holes were transferred from the valence band (VB) of TiO<sub>2</sub> to VB of ZnO. The process isolated active electrons and holes and, hence, accelerated the decrease in the electron-hole pair recombination and eroded the increase in lifespan. These phenomena directly result in an intense emission quenching as revealed by the photoluminescence results [Figure 4.33]. In addition, the high aspect ratio one dimensional structure of the ZnO nanostructure also helped to decrease the recombination probability of photogenerated carriers due to an increase in the delocalization of electrons (C. Cheng *et al.*, 2014; Leelavathi *et al.*, 2013; Shao *et al.*, 2014).

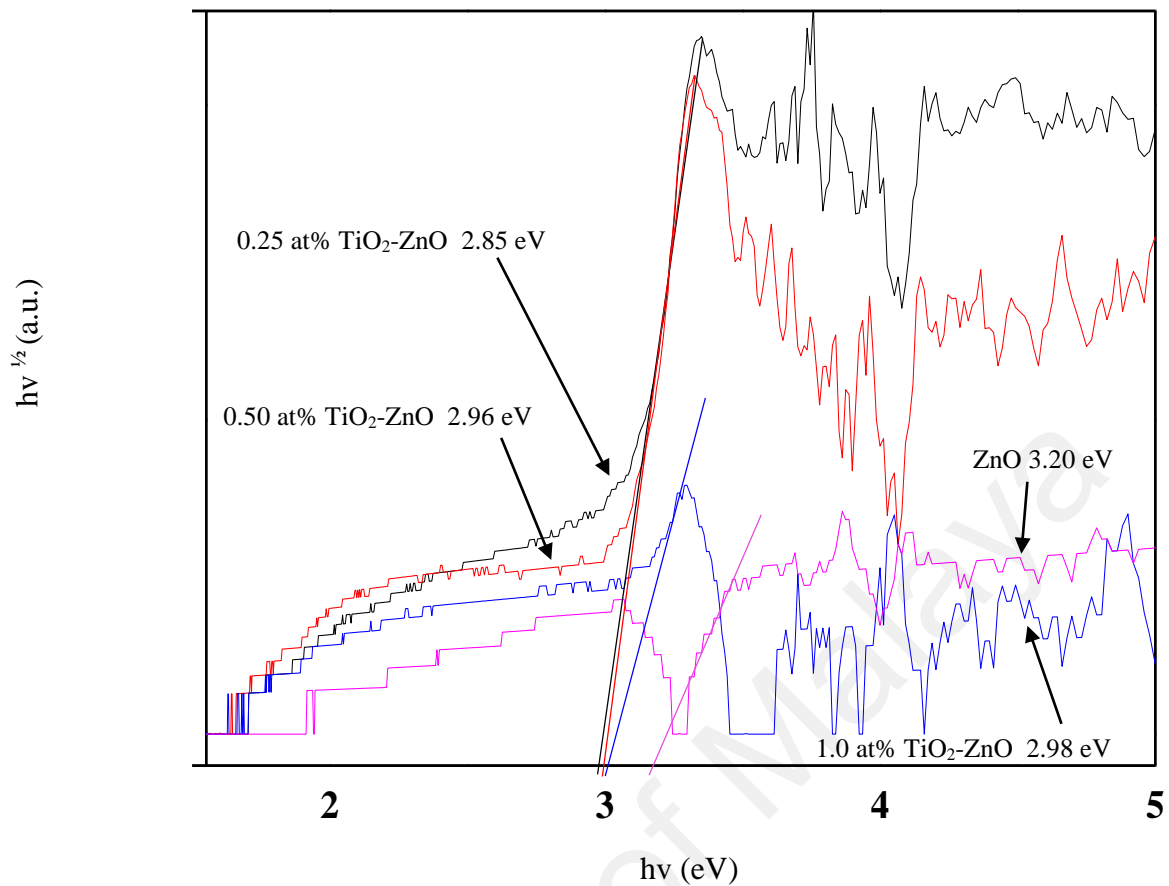


Figure 4.38: UV-DR Spectra for pure ZnO, 0.25 at% TiO<sub>2</sub>-ZnO, 0.50 at% TiO<sub>2</sub>-ZnO, and 1.0 at% TiO<sub>2</sub>-ZnO.

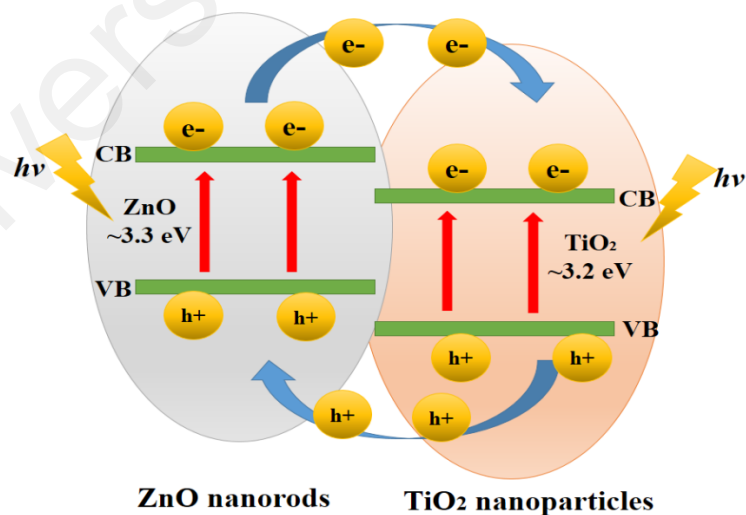
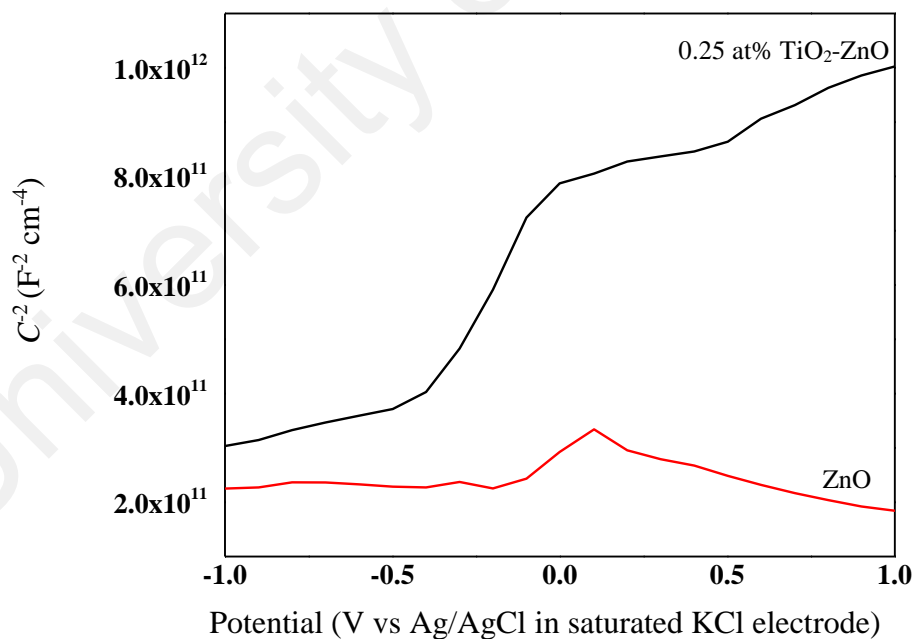


Figure 4.39: Illustration of staggered bandgap (type II) hybrid TiO<sub>2</sub>-ZnO film semiconductor and its photo-induced charge transfer and separation

#### 4.3.2.7 Mott-Schottky analysis

Referring to Figure 4.40, it was clearly showed that ZnO and TiO<sub>2</sub>-ZnO , both are n-type semiconductor. This type of semiconductor can be determined via the reflection of charge depletion behavior of n-type plots. Flat band potential ( $V_{fb}$ ) is important in Mott-Schottky (MS) analysis. Referring to Wang *et al.* and Radecka *et al.*, under biased condition, the  $C$  of photoelectrode space charge carrier region is depleted (Radecka *et al.*, 2008; X. Wang *et al.*, 2006). In addition, charge carrier density ( $N_d$ ) showed the charge distribution at the photoelectrode/electrolyte interface. The slope of linear region determined  $N_d$  and it was clearly seen that 0.25 at% TiO<sub>2</sub>-ZnO increased in charge carrier distribution as compared to ZnO at the photoelectrode/electrolyte interface. In addition, high aspect ratio 0.25 at% TiO<sub>2</sub>-ZnO (7.7) helped in promoting high charge carrier density at photoelectrode/electrolyte interface as compared to ZnO with aspect ratio 6.7.



**Figure 4.40: MS spectra of samples ZnO and 0.25at% TiO<sub>2</sub>-Zn.**

## CHAPTER 5: CONCLUSION AND RECOMMENDATIONS

### 5.1 Conclusion

This research demonstrated the fabrication of high quality ZnO nanostructure by electrodeposition technique. Followed by dip-coating technique to form hybrid TiO<sub>2</sub>-ZnO film. Photocurrent density produced from hybrid TiO<sub>2</sub>-ZnO film has been increased greatly under UV ray and visible light illumination as compared to ZnO. The results presented are important to stimulate further efforts to utilize hybrid TiO<sub>2</sub>-ZnO film for PEC water splitting applications. It also can be used to investigate similar structures for various optoelectronic applications such as optical switch, solar cells and optical fibers.

In summary, the objectives of the experiment are achieved. In the first stage of research study, the optimized conditions of 0.5 mM ZnCl<sub>2</sub>, 0.1 M KCl, temperature 70 °C, 60 min, and 1 V applied potential for synthesizing ZnO 1D nanostructure film were determined. ZnO 1D nanorod produced highest performance of PEC water splitting performance as it had anisotropic mobility of electrons and its electrons' mobility increased with the decrease of density for electrons availability to scatter. Electrons' mobility behavior could generate better transport for photogenerated charge carriers within the 1D nanorod's one-dimensional wall surface. Simultaneously, 1D nanorod prevents backward reactions and therefore reduced the number of recombination centers. The conclusions attained in this part of research work are as follow:-

- Heat treatment process helped in improving the crystallization by transforming ZnO from amorphous phase to crystalline phase. It also assisted in reducing the defects and providing better oxidation process. The atoms have enough activation energy to reside in the correct place in crystal lattice.
- Stirring process also affecting the nanostructures formed. Nanodisk-dendritic ZnO was formed at high stirring speed (> 350 rpm). Nanodisk-dendritic ZnO

is a three-dimensional (3D) ZnO nanostructures with perfect hexagonal shape. Growth occurred in globally diffusion and later oriented attachment are localized. Second hexagonal nanodisk was grown slightly dislocated from the earlier crystal due to high velocity of electrolyte.

- Electrolyte temperature changed the solubility and supersaturation index for the formation of  $\text{Zn}(\text{OH})_2$  and ZnO. Temperatures of 70 °C and 80 °C are the ideal for ZnO 1D nanostructure. It also produced almost correct stoichiometry of Zn to O ratio.
- Exposure time studied the formation of ZnO. Summarization of ZnO mechanism is as follows:
  - Substrate was given an electric supply,
  - Deposition of  $\text{Zn}(\text{OH})_2$ ,
  - Formation of ZnO seeds,
  - Dehydration process, followed by formation of ZnO nanostructures.
- 1 V is the best applied potential with optimum electrolyte mixture  $\text{ZnCl}_2$  and KCl, pH ~5-6, temperature ~70 °C. Therefore, this sets of parameter have been select for future formation of hybrid  $\text{TiO}_2$ -ZnO film.

In second stage of research study, resultant  $\text{TiO}_2$  nanosized particles were successfully formed via precipitation-peptization technique. The summaries attained in this part of experimental works are as follows:

- Temperature of precipitation-peptization produced small enough crystallite size at temperature; 60 °C and 80 °C (10.3 nm). This crystallite size is important because it determines the ability of  $\text{TiO}_2$  to be in the interstitial position between ZnO crystals during coating process  $\text{TiO}_2$ -ZnO.

- Stirring during precipitation-peptization technique, 350 rpm is an optimum speed to produce small crystallite size; 10.3 nm. Increasing the stirring speed produced bigger crystallite size. This is because higher evaporation rate lead to crystal growth rather than nucleation of new crystal.

In order to further improve the transportation of charge carriers and minimize the recombination losses in ZnO 1D nanostructure film, considerable effort has been conducted to improve the PEC water splitting performance by loading optimum content of TiO<sub>2</sub> using dip-coating technique. The conclusions attained in this stage of experimental works are as follows:

- Dip-coating is commonly used for formation of heterogeneous catalyst. But, in this experiment, prolonged exposure time produced porous structure heterogeneous catalyst. Thus, it inhibits the performance of PEC.
- Therefore, different number of dip-coating cycles was implemented. In each cycle, the dipping process was less than five seconds. 0.25 at% of TiO<sub>2</sub> demonstrated a maximum photocurrent density of 19.78 mA/cm<sup>2</sup> under UV ray and 14.75 mA/cm<sup>2</sup> under visible light. Photoconversion efficiency ~ 1.66 % (UV ray) and ~2.18 % (visible light) was achieved. It was approximately 2-3 times higher than the ZnO film. The photocurrent density and photoconversion efficiency improved due to the presence of Ti element in hybrid TiO<sub>2</sub>-ZnO film (below 1 at% Ti). The hybrid TiO<sub>2</sub>-ZnO film can benefit efficient excitonic charge separation and minimize the recombination in the heterostructure coating. Moreover, the TiO<sub>2</sub> also acts as antireflection layer that effectively increase the light absorption efficiency.

## 5.2 Suggestions and Recommendations

To make PEC water splitting more efficient, further studies and developments are required. Below are a few suggestions for further studies:

- To optimize the properties of ZnO, further studies on other parameters are needed. ZnCl<sub>2</sub> concentration, variety of directing agents, and ratio of ZnCl<sub>2</sub> to directing agent can be studied. Different substrate can be used for study other ZnO nanostructures, as the substrate also play an important role for the direction and shape nanostructures.
- Meanwhile, for further optimization of TiO<sub>2</sub>-ZnO hybrid composite for PEC water splitting, other techniques can be employed, *e.g.* chemical bath deposition and sputtering processes. The selection of coating process is important for obtain an optimize thickness of TiO<sub>2</sub>.

## REFERENCES

- Abd-Ellah, M., Moghimi, N., Zhang, L., Heinig, N. F., Zhao, L., Thomas, J. P., & Leung, K. (2013). Effect of Electrolyte Conductivity on Controlled Electrochemical Synthesis of Zinc Oxide Nanotubes and Nanorods. *The Journal of Physical Chemistry C*, 117(13), 6794-6799.
- Abd Samad, N. A., Lai, C. W., & Abd Hamid, S. B. (2015a). Easy Formation of Nanodisk-Dendritic ZnO Film via Controlled Electrodeposition Process. *Journal of Nanomaterials*. doi:10.1155/2015/563728
- Abd Samad, N. A., Lai, C. W., & Abd Hamid, S. B. (2015b). Easy Formation of Nanodisk-Dendritic ZnO Film via Controlled Electrodeposition Process. *Journal of Nanomaterials*, 2015.
- Ahn, K.-S., Lee, S.-H., Dillon, A. C., Tracy, C. E., & Pitts, R. (2007). The effect of thermal annealing on photoelectrochemical responses of WO<sub>3</sub> thin films. *Journal of Applied Physics*, 101(9), 093524-093524-093524.
- Al-Gaashani, R., Radiman, S., Daud, A. R., Tabet, N., & Al-Douri, Y. (2013). XPS and optical studies of different morphologies of ZnO nanostructures prepared by microwave methods. *Ceramics International*, 39(3), 2283-2292.
- Alim, K. A., Fonoberov, V. A., & Balandin, A. A. (2005). Origin of the optical phonon frequency shifts in ZnO quantum dots. *Applied Physics Letters*, 86(5), 53103-53103.
- Alphonse, P., Varghese, A., & Tendero, C. (2010). Stable hydrosols for TiO<sub>2</sub> coatings. *Journal of sol-gel science and technology*, 56(3), 250-263.
- Alvi, N. H. (2011). *Luminescence Properties of ZnO Nanostructures and Their Implementation as White Light Emitting Diodes (LEDs)*. Linköping University
- Andersson, M., Österlund, L., Ljungstroem, S., & Palmqvist, A. (2002). Preparation of nanosize anatase and rutile TiO<sub>2</sub> by hydrothermal treatment of microemulsions and their activity for photocatalytic wet oxidation of phenol. *The Journal of Physical Chemistry B*, 106(41), 10674-10679.
- Andrić, P., Meyer, A. S., Jensen, P. A., & Dam-Johansen, K. (2010). Reactor design for minimizing product inhibition during enzymatic lignocellulose hydrolysis: I. Significance and mechanism of cellobiose and glucose inhibition on cellulolytic enzymes. *Biotechnology Advances*, 28(3), 308-324.
- Anpo, M., Nakaya, H., Kodama, S., Kubokawa, Y., Domen, K., & Onishi, T. (1986). Photocatalysis over binary metal oxides. Enhancement of the photocatalytic activity of titanium dioxide in titanium-silicon oxides. *The Journal of Physical Chemistry*, 90(8), 1633-1636.
- Atwood, J. D., & Zuckerman, J. J. (1999). *Inorganic reactions and methods: Formation of ceramics* (Vol. 18): Vch Pub.

- Aziz, N. S. A., Mahmood, M. R., Yasui, K., & Hashim, A. M. (2014). Seed/catalyst-free vertical growth of high-density electrodeposited zinc oxide nanostructures on a single-layer graphene. *Nanoscale Research Letters*, 9(1), 1-7.
- Bagheri, S., Shameli, K., & Abd Hamid, S. B. (2012). Synthesis and characterization of anatase titanium dioxide nanoparticles using egg white solution via sol-gel Method. *Journal of Chemistry*, 2013.
- Bahadur, H., Srivastava, A. K., Sharma, R. K., & Chandra, S. (2007). Morphologies of sol-gel derived thin films of ZnO using different precursor materials and their nanostructures. *Nanoscale Research Letters*, 2(10), 469-475. doi:10.1007/s11671-007-9089-x
- Banerjee, D., Lao, J., Wang, D., Huang, J., Ren, Z., Steeves, D., . . . Sennett, M. (2003). Large-quantity free-standing ZnO nanowires. *Applied Physics Letters*, 83(10), 2061-2063.
- Barron, J., Ashton, C., & Geary, L. (2006). *The effects of temperature on pH measurement*. Paper presented at the 57th Annual Meeting of the International Society of Electrochemistry, Edinburgh, Technical Services Department, Reagecon Diagnostics Ltd, Ireland.
- Barthel, J. M., Krienke, H., & Kunz, W. (1998). *Physical chemistry of electrolyte solutions: modern aspects* (Vol. 5): Springer Science & Business Media.
- Bhandarkar, S. D., Chandross, E. A., & Putvinski, T. M. (2000). Method for forming article using sol-gel processing: Google Patents.
- Bilgen, E., Ducarroir, M., Foex, M., Sibieude, F., & Trombe, F. (1977). Use of solar energy for direct and two-step water decomposition cycles. *International Journal of Hydrogen Energy*, 2(3), 251-257.
- Birkholz, M. (2006). *Thin film analysis by X-ray scattering*: John Wiley & Sons.
- Bitenc, M., & Orel, Z. C. (2009). Synthesis and characterization of crystalline hexagonal bipods of zinc oxide. *Materials Research Bulletin*, 44(2), 381-387.
- Boddenberg, B. (1996). Concepts in Physical Chemistry. *Zeitschrift für Physikalische Chemie*, 195(Part\_1\_2), 287-289.
- Bond, G., Showers, W., Cheseby, M., Lotti, R., Almasi, P., Priore, P., . . . Bonani, G. (1997). A pervasive millennial-scale cycle in North Atlantic Holocene and glacial climates. *Science*, 278(5341), 1257-1266.
- Bornand, V., & Mezy, A. (2011). An alternative approach for the oriented growth of ZnO nanostructures. *Materials Letters*, 65(9), 1363-1366. doi:10.1016/j.matlet.2011.01.083
- Bruncko, J., Vincze, A., Netrvalova, M., Šutta, P., Hasko, D., & Michalka, M. (2011). Annealing and recrystallization of amorphous ZnO thin films deposited under cryogenic conditions by pulsed laser deposition. *Thin Solid Films*, 520(2), 866-870.

- Bumrah, G. S., & Sharma, R. M. (2015). Raman spectroscopy–Basic principle, instrumentation and selected applications for the characterization of drugs of abuse. *Egyptian Journal of Forensic Sciences*.
- Cai, A., Muth, J., Reed, M., Porter, H., Jin, C., & Narayan, J. (2002). *Effect of Growth Temperature and Annealing on ZnO*. Paper presented at the MRS Proceedings.
- Callister, W. D., & Rethwisch, D. G. (2007). *Materials science and engineering: an introduction* (Vol. 7): Wiley New York.
- Carter, C. B., & Norton, M. G. (2007). *Ceramic materials: science and engineering*: Springer Science & Business Media.
- Casaletto, M., Longo, A., Martorana, A., Prestianni, A., & Venezia, A. (2006). XPS study of supported gold catalysts: the role of Au<sup>0</sup> and Au<sup>+</sup>  $\delta$  species as active sites. *Surface and interface analysis*, 38(4), 215-218.
- Chandrinou, C., Boukos, N., Stogios, C., & Travlos, A. (2009). PL study of oxygen defect formation in ZnO nanorods. *Microelectronics Journal*, 40(2), 296-298.
- Chatenet, M., Dubau, L., Job, N., & Maillard, F. (2010). The (electro) catalyst| membrane interface in the Proton Exchange Membrane Fuel Cell: Similarities and differences with non-electrochemical Catalytic Membrane Reactors. *Catalysis Today*, 156(3), 76-86.
- Chaturvedi, S., Dave, P. N., & Shah, N. (2012). Applications of nano-catalyst in new era. *Journal of Saudi Chemical Society*, 16(3), 307-325.
- Chen, Q.-P., Xue, M.-Z., Sheng, Q.-R., Liu, Y.-G., & Ma, Z.-F. (2006). Electrochemical growth of nanopillar zinc oxide films by applying a low concentration of zinc nitrate precursor. *Electrochemical and solid-state letters*, 9(3), C58-C61.
- Chen, W., Liu, W., Hsieh, S., & Tsai, T. (2007). Preparation of nanosized ZnO using  $\alpha$  brass. *Applied Surface Science*, 253(16), 6749-6753.
- Chen, Y.-W., Lee, D.-S., & Chen, H.-J. (2012). Preferential oxidation of CO in H<sub>2</sub> stream on Au/ZnO–TiO<sub>2</sub> catalysts. *International Journal of Hydrogen Energy*, 37(20), 15140-15155.
- Chen, Z., Shum, K., Salagaj, T., Zhang, W., & Strobl, K. (2010). ZnO thin films synthesized by chemical vapor deposition. *Energy*, 8, 8-9.
- Cheng, C., Amini, A., Zhu, C., Xu, Z., Song, H., & Wang, N. (2014). Enhanced photocatalytic performance of TiO<sub>2</sub>-ZnO hybrid nanostructures. *Scientific reports*, 4.
- Cheng, C., Yu, K. F., Cai, Y., Fung, K. K., & Wang, N. (2007). Site-specific deposition of titanium oxide on zinc oxide nanorods. *The Journal of Physical Chemistry C*, 111(45), 16712-16716.
- Cheng, H.-M., Hsu, H.-C., Tseng, Y.-K., Lin, L.-J., & Hsieh, W.-F. (2005). Raman scattering and efficient UV photoluminescence from well-aligned ZnO nanowires

epitaxially grown on GaN buffer layer. *The Journal of Physical Chemistry B*, 109(18), 8749-8754.

- Chi, C. Y., Chin, S. C., Lu, Y. C., Hong, L., Lin, Y. L., Jen, F. Y., . . . Segawa, Y. (2005). Nanostructures and optical characteristics of ZnO thin-film-like samples grown on GaN. *Nanotechnology*, 16(12), 3084-3091. doi:10.1088/0957-4484/16/12/060
- Chin, H.-S., & Chao, L.-S. (2013). The effect of thermal annealing processes on structural and photoluminescence of zinc oxide thin film. *Journal of Nanomaterials*, 2013, 4.
- Chiroma, H., Abdul-kareem, S., Khan, A., Nawi, N. M., Gital, A. Y., Shuib, L., . . . Herawan, T. (2015). Global Warming: Predicting OPEC Carbon Dioxide Emissions from Petroleum Consumption Using Neural Network and Hybrid Cuckoo Search Algorithm. *Plos One*, 10(8), 21. doi:10.1371/journal.pone.0136140
- Chiu, W., Khiew, P., Cloke, M., Isa, D., Tan, T., Radiman, S., . . . Lim, H. (2010). Photocatalytic study of two-dimensional ZnO nanopellets in the decomposition of methylene blue. *Chemical Engineering Journal*, 158(2), 345-352.
- Chiuta, S., Everson, R. C., Neomagus, H., van der Gryp, P., & Bessarabov, D. G. (2013). Reactor technology options for distributed hydrogen generation via ammonia decomposition: A review. *International Journal of Hydrogen Energy*, 38(35), 14968-14991. doi:10.1016/j.ijhydene.2013.09.067
- Chong, M. N., Jin, B., Chow, C. W., & Saint, C. (2010). Recent developments in photocatalytic water treatment technology: a review. *Water Research*, 44(10), 2997-3027.
- Cicea, C., Marinescu, C., Popa, I., & Dobrin, C. (2014). Environmental efficiency of investments in renewable energy: Comparative analysis at macroeconomic level. *Renewable and Sustainable Energy Reviews*, 30(0), 555-564. doi:<http://dx.doi.org/10.1016/j.rser.2013.10.034>
- Clarizia, L., Spasiano, D., Di Somma, I., Marotta, R., Andreozzi, R., & Dionysiou, D. D. (2014). Copper modified-TiO<sub>2</sub> catalysts for hydrogen generation through photoreforming of organics. A short review. *International Journal of Hydrogen Energy*, 39(30), 16812-16831. doi:10.1016/j.ijhydene.2014.08.037
- Clavel, G., Marichy, C., Willinger, M. G., Ravaine, S., Zitoun, D., & Pinna, N. (2010). CoFe<sub>2</sub>O<sub>4</sub>-TiO<sub>2</sub> and CoFe<sub>2</sub>O<sub>4</sub>-ZnO Thin Film Nanostructures Elaborated from Colloidal Chemistry and Atomic Layer Deposition. *Langmuir*, 26(23), 18400-18407. doi:10.1021/la103364y
- Crawford, G., & Chawla, N. (2009). Porous hierarchical TiO<sub>2</sub> nanostructures: processing and microstructure relationships. *Acta Materialia*, 57(3), 854-867.
- Cui, J., & Gibson, U. J. (2005). Enhanced nucleation, growth rate, and dopant incorporation in ZnO nanowires. *The Journal of Physical Chemistry B*, 109(46), 22074-22077.

- Dai, K., Peng, T. Y., Chen, H., Zhang, R. X., & Zhang, Y. X. (2008). Photocatalytic degradation and mineralization of commercial methamidophos in aqueous Titania suspension. *Environmental Science & Technology*, 42(5), 1505-1510. doi:10.1021/es702268p
- Dai, S., Li, Y., Du, Z., & Carter, K. R. (2013). Electrochemical deposition of ZnO hierarchical nanostructures from hydrogel coated electrodes. *Journal of The Electrochemical Society*, 160(4), D156-D162.
- Dao, T., Dang, C., Han, G., Hoang, C., Yi, W., Narayanamurti, V., & Nagao, T. (2013). Chemically synthesized nanowire TiO<sub>2</sub>/ZnO core-shell pn junction array for high sensitivity ultraviolet photodetector. *Applied Physics Letters*, 103(19), 193119.
- Das, S., & Jayaraman, V. (2014). SnO<sub>2</sub>: a comprehensive review on structures and gas sensors. *Progress in Materials Science*, 66, 112-255.
- Demmin, J. C. (2001). SPECIAL REPORT-Process technology update: Progress on all fronts-Ultra-shallow Junctions. *Solid State Technology*, 44(1), 68-69.
- Devoy, R. J. (2014). Sea-Level Rise: Causes, Impacts, and Scenarios for Change. *Coastal and Marine Hazards, Risks, and Disasters*, 197.
- Djurišić, A., Leung, Y., Tam, K., Hsu, Y., Ding, L., Ge, W., . . . Tam, H. (2007). Defect emissions in ZnO nanostructures. *Nanotechnology*, 18(9), 095702.
- Dobkin, D. M., & Zuraw, M. K. (2003). *Principles of chemical vapor deposition*: Springer.
- Du, J., Liu, Z., Huang, Y., Gao, Y., Han, B., Li, W., & Yang, G. (2005). Control of ZnO morphologies via surfactants assisted route in the subcritical water. *Journal of Crystal Growth*, 280(1), 126-134.
- Du, J. L. Y. C. J., & Lai, H. Study of luminescence and epitaxy of green light emitting ZnO thin films prepared by MOCVD. *National Dong Hwa University. Hualien*, 974.
- Elias, J., Tena-Zaera, R., & Lévy-Clément, C. (2007). Electrodeposition of ZnO nanowires with controlled dimensions for photovoltaic applications: Role of buffer layer. *Thin Solid Films*, 515(24), 8553-8557.
- Elias, J., Tena-Zaera, R., & Lévy-Clément, C. (2008). Effect of the chemical nature of the anions on the electrodeposition of ZnO nanowire arrays. *The Journal of Physical Chemistry C*, 112(15), 5736-5741.
- Erdoğan, A., Çakal, G., Özkar, S., & Eroğlu, İ. (2004). The effect of stirring rate on dissolution of colemanite and particle size of gypsum crystals during the boric acid production in a batch reactor *U. Uluslararası Bor Sempozyumu, Eskişehir* (pp. 23-25).
- Espitia, P. J. P., Soares, N. d. F. F., dos Reis Coimbra, J. S., de Andrade, N. J., Cruz, R. S., & Medeiros, E. A. A. (2012). Zinc oxide nanoparticles: synthesis,

- antimicrobial activity and food packaging applications. *Food and Bioprocess Technology*, 5(5), 1447-1464.
- Ewan, B., & Allen, R. (2005). A figure of merit assessment of the routes to hydrogen. *International Journal of Hydrogen Energy*, 30(8), 809-819.
- Exarhos, G. J., & Sharma, S. K. (1995). Influence of processing variables on the structure and properties of ZnO films. *Thin Solid Films*, 270(1), 27-32.
- Fang, D., Yao, P., & Li, H. (2014). Influence of annealing temperature on the structural and optical properties of Mg–Al co-doped ZnO thin films prepared via sol–gel method. *Ceramics International*, 40(4), 5873-5880. doi:10.1016/j.ceramint.2013.11.030
- Fierro, J. L. G. (2005). *Metal Oxides: chemistry and applications*: CRC press.
- Fierro, J. L. G. (2010). *Metal oxides: chemistry and applications*: CRC press.
- Fletcher, E. A., & Moen, R. L. (1977). Hydrogen-and oxygen from water. *Science*, 197(4308), 1050-1056.
- Fong, Y. Y., Abdullah, A. Z., Ahmad, A. L., & Bhatia, S. (2008). Development of functionalized zeolite membrane and its potential role as reactor combined separator for para-xylene production from xylene isomers. *Chemical Engineering Journal*, 139(1), 172-193.
- Fostad, G., Hafell, B., Førde, A., Dittmann, R., Sabetrasekh, R., Will, J., . . . Haugen, H. (2009). Loadable TiO<sub>2</sub> scaffolds—A correlation study between processing parameters, micro CT analysis and mechanical strength. *Journal of the European Ceramic Society*, 29(13), 2773-2781.
- Frade, T., Jorge, M. M., & Gomes, A. (2012). One-dimensional ZnO nanostructured films: Effect of oxide nanoparticles. *Materials Letters*, 82, 13-15.
- Gad, S. C. (2008). *Pharmaceutical manufacturing handbook: production and processes* (Vol. 5): John Wiley & Sons.
- Gao, X., Hamelin, A., & Weaver, M. J. (1991). Atomic relaxation at ordered electrode surfaces probed by scanning tunneling microscopy: Au (111) in aqueous solution compared with ultrahigh-vacuum environments. *The Journal of chemical physics*, 95(9), 6993-6996.
- George, L., Sappati, S., Ghosh, P., & Devi, R. N. (2015). Surface Site Modulations by Conjugated Organic Molecules To Enhance Visible Light Activity of ZnO Nanostructures in Photocatalytic Water Splitting. *Journal of Physical Chemistry C*, 119(6), 3060-3067. doi:10.1021/jp511996z
- Giulietti, M., Seckler, M., Derenzo, S., Ré, M., & Cekinski, E. (2001). Industrial crystallization and precipitation from solutions: state of the technique. *Brazilian Journal of Chemical Engineering*, 18(4), 423-440.

- Goh, H.-S., Adnan, R., & Farrukh, M. A. (2011). ZnO nanoflake arrays prepared via anodization and their performance in the photodegradation of methyl orange. *Turkish Journal of Chemistry*, 35(3), 375-391.
- Goux, A., Pauporté, T., Chivot, J., & Lincot, D. (2005). Temperature effects on ZnO electrodeposition. *Electrochimica Acta*, 50(11), 2239-2248.
- Grätzel, M. (2001). Photoelectrochemical cells. *Nature*, 414(6861), 338-344.
- Greene, L. E., Law, M., Yuhas, B. D., & Yang, P. (2007). ZnO-TiO<sub>2</sub> core-shell nanorod/P3HT solar cells. *The Journal of Physical Chemistry C*, 111(50), 18451-18456.
- Grimes, C. A., Varghese, O. K., & Ranjan, S. (2007). *Light, water, hydrogen: the solar generation of hydrogen by water photoelectrolysis*: Springer Science & Business Media.
- Hahn, Y.-B. (2011). Zinc oxide nanostructures and their applications. *Korean Journal of Chemical Engineering*, 28(9), 1797-1813.
- Han, C., Luque, R., & Dionysiou, D. D. (2012). Facile preparation of controllable size monodisperse anatase titania nanoparticles. *Chemical Communications*, 48(13), 1860-1862.
- Hang, D.-R., Islam, S. E., Sharma, K. H., Kuo, S.-W., Zhang, C.-Z., & Wang, J.-J. (2014). Annealing effects on the optical and morphological properties of ZnO nanorods on AZO substrate by using aqueous solution method at low temperature. *Nanoscale Research Letters*, 9(1), 1.
- He, G., Liu, M., Zhu, L., Chang, M., Fang, Q., & Zhang, L. (2005). Effect of postdeposition annealing on the thermal stability and structural characteristics of sputtered HfO<sub>2</sub> films on Si (100). *Surface Science*, 576(1), 67-75.
- Hernández, S., Cauda, V., Hidalgo, D., Rivera, V. F., Manfredi, D., Chiodoni, A., & Pirri, F. C. (2014). Fast and low-cost synthesis of 1D ZnO–TiO<sub>2</sub> core–shell nanoarrays: characterization and enhanced photo-electrochemical performance for water splitting. *Journal of Alloys and Compounds*, 615, S530-S537.
- Hoffmann, M. R., Martin, S. T., Choi, W., & Bahnemann, D. W. (1995). Environmental applications of semiconductor photocatalysis. *Chemical reviews*, 95(1), 69-96.
- Hosseini, S., Sarsari, I. A., Kameli, P., & Salamati, H. (2015). Effect of Ag doping on structural, optical, and photocatalytic properties of ZnO nanoparticles. *Journal of Alloys and Compounds*, 640, 408-415.
- Hu, J. A., Zhu, F., Matulionis, I., Deutsch, T., Gaillard, N., Miller, E., & Madan, A. (2009). Development of a hybrid photoelectrochemical (PEC) device with amorphous silicon carbide as the photoelectrode for water splitting. In F. ShahedipourSandvik, E. F. Schubert, L. D. Bell, V. Tilak, & A. W. Bett (Eds.), *Compound Semiconductors for Energy Applications and Environmental Sustainability* (Vol. 1167, pp. 121-126). Warrendale: Materials Research Society.

- Huang, J., El-Azzami, L., & Ho, W. W. (2005). Modeling of CO<sub>2</sub>-selective water gas shift membrane reactor for fuel cell. *Journal of membrane science*, 261(1), 67-75.
- Huang, K., Li, Y., Lin, S., Liang, C., Wang, H., Ye, C., . . . Yang, H. (2014). A facile route to reduced graphene oxide–zinc oxide nanorod composites with enhanced photocatalytic activity. *Powder Technology*, 257, 113-119.
- Huang, Y., He, J., Zhang, Y., Dai, Y., Gu, Y., Wang, S., & Zhou, C. (2006). Morphology, structures and properties of ZnO nanobelts fabricated by Zn-powder evaporation without catalyst at lower temperature. *Journal of Materials Science*, 41(10), 3057-3062.
- Hurst, V. J., Schroeder, P. A., & Styron, R. W. (1997). Accurate quantification of quartz and other phases by powder X-ray diffractometry. *Analytica Chimica Acta*, 337(3), 233-252.
- Hwang, C.-C., & Wu, T.-Y. (2004). Synthesis and characterization of nanocrystalline ZnO powders by a novel combustion synthesis method. *Materials Science and Engineering: B*, 111(2), 197-206.
- Ihara, T., Miyoshi, M., Iriyama, Y., Matsumoto, O., & Sugihara, S. (2003). Visible-light-active titanium oxide photocatalyst realized by an oxygen-deficient structure and by nitrogen doping. *Applied Catalysis B: Environmental*, 42(4), 403-409.
- Iulianelli, A., Ribeiro, P., Mendes, A., & Basile, A. (2014). Methanol steam reforming for hydrogen generation via conventional and membrane reactors: A review. *Renewable & Sustainable Energy Reviews*, 29, 355-368. doi:10.1016/j.rser.2013.08.032
- Janotti, A., & Van de Walle, C. G. (2007). Native point defects in ZnO. *Physical Review B*, 76(16), 165202.
- Janotti, A., & Van de Walle, C. G. (2009). Fundamentals of zinc oxide as a semiconductor. *Reports on Progress in Physics*, 72(12), 126501.
- Jian-Bin, H., Shao-Wu, W., Yong, L., Zong-Ci, Z., & Xin-Yu, W. (2012). Debates on the causes of global warming. *Advances in Climate Change Research*, 3(1), 38-44.
- Jiang, S. P. (2006). A review of wet impregnation—An alternative method for the fabrication of high performance and nano-structured electrodes of solid oxide fuel cells. *Materials Science and Engineering: A*, 418(1), 199-210.
- Jlassi, M., Chorfi, H., Saadoun, M., & Bessaïs, B. (2013). ZnO ratio-induced photocatalytic behavior of TiO<sub>2</sub>–ZnO nanocomposite. *Superlattices and Microstructures*, 62, 192-199.
- Jose-Yacamán, M., Gutierrez-Wing, C., Miki, M., Yang, D.-Q., Piyakis, K., & Sacher, E. (2005). Surface diffusion and coalescence of mobile metal nanoparticles. *The Journal of Physical Chemistry B*, 109(19), 9703-9711.

- Justicia, I., García, G., Battiston, G., Gerbasi, R., Ager, F., Guerra, M., . . . Figueras, A. (2005). Photocatalysis in the visible range of sub-stoichiometric anatase films prepared by MOCVD. *Electrochimica Acta*, 50(23), 4605-4608.
- Kapałka, A., Fóti, G., Comninellis, C., & Chen, G. (2010). Electrochemistry for the Environment.
- Kaygusuz, K. (2009). Energy and environmental issues relating to greenhouse gas emissions for sustainable development in Turkey. *Renewable and Sustainable Energy Reviews*, 13(1), 253-270. doi:<http://dx.doi.org/10.1016/j.rser.2007.07.009>
- Kern, W. (2012). *Thin film processes II* (Vol. 2): Academic press.
- Khojier, K., Savaloni, H., & Amani, E. (2014). Influence of annealing conditions on the crystallographic structure, chemical composition and luminescence of ZnO thin films. *Applied Surface Science*, 289, 564-570. doi:10.1016/j.apsusc.2013.11.043
- Khramovskyy, V., & Yakimova, R. (2012). Morphology engineering of ZnO nanostructures. *Physica B: Condensed Matter*, 407(10), 1533-1537.
- Khrypunov, G., Klochko, N., Volkova, N., Kopach, V., Lyubov, V., & Klepikova, K. (2011). *Pulse and direct current electrodeposition of zinc oxide layers for solar cells with extra thin absorbers*. Paper presented at the World Renewable Energy Congress WREC-2011, Linköping, Sweden.
- Kim, K.-S., & Kim, H. W. (2003). Synthesis of ZnO nanorod on bare Si substrate using metal organic chemical vapor deposition. *Physica B: Condensed Matter*, 328(3), 368-371.
- Kim, S. J., Lee, J., & Choi, J. (2008). Understanding of anodization of zinc in an electrolyte containing fluoride ions. *Electrochimica Acta*, 53(27), 7941-7945.
- Kim, Y.-J., Lee, J.-H., & Yi, G.-C. (2009). Vertically aligned ZnO nanostructures grown on graphene layers. *Applied Physics Letters*, 95(21), 213101.
- Kim, Y. J., Hadiywarman, Yoon, A., Kim, M., Yi, G. C., & Liu, C. (2011). Hydrothermally grown ZnO nanostructures on few-layer graphene sheets. *Nanotechnology*, 22(24), 8. doi:10.1088/0957-4484/22/24/245603
- Kirkby, J. (2007). Cosmic rays and climate. *Surveys in Geophysics*, 28(5-6), 333-375.
- Kisi, E. H., & Elcombe, M. M. (1989). u parameters for the wurtzite structure of ZnS and ZnO using powder neutron diffraction. *Acta Crystallographica Section C: Crystal Structure Communications*, 45(12), 1867-1870.
- Kniess, C. T., de Lima, J. C., & Prates, P. B. (2012). *The quantification of crystalline phases in materials: applications of Rietveld method*: INTECH Open Access Publisher Rijeka.
- Kogan, A. (1998). Direct solar thermal splitting of water and on-site separation of the products—II. Experimental feasibility study. *International Journal of Hydrogen Energy*, 23(2), 89-98.

- Kołodziejczak-Radzimska, A., & Jesionowski, T. (2014). Zinc oxide—from synthesis to application: a review. *Materials*, 7(4), 2833-2881.
- Könenkamp, R., Boedecker, K., Lux-Steiner, M. C., Poschenrieder, M., Zenia, F., Levy-Clement, C., & Wagner, S. (2000). Thin film semiconductor deposition on free-standing ZnO columns. *Applied Physics Letters*, 77(16), 2575-2577.
- Kong, X. Y., Ding, Y., Yang, R., & Wang, Z. L. (2004). Single-crystal nanorings formed by epitaxial self-coiling of polar nanobelts. *Science*, 303(5662), 1348-1351.
- Kröger, F., & Vink, H. (1954). The origin of the fluorescence in self-activated ZnS, CdS, and ZnO. *The Journal of chemical physics*, 22(2), 250-252.
- Lai, C. W., & Sreekantan, S. (2011). Effect of applied potential on the formation of self-organized TiO<sub>2</sub> nanotube arrays and its photoelectrochemical response. *Journal of Nanomaterials*, 2011, 11.
- Lai, C. W., & Sreekantan, S. (2014). Photoelectrochemical properties of TiO<sub>2</sub> nanotube arrays: effect of electrolyte pH and annealing temperature. *Journal of Experimental Nanoscience*, 9(3), 230-239.
- Lascelles, S., McCarthy, G., Butterworth, M., & Armes, S. (1998). Effect of synthesis parameters on the particle size, composition and colloid stability of polypyrrole-silica nanocomposite particles. *Colloid and Polymer Science*, 276(10), 893-902.
- Lee, K. Y., Kumar, B., Park, H.-K., Choi, W. M., Choi, J.-Y., & Kim, S.-W. (2012). Growth of high quality ZnO nanowires on graphene. *Journal of Nanoscience and Nanotechnology*, 12(2), 1551-1554.
- Leelavathi, A., Madras, G., & Ravishankar, N. (2013). Origin of enhanced photocatalytic activity and photoconduction in high aspect ratio ZnO nanorods. *Physical Chemistry Chemical Physics*, 15(26), 10795-10802.
- Lepot, N., Van Bael, M., Van den Rul, H., D'Haen, J., Peeters, R., Franco, D., & Mullens, J. (2007). Synthesis of ZnO nanorods from aqueous solution. *Materials Letters*, 61(13), 2624-2627.
- Leskelä, M., & Ritala, M. (2002). Atomic layer deposition (ALD): from precursors to thin film structures. *Thin Solid Films*, 409(1), 138-146.
- Lévy-Clément, C., Tena-Zaera, R., Ryan, M. A., Katty, A., & Hodes, G. (2005). CdSe-Sensitized p-CuSCN/Nanowire n-ZnO Heterojunctions. *Advanced Materials*, 17(12), 1512-1515.
- Li, G.-R., Lu, X.-H., Qu, D.-L., Yao, C.-Z., Zheng, F.-l., Bu, Q., . . . Tong, Y.-X. (2007). Electrochemical growth and control of ZnO dendritic structures. *The Journal of Physical Chemistry C*, 111(18), 6678-6683.
- Li, J., & Wu, N. (2015). Semiconductor-based photocatalysts and photoelectrochemical cells for solar fuel generation: a review. *Catalysis Science & Technology*, 5(3), 1360-1384.

- Li, Q., Bian, J., Sun, J., Wang, J., Luo, Y., Sun, K., & Yu, D. (2010). Controllable growth of well-aligned ZnO nanorod arrays by low-temperature wet chemical bath deposition method. *Applied Surface Science*, 256(6), 1698-1702.
- Liao, C.-H., Huang, C.-W., & Wu, J. (2012). Hydrogen production from semiconductor-based photocatalysis via water splitting. *Catalysts*, 2(4), 490-516.
- Licht, S., Wang, B., Mukerji, S., Soga, T., Umeno, M., & Tributsch, H. (2000). Efficient solar water splitting, exemplified by RuO<sub>2</sub>-catalyzed AlGaAs/Si photoelectrolysis. *The Journal of Physical Chemistry B*, 104(38), 8920-8924.
- Licht, S., Wang, B., Mukerji, S., Soga, T., Umeno, M., & Tributsch, H. (2001). Over 18% solar energy conversion to generation of hydrogen fuel; theory and experiment for efficient solar water splitting. *International Journal of Hydrogen Energy*, 26(7), 653-659.
- Lin, L., Yang, Y., Men, L., Wang, X., He, D., Chai, Y., . . . Tang, Q. (2013). A highly efficient TiO<sub>2</sub>@ ZnO n-p-n heterojunction nanorod photocatalyst. *Nanoscale*, 5(2), 588-593.
- Lin, Y. (2001). Microporous and dense inorganic membranes: current status and prospective. *Separation and Purification Technology*, 25(1), 39-55.
- Linsebigler, A. L., Lu, G., & Yates Jr, J. T. (1995). Photocatalysis on TiO<sub>2</sub> surfaces: principles, mechanisms, and selected results. *Chemical reviews*, 95(3), 735-758.
- Liu, B. H., & Li, Z. P. (2009). A review: Hydrogen generation from borohydride hydrolysis reaction. *Journal of Power Sources*, 187(2), 527-534. doi:10.1016/j.jpowsour.2008.11.032
- Liu, J., Huang, X., Duan, J., Ai, H., & Tu, P. (2005). A low-temperature synthesis of multiwhisker-based zinc oxide micron crystals. *Materials Letters*, 59(28), 3710-3714.
- Liu, J., Huang, X., Li, Y., Sulieman, K., Sun, F., & He, X. (2006). Selective growth and properties of zinc oxide nanostructures. *Scripta Materialia*, 55(9), 795-798.
- Liu, L., Ryu, S., Tomasik, M. R., Stolyarova, E., Jung, N., Hybertsen, M. S., . . . Flynn, G. W. (2008). Graphene oxidation: thickness-dependent etching and strong chemical doping. *Nano letters*, 8(7), 1965-1970.
- Lu, G., Wang, X., Liu, J., Qiu, S., He, C., Li, B., & Liu, W. (2013). One-pot synthesis and gas sensing properties of ZnO mesoporous architectures. *Sensors and Actuators B: Chemical*, 184, 85-92.
- Ma, S., Li, R., Lv, C., Xu, W., & Gou, X. (2011). Facile synthesis of ZnO nanorod arrays and hierarchical nanostructures for photocatalysis and gas sensor applications. *Journal of Hazardous Materials*, 192(2), 730-740.
- Machlin, E. (2006). *Materials Science in Microelectronics: The relationships between thin film processing and structure*: Cambridge Univ Press.

- Manasreh, M. O. (2000). *III-Nitride Semiconductors: Electrical, Structural and Defects Properties: Electrical, Structural and Defects Properties*: Elsevier.
- Mao, D., Wang, X., Li, W., Liu, X., Li, Q., & Xu, J. (2002). Electron field emission from hydrogen-free amorphous carbon-coated ZnO tip array. *Journal of Vacuum Science & Technology B*, 20(1), 278-281.
- McLeary, E., Jansen, J., & Kapteijn, F. (2006). Zeolite based films, membranes and membrane reactors: Progress and prospects. *Microporous and Mesoporous Materials*, 90(1), 198-220.
- Miller, D. R., Akbar, S. A., & Morris, P. A. (2014). Nanoscale metal oxide-based heterojunctions for gas sensing: a review. *Sensors and Actuators B: Chemical*, 204, 250-272.
- Mishra, D., Mohapatra, J., Sharma, M., Chattarjee, R., Singh, S., Varma, S., . . . Entel, P. (2013). Carbon doped ZnO: synthesis, characterization and interpretation. *Journal of Magnetism and Magnetic Materials*, 329, 146-152.
- Molefe, F. V., Koao, L. F., Dejene, B. F., & Swart, H. C. (2015). Phase formation of hexagonal wurtzite ZnO through decomposition of Zn (OH) 2 at various growth temperatures using CBD method. *Optical Materials*, 46, 292-298.
- Mollar, M., Cembrero, J., Perales, M., Pascual, M., & Marí, B. (2006). Obtención de columnas de znO.: Variables a controlar (y II). *Boletín de la Sociedad Española de Cerámica y Vidrio*, 45(4), 278-282.
- Moreau, F., & Bond, G. C. (2007). Influence of the surface area of the support on the activity of gold catalysts for CO oxidation. *Catalysis Today*, 122(3), 215-221.
- Moulder, J. F., Chastain, J., & King, R. C. (1995). *Handbook of X-ray photoelectron spectroscopy: a reference book of standard spectra for identification and interpretation of XPS data*: Physical Electronics Eden Prairie, MN.
- Mozia, S. (2010). Photocatalytic membrane reactors (PMRs) in water and wastewater treatment. A review. *Separation and Purification Technology*, 73(2), 71-91.
- Musić, S., Dragčević, Đ., Maljković, M., & Popović, S. (2003). Influence of chemical synthesis on the crystallization and properties of zinc oxide. *Materials Chemistry and Physics*, 77(2), 521-530.
- Nakamura, I., Negishi, N., Kutsuna, S., Ihara, T., Sugihara, S., & Takeuchi, K. (2000). Role of oxygen vacancy in the plasma-treated TiO 2 photocatalyst with visible light activity for NO removal. *Journal of Molecular Catalysis A: Chemical*, 161(1), 205-212.
- NASA. (2014). Global Climate Change: Vital Signs of the Planet. Retrieved from <http://climate.nasa.gov/>
- NASA. (2016). NASA, NOAA Analyses Reveal Record-Shattering Global Warm Temperatures in 2015. Retrieved from <http://www.nasa.gov/press-release/nasa-noaa-analyses-reveal-record-shattering-global-warm-temperatures-in-2015>

- Naumkin, A. V., Kraut-Vass, A., Gaarenstroom, S. W., & Powell, C. J. (2012). National Institute of Standards and Technology (NIST) Material Measurement Laboratory (MML),.
- Nefedov, V., Salyn, Y. V., Leonhardt, G., & Scheibe, R. (1977). A comparison of different spectrometers and charge corrections used in X-ray photoelectron spectroscopy. *Journal of Electron Spectroscopy and Related Phenomena*, *10*(2), 121-124.
- Nikoobakht, B., Wang, X., Herzing, A., & Shi, J. (2013). Scalable synthesis and device integration of self-registered one-dimensional zinc oxide nanostructures and related materials. *Chemical Society Reviews*, *42*(1), 342-365.
- Nordell, B. (2003). Thermal pollution causes global warming. *Global and planetary change*, *38*(3), 305-312.
- O'Donoghue, M. (2006). *Gems: their sources, descriptions and identification*: Butterworth-Heinemann.
- Ogden, J. M. (1999). Prospects for building a hydrogen energy infrastructure. *Annual Review of Energy and the Environment*, *24*(1), 227-279.
- Oliveira, M. M., Schnitzler, D. C., & Zarbin, A. J. (2003). (Ti, Sn) O<sub>2</sub> Mixed Oxides Nanoparticles Obtained by the Sol-Gel Route. *Chemistry of Materials*, *15*(9), 1903-1909.
- Ong, K. G., Varghese, O. K., Mor, G. K., & Grimes, C. A. (2005). Numerical simulation of light propagation through highly-ordered titania nanotube arrays: Dimension optimization for improved photoabsorption. *Journal of Nanoscience and Nanotechnology*, *5*(11), 1801-1808.
- Otani, S., Katayama, J., Umemoto, H., & Matsuoka, M. (2006). Effect of bath temperature on the electrodeposition mechanism of zinc oxide film from zinc nitrate solution. *Journal of The Electrochemical Society*, *153*(8), C551-C556. doi:10.1149/1.2205187
- Othman, S. H., Rashid, S. A., Ghazi, T. I. M., & Abdullah, N. (2012). Dispersion and stabilization of photocatalytic TiO<sub>2</sub> nanoparticles in aqueous suspension for coatings applications. *Journal of Nanomaterials*, *2012*, 2.
- Ozyurt, O. (2010). Energy issues and renewables for sustainable development in Turkey. *Renewable and Sustainable Energy Reviews*, *14*(9), 2976-2985. doi:<http://dx.doi.org/10.1016/j.rser.2010.08.002>
- Pan, Z. W., Dai, Z. R., & Wang, Z. L. (2001). Nanobelts of semiconducting oxides. *Science*, *291*(5510), 1947-1949.
- Panigrahi, S., & Basak, D. (2011). Core-shell TiO<sub>2</sub>@ ZnO nanorods for efficient ultraviolet photodetection. *Nanoscale*, *3*(5), 2336-2341.

- Park, W. I., Kim, D., Jung, S.-W., & Yi, G.-C. (2002). Metalorganic vapor-phase epitaxial growth of vertically well-aligned ZnO nanorods. *Applied Physics Letters*, 80(22), 4232-4234.
- Parthasarathy, P., & Sheeba, K. N. (2015). Combined slow pyrolysis and steam gasification of biomass for hydrogen generation-a review. *International Journal of Energy Research*, 39(2), 147-164. doi:10.1002/er.3218
- Peighambardoust, S., Rowshanzamir, S., & Amjadi, M. (2010). Review of the proton exchange membranes for fuel cell applications. *International Journal of Hydrogen Energy*, 35(17), 9349-9384.
- Perel'Man, M. E., Rubinstein, G. M., & Tatartchenko, V. A. (2008). Mechanisms of dendrites occurrence during crystallization: Features of the ice crystals formation. *Physics Letters A*, 372(22), 4100-4103.
- Peulon, S., & Lincot, D. (1998). Mechanistic study of cathodic electrodeposition of zinc oxide and zinc hydroxychloride films from oxygenated aqueous zinc chloride solutions. *Journal of The Electrochemical Society*, 145(3), 864-874.
- Plummer, J. D., & Griffin, P. B. (2001). Material and process limits in silicon VLSI technology. *Proceedings of the IEEE*, 89(3), 240-258.
- Polshettiwar, V., Baruwati, B., & Varma, R. S. (2009). Self-assembly of metal oxides into three-dimensional nanostructures: synthesis and application in catalysis. *ACS nano*, 3(3), 728-736.
- Pradhan, D., Kumar, M., Ando, Y., & Leung, K. (2009). Fabrication of ZnO nanospikes and nanopillars on ITO glass by templateless seed-layer-free electrodeposition and their field-emission properties. *ACS applied materials & interfaces*, 1(4), 789-796.
- Radecka, M., Rekas, M., Trenczek-Zajac, A., & Zakrzewska, K. (2008). Importance of the band gap energy and flat band potential for application of modified TiO<sub>2</sub> photoanodes in water photolysis. *Journal of Power Sources*, 181(1), 46-55.
- Ramírez, D., Gómez, H., Riveros, G., Schrebler, R., Henríquez, R., & Lincot, D. (2010). Effect of Zn (II) concentration on the morphology of zinc oxide nanorods during electrodeposition on very thin alumina membrane templates. *The Journal of Physical Chemistry C*, 114(35), 14854-14859.
- Rehman, S., Ullah, R., Butt, A., & Gohar, N. (2009). Strategies of making TiO<sub>2</sub> and ZnO visible light active. *Journal of Hazardous Materials*, 170(2), 560-569.
- Reij, M. W., Keurentjes, J. T., & Hartmans, S. (1998). Membrane bioreactors for waste gas treatment. *Journal of Biotechnology*, 59(3), 155-167.
- Rohani, S., Tavare, N., & Garside, J. (1990). Control of crystal size distribution in a batch cooling crystallizer. *The Canadian Journal of Chemical Engineering*, 68(2), 260-267.

- Roy, C., Byrne, S., McGlynn, E., Mosnier, J.-P., de Posada, E., O'Mahony, D., . . . Cafolla, A. A. (2003). Correlation of Raman and X-ray diffraction measurements of annealed pulsed laser deposited ZnO thin films. *Thin Solid Films*, 436(2), 273-276.
- Sahu, R. K., Ganguly, K., Mishra, T., Mishra, M., Ningthoujam, R., Roy, S., & Pathak, L. (2012). Stabilization of intrinsic defects at high temperatures in ZnO nanoparticles by Ag modification. *Journal of Colloid and Interface Science*, 366(1), 8-15.
- Saitoh, H., Satoh, M., Tanaka, N., Ueda, Y., & Ohshio, S. (1999). Homogeneous growth of zinc oxide whiskers. *Japanese Journal of Applied Physics*, 38(12R), 6873.
- Salih, F., & Pillay, A. (2007). Efficiency of solar water disinfection photocatalized by titanium dioxide of varying particle size. *Journal of water and health*, 5(3), 335-340.
- Samad, N. A. A., Lai, C. W., & Hamid, S. B. A. (2016). Influence applied potential on the formation of self-organized ZnO nanorod film and its photoelectrochemical response.
- Sanjeev, S., & Kekuda, D. (2015). *Effect of Annealing Temperature on the Structural and Optical Properties of Zinc Oxide (ZnO) Thin Films Prepared by Spin Coating Process*. Paper presented at the IOP Conference Series: Materials Science and Engineering.
- Sbrockey, N. M., & Ganesan, S. (2004). ZnO thin films by MOCVD. *III-Vs Review*, 17(7), 23-25.
- Schierbaum, K., Kirner, U., Geiger, J., & Göpel, W. (1991). Schottky-barrier and conductivity gas sensors based upon Pd/SnO<sub>2</sub> and Pt/TiO<sub>2</sub>. *Sensors and Actuators B: Chemical*, 4(1), 87-94.
- Scholes, C. A., Smith, K. H., Kentish, S. E., & Stevens, G. W. (2010). CO<sub>2</sub> capture from pre-combustion processes—strategies for membrane gas separation. *International Journal of Greenhouse Gas Control*, 4(5), 739-755.
- Schumm, M., Koerdel, M., Morhange, J., Golacki, Z., Graszka, K., Skupinski, P., . . . Kalt, H. (2007). *Analysis of the vibrational properties of Zn<sub>1-x</sub>CoxO by Raman spectroscopy*. Paper presented at the Journal of Physics: Conference Series.
- Sendi, R. K., & Mahmud, S. (2013). Stress control in ZnO nanoparticle-based discs via high-oxygen thermal annealing at various temperatures. *Journal of Physical Science*, 24(1), 1-15.
- SHAHAB, M., TABISH, T., ZAMAN, B., TARIQ, Z., & KAMRAN, M. (2013). CHARACTERIZATION AND SYNTHESIS OF NANOSIZED TiO<sub>2</sub> PARTICLES. *Annals of the Faculty of Engineering Hunedoara-International Journal of Engineering*, 11(3).
- Shaheen, B. S., Salem, H. G., El-Sayed, M. A., & Allam, N. K. (2013). Thermal/Electrochemical growth and characterization of one-dimensional

ZnO/TiO<sub>2</sub> hybrid nanoelectrodes for solar fuel production. *The Journal of Physical Chemistry C*, 117(36), 18502-18509.

Shankar, K., Mor, G. K., Prakasam, H. E., Yoriya, S., Paulose, M., Varghese, O. K., & Grimes, C. A. (2007). Highly-ordered TiO<sub>2</sub> nanotube arrays up to 220  $\mu\text{m}$  in length: use in water photoelectrolysis and dye-sensitized solar cells. *Nanotechnology*, 18(6), 065707.

Shao, D., Sun, H., Xin, G., Lian, J., & Sawyer, S. (2014). High quality ZnO–TiO<sub>2</sub> core–shell nanowires for efficient ultraviolet sensing. *Applied Surface Science*, 314, 872-876.

Shen, X.-Y., Zhai, Y.-C., & Zhang, Y.-H. (2010). Preparation and characterization of ultrafine zinc oxide powder by hydrothermal method. *Transactions of Nonferrous Metals Society of China*, 20, s236-s239.

Shin, B., Won, J., Son, T., Kang, Y. S., & Kim, C. K. (2011). Barrier effect of dendrons on TiO<sub>2</sub> particles in dye sensitized solar cells. *Chemical Communications*, 47(6), 1734-1736.

Skoog, D. A., & West, D. M. (1980). *Principles of instrumental analysis* (Vol. 158): Saunders College Philadelphia.

Smith, D. L. (1995). *Thin-film deposition: principles and practice*: McGraw-hill New York etc.

Soares, J. M., Morrall, P., Crossley, A., Harris, P., & Bowker, M. (2003). Catalytic and noncatalytic CO oxidation on Au/TiO<sub>2</sub> catalysts. *Journal of catalysis*, 219(1), 17-24.

Solís-Pomar, F., Martínez, E., Meléndrez, M. F., & Pérez-Tijerina, E. (2011). Growth of vertically aligned ZnO nanorods using textured ZnO films. *Nanoscale Research Letters*, 6(1), 1-11.

Stoica, G. M., Stoica, A. D., Miller, M. K., & Ma, D. (2014). Temperature-dependent elastic anisotropy and mesoscale deformation in a nanostructured ferritic alloy. *Nature communications*, 5.

Studenikin, S., Golego, N., & Cocivera, M. (1998). Fabrication of green and orange photoluminescent, undoped ZnO films using spray pyrolysis. *Journal of Applied Physics*, 84(4), 2287-2294.

Stull, D. R., & Prophet, H. (1971). *JANAF thermochemical tables*. Retrieved from

Subramanian, V., Wolf, E. E., & Kamat, P. V. (2004). Catalysis with TiO<sub>2</sub>/gold nanocomposites. Effect of metal particle size on the Fermi level equilibration. *Journal of the American Chemical Society*, 126(15), 4943-4950.

Sun, Q., Lu, Y., Xia, Y., Yang, D., Li, J., & Liu, Y. (2012). Flame retardancy of wood treated by TiO<sub>2</sub>/ZnO coating. *Surface Engineering*, 28(8), 555-559.

- Sun, Y., Wang, G., & Yan, K. (2011). TiO<sub>2</sub> nanotubes for hydrogen generation by photocatalytic water splitting in a two-compartment photoelectrochemical cell. *International Journal of Hydrogen Energy*, 36(24), 15502-15508.
- Tabakova, T., Idakiev, V., Andreeva, D., & Mitov, I. (2000). Influence of the microscopic properties of the support on the catalytic activity of Au/ZnO, Au/ZrO<sub>2</sub>, Au/Fe<sub>2</sub>O<sub>3</sub>, Au/Fe<sub>2</sub>O<sub>3</sub>-ZnO, Au/Fe<sub>2</sub>O<sub>3</sub>-ZrO<sub>2</sub> catalysts for the WGS reaction. *Applied Catalysis A: General*, 202(1), 91-97.
- Tang, Q., Lin, L., Zhao, X., Huang, K., & Wu, J. (2012). p-n heterojunction on ordered ZnO nanowires/polyaniline microrods double array. *Langmuir*, 28(8), 3972-3978.
- Tena-Zaera, R., Elias, J., Wang, G., & Levy-Clement, C. (2007). Role of chloride ions on electrochemical deposition of ZnO nanowire arrays from O<sub>2</sub> reduction. *The Journal of Physical Chemistry C*, 111(45), 16706-16711.
- Tena-Zaera, R., Katty, A., Bastide, S., Lévy-Clément, C., O'Regan, B., & Muñoz-Sanjosé, V. (2005). ZnO/CdTe/CuSCN, a promising heterostructure to act as inorganic eta-solar cell. *Thin Solid Films*, 483(1), 372-377.
- Termnak, S., Triampo, W., & Triampo, D. (2009). Effect of acid during synthesis on the agglomerated strength of TiO<sub>2</sub> nanoparticles. *Journal of Ceramic Processing Research*, 10(4), 491-496.
- Tian, J., Chen, L., Yin, Y., Wang, X., Dai, J., Zhu, Z., . . . Wu, P. (2009). Photocatalyst of TiO<sub>2</sub>/ZnO nano composite film: preparation, characterization, and photodegradation activity of methyl orange. *Surface and Coatings Technology*, 204(1), 205-214.
- Tien, L., Pearton, S., Norton, D., & Ren, F. (2008). Synthesis and microstructure of vertically aligned ZnO nanowires grown by high-pressure-assisted pulsed-laser deposition. *Journal of Materials Science*, 43(21), 6925-6932.
- Tompa, G. S., Sun, S., Provost, L., Mentel, D., Sugrim, D., Chan, P., . . . Lee, A. (2006). *Large area multi-wafer MOCVD of transparent and conducting ZnO films*. Paper presented at the MRS Proceedings.
- Turrell, G., Gardiner, D., & Graves, P. (1989). Practical Raman Spectroscopy. *Gardiner, DJ*, 13-54.
- Uchida, H., Arisaka, S.-i., & Watanabe, M. (2002). High Performance Electrode for Medium-Temperature Solid Oxide Fuel Cells: Control of Microstructure of La (Sr) CoO<sub>3</sub> Cathodes with Highly Dispersed Pt Electrocatalysts. *Journal of The Electrochemical Society*, 149(1), A13-A18.
- Uchida, H., Arisaka, S., & Watanabe, M. (2000). High performance electrodes for medium-temperature solid oxide fuel cells: Activation of La (Sr) CoO<sub>3</sub> cathode with highly dispersed Pt metal electrocatalysts. *Solid State Ionics*, 135(1), 347-351.
- Uchida, H., Mochizuki, N., & Watanabe, M. (1996). High-Performance Electrode for Medium-Temperature Operating Solid Oxide Fuel Cells Polarization Property of

Ceria-Based Anode with Highly Dispersed Ruthenium Catalysts in Gas. *Journal of The Electrochemical Society*, 143(5), 1700-1704.

Uchida, H., Suzuki, H., & Watanabe, M. (1998). High-Performance Electrode for Medium-Temperature Solid Oxide Fuel Cells Effects of Composition and Microstructures on Performance of Ceria-Based Anodes. *Journal of The Electrochemical Society*, 145(2), 615-620.

Ullah, R., & Dutta, J. (2008). Photocatalytic degradation of organic dyes with manganese-doped ZnO nanoparticles. *Journal of Hazardous Materials*, 156(1), 194-200.

United States Environmental Protection Agency (EPA). (2001). Global Warming.

Varghese, N., Panchakarla, L., Hanapi, M., Govindaraj, A., & Rao, C. (2007). Solvothermal synthesis of nanorods of ZnO, N-doped ZnO and CdO. *Materials Research Bulletin*, 42(12), 2117-2124.

Wahab, R., Ansari, S., Kim, Y.-S., Seo, H.-K., & Shin, H.-S. (2007). Room temperature synthesis of needle-shaped ZnO nanorods via sonochemical method. *Applied Surface Science*, 253(18), 7622-7626.

Wang, H.-C., Liao, C.-H., Chueh, Y.-L., Lai, C.-C., Chou, P.-C., & Ting, S.-Y. (2013). Crystallinity improvement of ZnO thin film by hierarchical thermal annealing. *Optical Materials Express*, 3(2), 295-306.

Wang, J. (2006). *Analytical electrochemistry*: John Wiley & Sons.

Wang, S. (2009). Holocene cold events in the North Atlantic: Chronology and climatic impact. *Chinese Quat. Sci*, 29(6), 1146-1153.

Wang, X., Yu, J. C., Chen, Y., Wu, L., & Fu, X. Q. (2006). TiO<sub>2</sub>-xN<sub>x</sub>, ZrO<sub>2</sub>-Modified Mesoporous Nanocrystalline as Efficient Visible Light Photocatalysts *Environmental Science & Technology*, 40(7), 2369-2374.

Wang, Y., Cheng, H., Edwards, R. L., He, Y., Kong, X., An, Z., . . . Li, X. (2005). The Holocene Asian monsoon: links to solar changes and North Atlantic climate. *Science*, 308(5723), 854-857.

Wang, Z., Zhang, H., Zhang, L., Yuan, J., Yan, S., & Wang, C. (2002). Low-temperature synthesis of ZnO nanoparticles by solid-state pyrolytic reaction. *Nanotechnology*, 14(1), 11.

Wang, Z. L. (2004). Zinc oxide nanostructures: growth, properties and applications. *Journal of Physics: Condensed Matter*, 16(25), R829.

Weidenkaff, A., Reller, A., Wokaun, A., & Steinfeld, A. (2000). Thermogravimetric analysis of the ZnO/Zn water splitting cycle. *Thermochimica Acta*, 359(1), 69-75.

Westermann, T., & Melin, T. (2009). Flow-through catalytic membrane reactors—principles and applications. *Chemical Engineering and Processing: Process Intensification*, 48(1), 17-28.

- Willard, H. H., Merritt Jr, L. L., Dean, J. A., & Settle Jr, F. A. (1988). Instrumental methods of analysis.
- Wolf, S., & Tauber, R. N. Silicon Processing for the VLSI Era vol. 1: Process technology, 1986: Lattice Press.
- Wong, M., Berenov, A., Qi, X., Kappers, M., Barber, Z., Illy, B., . . . MacManus-Driscoll, J. (2003). Electrochemical growth of ZnO nano-rods on polycrystalline Zn foil. *Nanotechnology*, 14(9), 968.
- Woodside, S. M., Bowen, B. D., & Piret, J. M. (1998). Mammalian cell retention devices for stirred perfusion bioreactors. *Cytotechnology*, 28(1-3), 163-175.
- Wright, J. D., & Sommerdijk, N. A. (2000). *Sol-gel materials: chemistry and applications* (Vol. 4): CRC press.
- Wu, J.-J., Liu, S.-C., Wu, C.-T., Chen, K.-H., & Chen, L.-C. (2002). Heterostructures of ZnO-Zn coaxial nanocables and ZnO nanotubes. *Applied Physics Letters*, 81(7), 1312-1314.
- Wu, M.-K., Chen, M.-J., Tsai, F.-Y., Yang, J.-R., & Shiojiri, M. (2010). Fabrication of ZnO nanopillars by atomic layer deposition. *Materials Transactions*, 51(2), 253-255.
- Xie, Q., Dai, Z., Liang, J., Xu, L., Yu, W., & Qian, Y. (2005). Synthesis of ZnO three-dimensional architectures and their optical properties. *Solid State Communications*, 136(5), 304-307.
- Xu, H., Wang, X., & Zhang, L. (2008). Selective preparation of nanorods and micro-octahedrons of  $\text{Fe}_2\text{O}_3$  and their catalytic performances for thermal decomposition of ammonium perchlorate. *Powder Technology*, 185(2), 176-180.
- Xu, S., & Wang, Z. L. (2011). One-dimensional ZnO nanostructures: solution growth and functional properties. *Nano Research*, 4(11), 1013-1098.
- Xu, T., Ji, P., He, M., & Li, J. (2012). Growth and structure of pure ZnO micro/nanocombs. *Journal of Nanomaterials*, 2012, 12.
- Xue, J., Liang, W., Liu, X., Shen, Q., & Xu, B. (2012). Crystallization behavior and formation mechanism of dendrite  $\text{Cu}_2\text{O}$  crystals. *CrystEngComm*, 14(23), 8017-8022.
- Yamauchi, S., Goto, Y., & Hariu, T. (2004). Photoluminescence studies of undoped and nitrogen-doped ZnO layers grown by plasma-assisted epitaxy. *Journal of Crystal Growth*, 260(1), 1-6.
- Yang, Y., Li, Y., Zhu, L., He, H., Hu, L., Huang, J., . . . Ye, Z. (2013). Shape control of colloidal Mn doped ZnO nanocrystals and their visible light photocatalytic properties. *Nanoscale*, 5(21), 10461-10471.

- Yang, Y., Yan, H., Fu, Z., Yang, B., & Zuo, J. (2006). Correlation between 577 cm<sup>-1</sup> Raman scattering and green emission in ZnO ordered nanostructures. *Applied Physics Letters*, 88(19), 1909.
- Yi, S. H., Choi, S. K., Jang, J. M., Kim, J. A., & Jung, W. G. (2007). Low-temperature growth of ZnO nanorods by chemical bath deposition. *J Colloid Interface Sci*, 313(2), 705-710. doi:10.1016/j.jcis.2007.05.006
- Yiamsawas, D., Boonpavanitchakul, K., & Kangwansupamonkon, W. (2009). Preparation of ZnO nanostructures by solvothermal method. *J. of Microscopy Society of Thailand*, 23, 75-78.
- Yin, S. F., Xu, B. Q., Zhou, X. P., & Au, C. T. (2004). A mini-review on ammonia decomposition catalysts for on-site generation of hydrogen for fuel cell applications. *Applied Catalysis a-General*, 277(1-2), 1-9. doi:10.1016/j.apcata.2004.09.020
- Yu, J., Zhao, X., & Zhao, Q. (2000). Effect of surface structure on photocatalytic activity of TiO<sub>2</sub> thin films prepared by sol-gel method. *Thin Solid Films*, 379(1), 7-14.
- Zeng, H., Cai, W., Liu, P., Xu, X., Zhou, H., Klingshirn, C., & Kalt, H. (2008). ZnO-based hollow nanoparticles by selective etching: elimination and reconstruction of metal– semiconductor interface, improvement of blue emission and photocatalysis. *ACS nano*, 2(8), 1661-1670.
- Zeng, H., Liu, P., Cai, W., Yang, S., & Xu, X. (2008). Controllable Pt/ZnO porous nanocages with improved photocatalytic activity. *The Journal of Physical Chemistry C*, 112(49), 19620-19624.
- Zeng, J. H., Jin, B. B., & Wang, Y. F. (2009). Facet enhanced photocatalytic effect with uniform single-crystalline zinc oxide nanodisks. *Chemical Physics Letters*, 472(1), 90-95.
- Zhang, H., Zong, R., & Zhu, Y. (2009). Photocorrosion inhibition and photoactivity enhancement for zinc oxide via hybridization with monolayer polyaniline. *The Journal of Physical Chemistry C*, 113(11), 4605-4611.
- Zhang, L., Cheng, H., Zong, R., & Zhu, Y. (2009). Photocorrosion suppression of ZnO nanoparticles via hybridization with graphite-like carbon and enhanced photocatalytic activity. *The Journal of Physical Chemistry C*, 113(6), 2368-2374.
- Zhang, R., Yin, P.-G., Wang, N., & Guo, L. (2009). Photoluminescence and Raman scattering of ZnO nanorods. *Solid State Sciences*, 11(4), 865-869.
- Zhang, X., Dai, J., Lam, C., Wang, H., Webley, P., Li, Q., & Ong, H. (2007). Zinc/ZnO core–shell hexagonal nanodisk dendrites and their photoluminescence. *Acta Materialia*, 55(15), 5039-5044.
- Zhang, X., Qin, J., Hao, R., Wang, L., Shen, X., Yu, R., . . . Liu, R. (2015). Carbon-Doped ZnO Nanostructures: Facile Synthesis and Visible Light Photocatalytic Applications. *The Journal of Physical Chemistry C*, 119(35), 20544-20554.

- Zheng, J., Song, J., Li, X., Jiang, Q., & Lian, J. (2011). Experimental and first-principle investigation of Cu-doped ZnO ferromagnetic powders. *Crystal Research and Technology*, 46(11), 1143-1148.
- Zheng, Y., Zheng, L., Zhan, Y., Lin, X., Zheng, Q., & Wei, K. (2007). Ag/ZnO heterostructure nanocrystals: synthesis, characterization, and photocatalysis. *Inorganic chemistry*, 46(17), 6980-6986.
- Zheng, Z., Lim, Z. S., Peng, Y., You, L., Chen, L., & Wang, J. (2013). General route to ZnO nanorod arrays on conducting substrates via galvanic-cell-based approach. *Scientific reports*, 3.
- Zhou, H., Alves, H., Hofmann, D., Kriegseis, W., Meyer, B., Kaczmarczyk, G., & Hoffmann, A. (2002). Behind the weak excitonic emission of ZnO quantum dots: ZnO/Zn(OH)<sub>2</sub> core-shell structure. *Applied Physics Letters*, 80(2), 210-212.

University of Malaya

## LIST OF PUBLICATIONS AND PAPERS PRESENTED

### ISI-Cited Publications

1. **Nur Azimah Abd Samad**, Chin Wei Lai, & Sharifah Bee Abd Hamid. (2015). Easy Formation of Nanodisk-Dendritic ZnO Film via Controlled Electrodeposition Process. *Journal of Nanomaterials*, 2015.
2. **Nur Azimah Abd Samad**, Chin Wei Lai, & Sharifah Bee Abd Hamid. (2016). Influence applied potential on the formation of self-organized ZnO nanorod film and its photoelectrochemical response. *Journal of Photoenergy*, 2016.

### Conference Proceedings

1. **Nur Azimah Abd Samad**, Chin Wei Lai, & Sharifah Bee Abd Hamid. (2014, November 24-25). The influence of heat treatment on current-applied potential characteristics of electrodeposited zinc oxide nanostructure film. Paper presented at the 2nd International Conference on Green Technology & Ecosystem for Global Sustainable Development, Putrajaya, Malaysia.
2. **Nur Azimah Abd Samad**, Chin Wei Lai, & Sharifah Bee Abd Hamid. (2014, December 17-18). The influence of precipitation-peptisation temperature towards morphology and crystallite size of TiO<sub>2</sub>. Paper presented at the 6th International Conference on Postgraduate Education, Malacca, Malaysia.
3. **Nur Azimah Abd Samad**, Chin Wei Lai, Sharifah Bee Abd Hamid, and S. Mallick, (2016, February 27-28). Enhanced solar-activated PEC water splitting system using TiO<sub>2</sub>-ZnO hybrid film. Paper presented at the International Seminar

on Nanoscience and Nanotechnology 2016 (NANO-SciTech 2016), Shah Alam, Malaysia.

4. **Nur Azimah Abd Samad**, Chin Wei Lai, Kian Mun Lee, Joon Ching Juan, Sharifah Bee Abd Hamid, S. Mallick (2016, February 27-28). Easy formation of titanate nanotubes for promising photocatalytic activity. Paper presented at the International Seminar on Nanoscience and Nanotechnology 2016 (NANO-SciTech 2016), Shah Alam, Malaysia.

University of Malaya